



TECHNISCHE  
UNIVERSITÄT  
WIEN



## DIPLOMARBEIT

# Background Analysis of CRESST-III Dark Matter Detectors

zur Erlangung des akademischen Grades

**Diplom-Ingenieur**

im Rahmen des Masterstudiums

**Technische Physik**

eingereicht von

**Julius Tesarek, BSc**  
Matrikelnummer 11913103

ausgeführt am Atominstitut  
der Fakultät Physik der Technischen Universität Wien  
in Zusammenarbeit mit dem Institut für Hochenergiephysik

### **Betreuung**

Dr. Samir Banik  
Univ.Prof. Dipl.-Phys. Dr.rer.nat. Jochen Schieck

Wien, 15.04.2025

---

(Unterschrift Verfasser)

---

(Unterschrift Betreuer)

# ABSTRACT

Even though there exists a large and diverse amount of observational evidence for the existence of dark matter (DM), its nature is still not clear. The Cryogenic Rare Event Search with Superconducting Thermometers (CRESST) experiment, located underground in the Laboratori Nazionali del Gran Sasso (LNGS), Italy, strives to directly detect DM particles in the sub-GeV/ $c^2$  mass range. CRESST exploits the low heat capacity of materials at temperatures close to absolute zero, measuring the temperature increase of target crystals caused by elastic scattering of (potentially DM) particles on the target's nuclei. This rise in temperature is quantified using transition edge sensors in combination with superconducting quantum interference devices. The Gran Sasso mountain above the LNGS underground laboratory provides substantial shielding from cosmic radiation, with a rock overburden of around 1400 m. To further reduce unwanted signals from standard model particles, multiple layers of active and passive shielding surround CRESST's detectors. Despite these measures, there are still backgrounds to be expected from radioactivity inside or close to the detectors. Knowing the amounts of different radioactive impurities is crucial for both DM search and the development of novel sensors with reduced backgrounds.

In this work, data of four  $\text{CaWO}_4$  detectors from the CRESST-III phase's "Run36" data taking campaign, recorded between November 2020 and November 2022, is analysed. In the high-energy range, with event energies on the order of MeV, the signal pulses are saturated in the analysed detectors. This necessitates special methods to reconstruct the corresponding energies. Alpha decay spectra are obtained by analysing the duration of pulse saturation, extending the available energy range for background analyses into the MeV region. This saturation time analysis is implemented and applied to the considered data. A calibration, mapping the saturation times to energies, is done through the identification of known spectral lines and the fit of an exponential function, following considerations on the pulse shape. As a second procedure for energy reconstruction, pulse templates are fitted to the event pulses. By restricting the fit to voltages below a certain truncation level, the non-linear detector response for high-energy events can be bypassed. The calibration of the truncated template fit utilises an intentionally positioned radioactive  $^{55}\text{Fe}$  source as well as information gained through the saturation time analysis. Moreover, techniques to handle artefacts, which commonly appear in the voltage traces at high event energies, are developed or improved, enhancing the correct processing of affected pulses.

The spectra obtained in this work allow for first estimations of the contamination levels of the examined detectors. More importantly, they serve as a basis for further in-depth investigations, involving Bayesian likelihood fits of simulated spectral templates to the experimental data, to determine the separate activities of impurities.

# KURZFASSUNG

Obwohl es eine Vielzahl von Beobachtungen gibt, die auf die Existenz Dunkler Materie (DM) hindeuten, ist deren Natur noch immer nicht geklärt. Das “Cryogenic Rare Event Search with Superconducting Thermometers” (CRESST) Experiment, das sich unterirdisch im italienischen Laboratori Nazionali del Gran Sasso (LNGS) befindet, strebt danach, DM Teilchen mit Massen im sub-GeV/ $c^2$ -Bereich direkt nachzuweisen. CRESST nutzt die geringe Wärmekapazität von Materialien bei Temperaturen nahe dem absoluten Nullpunkt und misst den Temperaturanstieg von Detektorkristallen, der durch elastische Streuung von Teilchen (potentiell DM) an den Atomkernen der Kristalle verursacht wird. Dieser Temperaturanstieg wird mit Hilfe von Phasenübergangsthermometern in Kombination mit supraleitenden Quanteninterferenzgeräten gemessen. Das Gran-Sasso-Gebirgsmassiv oberhalb des unterirdischen LNGS-Labors schirmt die kosmische Strahlung mit einer Gesteinsdicke von etwa 1400 Metern erheblich ab. Um unerwünschte Signale von Teilchen des Standardmodells weiter zu reduzieren, umgeben mehrere Schichten aktiver und passiver Abschirmung die Detektoren von CRESST. Trotz dieser Maßnahmen ist immer noch mit Hintergrundsignalen zu rechnen, die von Radioaktivität innerhalb der Detektoren, oder von Quellen in ihrer Nähe herrühren. Die Kenntnis der Mengen verschiedener radioaktiver Verunreinigungen ist sowohl für die DM-Suche als auch für die Entwicklung neuartiger Sensoren mit geringerem Hintergrund entscheidend.

In dieser Arbeit werden Daten von vier  $\text{CaWO}_4$ -Detektoren analysiert, die zwischen November 2020 und November 2022 im Rahmen der “Run36”-Datennahmekampagne der CRESST-III-Phase aufgezeichnet wurden. Im Bereich hoher Energien, mit Energiedepositionen in der Größenordnung von MeV, sind die Signalpulse in den analysierten Detektoren gesättigt. Dies erfordert spezielle Methoden, um die entsprechenden Energien zu rekonstruieren. Alphazerfallsspektren werden durch Analyse der Dauer der Pulssättigung gewonnen, wodurch der verfügbare Energiebereich für Hintergrundanalysen in den MeV-Bereich erweitert wird. Diese Sättigungszeitanalyse wird implementiert und auf die betrachteten Daten angewendet. Eine Kalibrierung, bei der die Sättigungszeiten in Energien umgerechnet werden, erfolgt durch die Identifizierung bekannter Spektrallinien und die Anpassung einer Exponentialfunktion, beruhend auf Überlegungen zur Pulsform. Als zweites Verfahren zur Energierekonstruktion werden Standardpulse an Ereignispulse angepasst. Durch Beschränkung der Anpassung auf Spannungen unterhalb eines bestimmten Abschneideniveaus kann das nichtlineare Detektorverhalten für hochenergetische Ereignisse umgangen werden. Zur Kalibrierung der so erhaltenen Spektren werden eine absichtlich eingebrachte radioaktive  $^{55}\text{Fe}$ -Quelle sowie Informationen aus der Sättigungszeitanalyse verwendet. Darüber hinaus werden Techniken zur Behandlung von Artefakten, die bei hohen Ereignisenergien häufig in den Daten auftreten, entwickelt bzw. verbessert, was die korrekte Analyse der betroffenen Pulse verbessert.

Die in dieser Arbeit gewonnenen Spektren ermöglichen erste Abschätzungen der Verunreinigungsgrade der untersuchten Detektoren. Weiters dienen sie als Grundlage für eingehende Untersuchungen, die Bayes’sche Likelihood-Anpassungen von simulierten Spektralvorlagen an die experimentellen Daten umfassen, um die einzelnen Aktivitäten der Verunreinigungen zu bestimmen.

# ACKNOWLEDGEMENTS

For their support throughout my work on the project presented here, I want to express gratitude to my supervisors, Samir Banik and Jochen Schieck. As my first contact for issues of all kinds, Samir pointed me towards relevant resources, while also reminding me to remain focused. I want to thank him especially for his active help and his suggestions for improving my writing. To Jochen, I am grateful for always having an open ear despite numerous other obligations, and for providing me with the opportunity to participate in a CRESST collaboration meeting as well as a work trip to the group in Bratislava.

Regarding questions of software and analysis, I would like to highlight the assistance I received from Philipp Schreiner, a colleague at HEPHY. Furthermore, a number of others at the institute and within the CRESST collaboration provided me with insights and advice that were valuable for my work. The computational results presented were obtained using the CLIP cluster (<https://clip.science>).

A heartfelt “thank you” goes out to my friends and family for their continued support, not just during the work on my thesis, but throughout all of my studies. My study group in particular made the last years so much more enjoyable. At the same time, I am deeply grateful for the unwavering support my parents provided, both financially and on a personal level. They enabled me to concentrate on my studies and always encouraged me to pursue my interests.

# CONTENTS

<b>1. Introduction</b>	<b>1</b>
1.1. Evidence for Dark Matter	2
1.1.1. Galactic Rotation Curves	2
1.1.2. Galaxy Cluster Dynamics	3
1.1.3. Intracluster Medium	4
1.1.4. Gravitational Lensing and Cluster Collisions	4
1.1.5. Cosmic Microwave Background Radiation	6
1.1.6. Structure Formation	6
1.2. Dark Matter Candidates	7
1.2.1. Modified Theories of Gravity	7
1.2.2. Baryonic Dark Matter	8
1.2.3. Neutrinos	8
1.2.4. WIMPs	9
1.2.5. Axions	9
1.3. Dark Matter Searches	10
1.3.1. Direct Detection	10
1.3.2. Indirect Detection	11
1.3.3. Collider Searches	12
1.3.4. Current Status	13
<b>2. The CRESST Experiment</b>	<b>14</b>
2.1. Experimental Setup	14
2.1.1. Radiation Shieldings	14
2.1.2. Cryogenic System	16
2.1.3. Detector Holding Structure and Cabling	16
2.2. CRESST Detectors	16
2.2.1. Modules	17
2.2.2. Cryogenic Detection Principle and Readout System	18
2.2.3. Transition Edge Sensors	19
2.2.4. Superconducting Quantum Interference Devices	20
2.2.5. Detector Operation and Data Acquisition	23
2.3. Background	25
2.3.1. Natural Radioactivity	25
2.3.2. Origin of Radionuclides	26
2.3.3. Low Energy Excess	27
2.3.4. Background Simulations and Modelling	27
<b>3. CRESST Data Analysis</b>	<b>29</b>
3.1. Types of Recorded Data	29
3.1.1. Hardware-Triggered Data	29
3.1.2. Continuously Recorded Data	30

3.2. Standard Analysis Methods . . . . .	30
3.2.1. Fundamental Analysis Parameters . . . . .	30
3.2.2. Special Event Types and Artefacts . . . . .	31
3.2.3. Event Selection . . . . .	33
3.2.4. Standard Event, Noise Power Spectrum and Optimum Filter . . . . .	34
3.2.5. Stream Triggering and Threshold . . . . .	36
3.2.6. Energy Reconstruction . . . . .	38
3.3. Extension of the Accessible Energy Range . . . . .	40
3.3.1. Flux Quantum Loss Correction . . . . .	40
3.3.2. Saturation Time Analysis . . . . .	41
3.3.3. Truncated Template Fit . . . . .	43
<b>4. Results of the Analysis</b>	<b>45</b>
4.1. Datasets . . . . .	45
4.2. TUM93A . . . . .	46
4.2.1. Hardware Triggered Data and Software Triggering . . . . .	46
4.2.2. Energy Reconstruction Methods . . . . .	47
4.2.3. Calibration . . . . .	48
4.2.4. Spectra and Likelihood Fit of Simulated Templates . . . . .	51
4.3. TUM93C, Comm1 and Comm2 . . . . .	55
<b>5. Conclusion</b>	<b>59</b>
<b>A. Lists of Analysed Files</b>	<b>60</b>
<b>Bibliography</b>	<b>viii</b>

# LIST OF ACRONYMS

BCS theory	Bardeen-Cooper-Schrieffer theory
CMB	Cosmic microwave background
CP	Control pulse <i>or</i> charge conjugation parity
CRESST	Cryogenic Rare Event Search with Superconducting Thermometers
DAC	Digital-to-analogue converter
DAQ	Data acquisition
DC	Direct current
DM	Dark matter
FQ	Flux quantum
FQL	Flux quantum loss
FQLC	Flux quantum loss correction
ICM	Intracluster medium
LEE	Low energy excess
LNGS	Laboratori Nazionali del Gran Sasso (Gran Sasso national laboratory)
MACHO	Massive compact halo object
MMD	Minimum-minimum difference
MOND	Modified Newtonian dynamics
NPS	Noise power spectrum
OF	Optimal filter
PMT	Photomultiplier tube
QDC	Charge-to-digital converter
RMS	Root mean square
SD	Standard deviation
SE	Secular equilibrium
SEV	Standard event
SM	Standard Model (of particle physics)
SOS	Silicon-on-sapphire
SQUID	Superconducting quantum interference device
STA	Saturation time analysis
TES	Transition edge sensor
TF	Template fit
TTF	Truncated template fit
TP	Test pulse
TPA	Test pulse amplitude (voltage set on the pulser)
WIMP	Weakly interacting massive particle
WP	Working point
WU	Warm-up

# 1. INTRODUCTION

The quest to understand the world that surrounds us has ever been a main driving force behind the endeavours of physical science. With this objective, the prediction of previously unknown objects or forms of matter through the careful study of what is known has an important history in astronomy and particle physics. For instance, 19<sup>th</sup> century astronomers, using Newton’s law of universal gravitation [1] to analyse irregularities in the orbit of the planet Uranus, predicted and subsequently observed the presence of another planet: Neptune [2]. In 2012, the discovery of a massive particle, known as the Higgs boson, was announced jointly by the CMS [3] and ATLAS [4] collaborations at CERN, after being theorized in the 1960s by Peter Higgs and others [5–7] to explain the masses of W- and Z-bosons. Today, we find ourselves in a situation similar to the first scenario outlined above. Diverse astronomical observations, a selection of which is presented in Section 1.1, suggest the presence of invisible matter: dark matter, or DM for short. DM is thus a hypothesised form of matter that interacts with ordinary matter via gravitation, but not electromagnetically, and which can explain the mentioned observations. At the same time, there is also theoretical motivation for various as of yet unobserved elementary particles (see Section 1.2), much like there was for the Higgs boson. It is possible that DM is at least partly composed of such particles, dealing not only with the astronomical evidence but also extending the *Standard Model* (SM) of particle physics [8]. Alternatively, DM could also be composed of large astrophysical objects, although this already seems unlikely. Further, the observations could be not a manifestation of DM but a sign for the inapplicability of our currently best theory of gravity, general relativity, at large scales. However, a modified theory of gravity that can explain all observations would still have to be found. As a consequence, particle DM appears to be the most promising hypothesis and profound searches are conducted [9–11], as briefly reviewed in Section 1.3, aiming to detect DM particles and potentially providing insights on their nature.

The *Cryogenic Rare Event Search with Superconducting Thermometers* (CRESST) experiment, which is part of the direct detection effort, uses highly radiopure detector crystals, equipped with transition edge temperature sensors, to look for elastic scatterings of DM particles off atomic nuclei in the target crystals, and is introduced in detail in Chapter 2. To improve the sensitivity of direct search experiments such as CRESST, it is pivotal to have a comprehensive understanding of the non-DM backgrounds that are recorded by the detectors. Only through careful evaluation of the different background components can their origins be understood, allowing to consider them in the analysis, and guiding the development of improved detectors.

This work focuses on the analysis of radioactive backgrounds in detectors of CRESST’s “Run36” data taking campaign. Chapter 3 gives an overview over well-established analysis procedures, as well as special techniques developed to investigate highly energetic backgrounds, with deposited energies ranging from tens of keVs to MeVs. As the concerned detectors are optimised for performance at considerably lower energies, these approaches provide an important extension of the energy range available to background analyses that is not achievable by standard methods. The resulting background spectra are presented

along with the specifics of the conducted analysis steps in Chapter 4. Finally, the Conclusion (Chapter 5), summarises the findings of this work and offers perspectives for future investigations.

## 1.1. Evidence for Dark Matter

In this Section, some of the most prominent evidence for DM is presented in a non-exhaustive manner, proceeding roughly from smaller to larger length scales.

### 1.1.1. Galactic Rotation Curves

On the scale of individual galaxies, the dynamics of stars orbiting around galactic centres cannot be explained by general relativity, considering the luminous matter only. In a spiral galaxy, with most of the visible matter concentrated in a central bulge, the Newtonian approximation to general relativity can be utilised to estimate the orbital velocity  $v$  of a star at a distance  $r$  from the galactic centre. The centripetal force is given by the gravitational attraction to the mass  $M(r)$  within the star's orbital radius:

$$\frac{mv^2}{r} = \frac{GmM(r)}{r^2}, \quad (1.1)$$

where  $m$  is the mass of the star and  $G$  the gravitational constant. Following the shell theorem [1], the details of a rotationally symmetric mass distribution enclosed by the orbit do not need to be considered. Simplifying the above equation yields

$$v(r) = \sqrt{\frac{GM(r)}{r}}, \quad (1.2)$$

an approximation to the rotation curve of the galaxy expected from the distribution of luminous matter. When most of the galaxy's mass is concentrated in the bulge,  $v(r) \sim 1/\sqrt{r}$  for stars outside of the bulge. More accurate models of the visible mass distributions in spiral galaxies include the mass of the galactic disk and of interstellar gas into the calculations. The resulting rotation curve will not exactly follow  $1/\sqrt{r}$ , but will still fall towards larger radii due to the relatively high density in the central region.

In a 1970 paper, Rubin and Ford published rotation curves of the Andromeda galaxy that are in clear disagreement with this prediction, because they are relatively flat at large distances [12]. These observations were facilitated by a novel spectrograph developed by Ford, which enabled precise spectrography of separate emission regions within the galactic disk. In the further course, many more galactic rotation curves were examined and shown to be similarly flat [13–15], as depicted in Figure 1.1. Comparing with eq. 1.2, this can be achieved only if  $M(r) \sim r$ , requiring large and massive DM halos in the outer parts of galaxies. When the masses of the bulge, disk, interstellar gas and DM halo are included in the models, good fits to the observed rotation curves can be obtained [16, 17].

Apart from investigations of spiral galaxies, the velocity dispersions of elliptical galaxies and globular clusters have been studied as well, similar to the analyses discussed in Section 1.1.2, substantiating the need for DM also in these systems [18, 19].

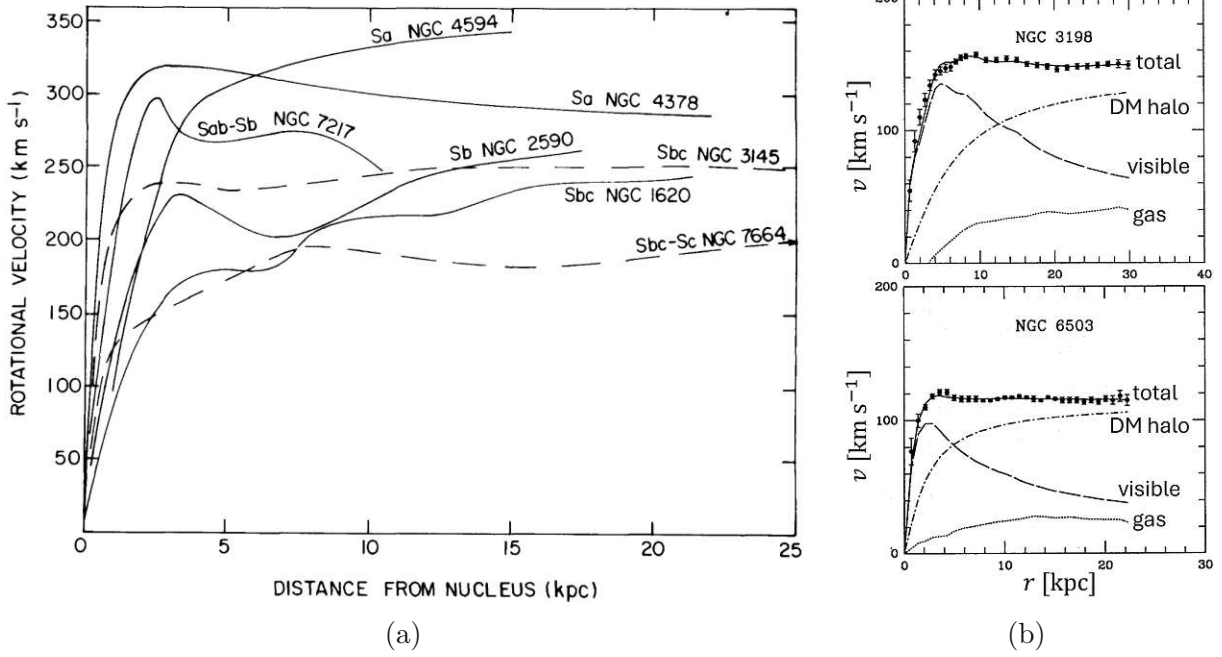


Figure 1.1.: (a) Smoothed measured rotation curves of seven high-luminosity spiral galaxies, taken from [13]. (b) Measured rotation curves for two spiral galaxies (data points with error bars) together with fitted contributions from visible components (dashed lines), gas (dotted lines) and DM halos (dash-dotted lines), as well as the fit totals (solid lines), adapted from [17].

### 1.1.2. Galaxy Cluster Dynamics

In 1933, Fritz Zwicky was one of the first to discuss dynamical evidence for DM, examining the Coma galaxy cluster [20]. From the cluster’s cosmological redshift  $z$ , he obtained its distance from Earth using the Hubble-Lemaître law [21, 22],

$$v = H \cdot d, \quad (1.3)$$

with the apparent radial velocity  $v$  of the cluster relative to Earth, its distance  $d$  and the Hubble parameter  $H$ . Viewing  $z$  as a Doppler shift, the relation between  $v$  and  $z$  is given by the relativistic Doppler effect, which holds for electromagnetic radiation [23]:

$$z = \frac{f_e}{f_o} - 1 = \gamma(1 + \beta \cos \varphi) - 1. \quad (1.4)$$

$f_{e/o}$  denotes the frequency emitted/observed by the source/observer,  $\varphi$  is the angle between the direction of movement of the source and the line of sight from observer to source as measured in the observer’s frame of reference, and  $v$  (which need not be in radial direction here) is contained in  $\beta = \frac{v}{c}$  and  $\gamma = \frac{1}{\sqrt{1-\beta^2}}$ , with the speed of light in vacuum  $c$ . For radial movement,  $\varphi = 0$  simplifies the calculations, and

$$z \approx \frac{v}{c} \quad (1.5)$$

for non-relativistic radial velocities  $v \ll c$ . This relation allows to also calculate the individual velocities of the cluster’s constituent galaxies, yielding a velocity dispersion,

which quantifies the relative velocities between the galaxies and thus the kinetic energy of the cluster.

Zwicky estimated the visible mass of the cluster from its measured brightness and distance, calculating the averaged potential energy  $E_p$  of the system. Employing the virial theorem due to Rупolph Clausius [24], he found the cluster’s expected averaged kinetic energy  $E_k$  according to

$$E_k = -\frac{1}{2}E_p. \quad (1.6)$$

The virial theorem is valid for systems in stationary motion (where the galaxies stay bound in the cluster) and potentials of the form  $V \sim \frac{1}{\text{distance}}$ , such as the gravitational one. The expected velocities of the cluster’s galaxies relative to each other that follow from this calculation are much smaller than the actually observed radial velocity dispersion as measured via Doppler shift. This led Zwicky to the insight that DM has to be present in the Coma cluster, although it is apparent from a later publication that he thought of DM as being composed of “cool and cold stars, macroscopic and microscopic solid bodies, and gases” [25]. His estimated ratio of gravitational mass to luminous mass of at least 400 was too large, partly because of the value  $H_0 = 588 \text{ km s}^{-1} \text{ Mpc}^{-1}$  for the Hubble constant used. Compared to currently accepted values, which are around  $H_0 \approx 70 \text{ km s}^{-1} \text{ Mpc}^{-1}$  [26, 27], this resulted in an underestimation of the cluster’s distance and consequently of its luminosity (from measured brightness and distance), visible mass and ultimately potential energy. More recent works place the amount of DM in the Coma cluster at 85% of its total mass, corresponding to a ratio of about 7 of gravitational mass to luminous mass [28]. Other dynamical analyses yield comparable results for different galaxy clusters [29, 30].

### 1.1.3. Intracluster Medium

Most of a cluster’s baryonic material is in fact contained not within the stars and galaxies of the cluster but rather in the *intracluster medium* (ICM), which permeates the space between the galaxies. The ICM is a hot, X-ray emitting plasma consisting mainly of fully ionised hydrogen and helium [31]. For undisturbed clusters that are not undergoing collisions, hydrostatic equilibrium of the ICM can be reasonably assumed, with the pressure of the plasma counterbalancing gravitational attraction. The distribution of gravitational mass can then be inferred from the ICM’s temperature and density, which in turn are observable through the X-radiation emitted by the plasma [32]. The resulting estimates of total cluster masses are generally in good agreement with those obtained by other methods and again confirm the need for DM [31].

### 1.1.4. Gravitational Lensing and Cluster Collisions

General relativity posits that mass, or equivalently energy, causes a curvature in space-time. It accordingly entails that travelling light is deflected gravitationally by masses close to its trajectory, where the angle of deflection is given by [33]<sup>1</sup>

$$\theta = \frac{4GM}{c^2 b}, \quad (1.7)$$

<sup>1</sup>A factor of 2 is missing in equations (70a) and (74) of the original 1916 article [33]. Explicitly calculating the deflection angle for a light ray passing by the Sun, Einstein evidently used an additional factor of 2, showing that this is just a misprint. For the corrected version, see [34] or [35].



shows the by far larger mass fraction to be located in the proximity of the galaxies [40], as visualised in Figure 1.2. This can be explained by a dominating collisionless DM component, which unlike the ICM was not slowed down during the merger. Similar observations have been made for other systems of galaxy clusters undergoing merging [41–43].

### 1.1.5. Cosmic Microwave Background Radiation

In the early and hot universe, photons frequently scattered on free electrons, which were unable to form stable atoms with baryons due to the high temperature. As the universe expanded and cooled, atoms were formed, removing most of the free charges and consequently making the universe largely transparent to photons by drastically reducing their scattering probability. Since this decoupling event, which happened approximately 380 000 years after the Big Bang [27, 44], further cosmic expansion has redshifted the freely streaming photons to the microwave band. Being present in all of the cosmos, the resulting radiation is called *cosmic microwave background*, or CMB for short, and its spectrum very precisely resembles that of an ideal black body at a temperature of about  $T_{\text{CMB}} \approx 2.72 \text{ K}$  [45]. Albeit it is extremely uniform, there are small temperature variations present in the CMB, which, since its 1965 discovery by Penzias and Wilson [46, 47], have been studied in increasing detail by a series of experiments [48]. The most obvious deviation from isotropy comes in the form of a dipole and is caused by Doppler shift due to the movement of our solar system relative to the frame of reference in which this shift is not present (this could be called the “rest frame” of the CMB). After correcting for this effect, and for the impact of matter in our galaxy on the microwave spectrum, the remaining anisotropies are on the order of hundreds of  $\mu\text{K}$  [49], as shown in Figure 1.3a. Expanding the CMB temperature in spherical harmonics  $Y_{lm}(\theta, \varphi)$  as

$$T_{\text{CMB}}(\theta, \varphi) = \sum_{l=0}^{\infty} \sum_{m=-l}^l a_{lm} Y_{lm}(\theta, \varphi) \quad (1.8)$$

encodes the angular dependencies on  $\theta$  and  $\varphi$  in the expansion coefficients  $a_{lm}$ . The angular power spectrum of the temperature fluctuations can then be obtained as

$$C_l = \frac{1}{2l+1} \sum_{m=-l}^l |a_{lm}|^2. \quad (1.9)$$

Understanding the CMB anisotropies as stemming from acoustic oscillations of the photon-electron-baryon plasma, which were frozen in at the time of decoupling, information about the curvature of the universe, the baryon density and the DM density can be extracted from an analysis of the acoustic peaks in the power spectrum that are depicted in Figure 1.3b. The *Planck* collaboration estimates DM to account for approximately 26 % of the energy content of the universe, while baryonic matter makes up about 5 % [27].

### 1.1.6. Structure Formation

CMB measurements show that the photon-electron-baryon plasma at the time of decoupling was very evenly distributed across the universe, with only small variations in temperature and density. Today, in contrast, matter is arranged in galaxy filaments consisting of galaxy clusters, separated by voids containing only small amounts of matter. To

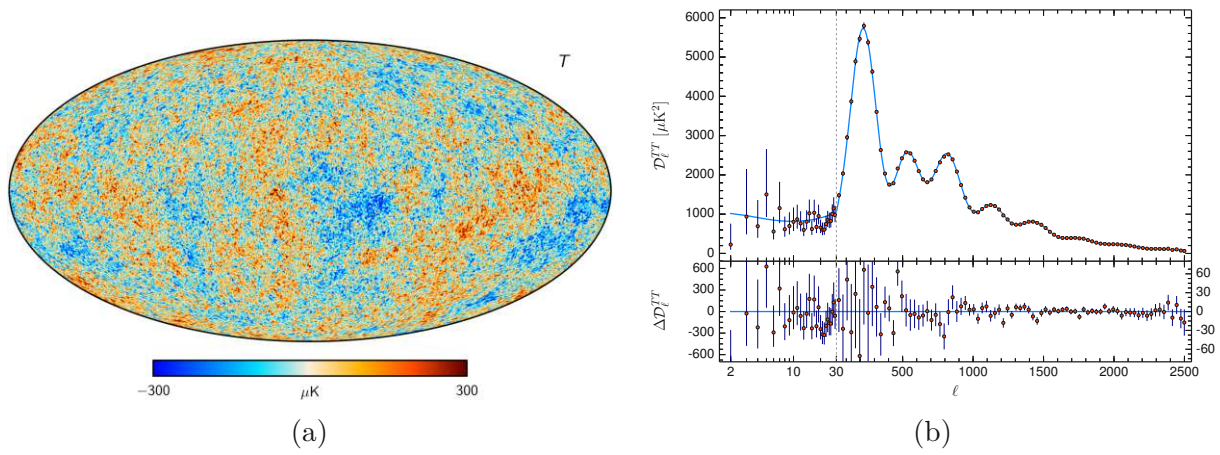


Figure 1.3.: (a) Reconstructed temperature map of the CMB as measured by the *Planck* experiment, where the monopole and dipole component were subtracted and cleaning was performed to remove imprints of regions with bright emission and point sources. Taken from [50], published in [49]. (b) Angular power spectrum of the CMB temperature. Experimental data points with error bars are shown together with a best fit (solid line). The lower panel shows the residuals with respect to this model. Taken from [27].

explain how the initially minuscule density fluctuations evolved into these large structures through gravitational action, the inclusion of DM into the models is once again necessary. Due to electromagnetic coupling to photons, the growth of baryonic density fluctuations in the early universe was inhibited by radiative pressure, while DM did not experience such a force counteracting gravity. The hence formed accumulations of DM provided potential wells for ordinary matter to fall into after recombination, kick-starting its condensation into galaxies and clusters [51]. Large numerical calculations, like the *Millennium Simulation* [52] support this notion and allow to compare DM models to observations.

## 1.2. Dark Matter Candidates

Trying to explain the invisible matter that seems to be the cause for a wide range of observed phenomena, various ideas have been put forth. In the following, the necessity of non-baryonic DM is justified and some well-motivated contenders are briefly discussed.

### 1.2.1. Modified Theories of Gravity

Since all evidence for DM is of gravitational nature, it has been a popular proposition that instead of pointing to the existence of invisible mass, observations could actually be indicating that our current best understanding of gravity, provided by general relativity, is incomplete. One attempt to find an alternative description of gravity that can explain flat galactic rotation curves is known as *Modified Newtonian dynamics*, or MOND [53]. It assumes a gravitational force law of

$$\frac{GMm}{r^2} = ma \cdot \mu\left(\frac{a}{a_0}\right), \quad (1.10)$$

with the mass  $m$  and acceleration  $a$  of the object in question, its distance  $r$  from the mass  $M$  exerting gravitational attraction, Newton’s constant  $G$ , a constant  $a_0$  and some function  $\mu$  satisfying

$$\mu(x \gg 1) \approx 1, \quad \mu(x \ll 1) \approx x. \quad (1.11)$$

The conditions 1.11 ensure that Newtonian behaviour is reproduced for large  $a$ , while leading to different results for small  $a$ , such as on the galactic scale. Building on MOND, further developments have seen the formulation of more advanced theories, including *Tensor-vector-scalar gravity* [54], a relativistic framework for modified gravity. Despite being able to explain galactic dynamics, all these approaches face severe difficulties with respect to other observations. Even with MOND, DM is still required on the scale of galaxy clusters [55, 56], although to a lesser extent. Furthermore, the lensing effects associated with systems of colliding clusters (see Section 1.1.4) likely cannot be explained by modified theories of gravity [40].

## 1.2.2. Baryonic Dark Matter

Assuming DM to be made of the same fundamental building blocks as regular matter would be the most natural course of action. Because the main share of ordinary matter’s mass stems from protons and neutrons (electrons being much lighter), it is referred to as baryonic matter in cosmological contexts. Cluster collisions are not compatible with DM in the form of diffuse gas clouds, as gas is slowed down during the collisions, while the DM component appears to move at least mostly without friction [40–43]. In addition, large amounts of gas should be detectable either through emission or absorption of electromagnetic radiation [57]. Contrarily, objects like black holes, neutron stars, brown dwarves, dim stars or planetary bodies could potentially be dark enough to evade detection and would not be slowed more than stars during cluster collisions. Collectively referred to as *massive compact halo objects* (MACHOs), they have been considered as a solution to the DM problem. However, MACHOs would cause detectable microlensing events, momentarily enhancing the brightness of background sources. As lensing surveys have not found sufficiently many of these signatures to explain DM through MACHOs of a large mass range [58, 59], they are no longer widely accepted as a viable DM candidate. More evidence in disfavour of baryonic DM comes from the CMB power spectrum (see Section 1.1.5), whose acoustic peaks demand substantial quantities of matter that did not interact significantly with the photon-electron-baryon plasma except via gravity [27]. Moreover, Big Bang nucleosynthesis, a model that explains the abundance of light nuclei, puts limits on the overall baryon density in the universe [60, 61]. If there were considerably more baryons, the observed prevalence of isotopes like  $^4\text{He}$  and  $^2\text{H}$  would contradict the theoretical expectations.

## 1.2.3. Neutrinos

Apart from baryons, the SM offers another stable particle candidate for DM<sup>2</sup>: neutrinos. These light elementary particles “have the undisputed virtue of being known to exist” [62], setting them apart from many other particle candidates for DM. Additionally, neutrinos interact only through gravity and the weak force. Still, there are also problems when

<sup>2</sup>Second and third generation charged fermions decay into lighter SM particles, as do the W, Z and Higgs bosons. Photons, as the quanta of the electromagnetic field are inherently not dark. Gluons interact strongly and are confined (in baryons) due to their colour charge.

trying to explain DM with SM neutrinos. For one, the Pauli exclusion principle limits the number of fermions that can be contained in a given volume of phase space. Since neutrinos have only very small masses [63], they are unable to provide the required gravity for galactic halos even at their maximum possible density [64]. Apart from that, as another consequence of their small masses, neutrinos travel at relativistic speeds and would constitute *hot DM*, which cannot explain the kind of structure formation that is seen in the universe [65]. Although this rules out SM neutrinos as the main component of DM, their mysteriously small masses (as compared to the other SM particles) might hint at the existence of so far unseen neutrino species. Other than the rest of the SM fermions, neutrinos are only ever observed to be of left-handed chirality, motivating the existence of “sterile” right-chiral counterparts, which would only interact gravitationally. Explaining the neutrino masses – themselves already an extension to the SM – by the *seesaw mechanism* [66] results in large mass terms for the sterile neutrino species, making them a promising DM candidate that is actively being searched for [67].

### 1.2.4. WIMPs

Another class of hypothesised DM particles with high theoretical plausibility is known as *weakly interacting massive particles* (WIMPs). As such, these particles couple to ordinary matter only through gravity and some form of weak interaction, be it the weak nuclear force of the SM or some as of yet unknown interaction. Astonishingly, early-universe thermal production of a particle with mass  $\sim \mathcal{O}(100 \text{ GeV}/c^2)$  and interaction cross sections  $\sim \mathcal{O}(\text{pb})^3$ , typical for the electroweak scale, would have resulted in a present-day relic density capable of explaining DM [68]. By involving a novel force in the interaction between WIMPs and SM particles, the range of possible WIMP masses can be extended to lower values [68]. In models of *supersymmetry*, which assign a supersymmetric partner to each SM particle, WIMPs are often predicted. If R-parity<sup>4</sup> is assumed to be conserved, the lightest supersymmetric particle is stable and can serve as DM [69]. Apart from supersymmetry, WIMPs are also a part of other extensions to the SM, including theories of universal extra dimensions [70] or little Higgs models [71]. The resulting broad motivation for WIMPs along with their in principle detectable nature make them particularly interesting candidates for DM.

### 1.2.5. Axions

Weak interactions have been shown to violate *CP-symmetry* [72, 73], the invariance of physics under the combined operations of charge conjugation (exchanging particles for their antimatter counterparts and vice versa) and parity transformation (inversion of spacial coordinates). Within the framework of the SM, there is no good reason why the strong interaction should not also exhibit CP-violation. This would lead to an electric dipole moment of the neutron, which is contradicted to high precision by experiments [74]. To resolve this tension, known as the *strong CP problem*, particles called axions have been proposed [75–77]. If they were present in adequate abundance, axions could make up DM, seeing as they could be stable, non-relativistic, and interacting extremely weakly with ordinary matter [78].

<sup>3</sup>The barn b is a unit of area commonly used for cross sections.  $1 \text{ b} = 10^{-28} \text{ m}^2 \rightarrow 1 \text{ pb} = 10^{-40} \text{ m}^2$ .

<sup>4</sup>R-parity distinguishes SM particles, with R-parity +1, from their supersymmetric partners, with R-parity -1.

## 1.3. Dark Matter Searches

The manifold evidence for DM in conjunction with the varied attempts to explain it has prompted an extensive search program aiming to detect DM in a non-gravitational way and determine its nature. Given that DM does couple to SM particles other than via gravity, three different approaches are apparent, as illustrated in Figure 1.4. Direct detection searches for a signal produced by scattering of DM particles off a target, leading to energy depositions in the detector. The complementary method of indirect detection is looking for SM products of DM annihilations or decays, while collider searches operate in the opposite direction, seeking signatures of DM produced in high-energy collisions of SM particles. Detailed information can be found in the main sources for the following section, [9–11], and the references therein.

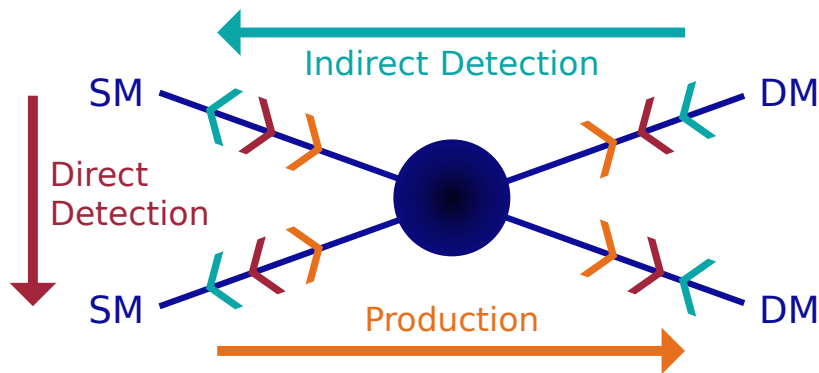


Figure 1.4.: Diagram showing how different DM search approaches investigate different manifestations of the interaction between SM and DM particles, where the direction of time follows the arrow for each case. The blob represents the unknown interaction of the four involved particles.

### 1.3.1. Direct Detection

Several strategies for direct detection experiments have been devised, making use of a line of physical processes that are initiated by the scattering of particles on the experimental target. In general, using heavy nuclei in the target offers a larger cross section for nuclear scattering [79], while lighter nuclei improve the sensitivity to lower particle masses due to the kinematics of elastic scattering. Searching for DM particles which interact with the spin of unpaired nucleons motivates the incorporation of nuclides with a non-zero nuclear spin into the targets [80].

Noble liquid detectors utilise liquefied, cryogenic Ar or Xe as their targets, usually monitoring large tanks containing target masses up to multiple tons. Particles scattering on the atoms of the liquid cause the emission of scintillation light that can be measured with photomultiplier tubes (PMTs). Additionally occurring ionisations of the target atoms offer a second detection channel. To exploit it, an electric field is applied, directing the electrons produced in ionising interactions towards the rim of the tank, where they too can be detected. Because electron recoils generate a higher ionisation signal than nuclear recoils, in relation to the scintillation light produced, the usage of both signals allows to discriminate between the two event classes, facilitating background reduction.

Another type of direct detection experiments are bolometers, cryogenically operated solid state detectors that take advantage of the small heat capacity of their target crystals at low temperatures. Using precise thermometers, they are built to register tiny temperature changes in the target and by this means quantify energy depositions caused by particle-target interactions. Similar to noble liquid detectors, it is also beneficial for bolometers to use an additional detection channel, which can come in the form of an ionisation signal for targets made of silicon or germanium, or scintillation light in the case of transparent scintillator targets like bismuth germanium oxide (BGO) or calcium tungstate ( $\text{CaWO}_4$ ).

Other experiments with crystalline targets choose to focus solely on ionisation charges or scintillation light, disregarding the heat signal. Further, there are bubble chamber detectors that detect absorbed energy through gas bubbles forming in a superheated liquid, with cameras recording photographs of the bubbles.

Striving to observe mostly nuclear and in some cases electron recoils of DM particles, all direct detection methods so far depend on DM interacting with ordinary matter through some force other than gravity. As this is not guaranteed, an interesting future development could be the construction of DM detectors relying solely on gravitational interactions, which would be capable of detecting (or ruling out) DM candidates with extremely high masses  $\geq 10^{19} \text{ GeV}/c^2$ , according to a current projection [81].

### 1.3.2. Indirect Detection

The anticipated signals for indirect DM detection are SM particles stemming from the decay or annihilation of DM particles somewhere in the not too far cosmic neighbourhood. The most frequently examined cosmic rays for this purpose comprise  $\gamma$ -rays, neutrinos and antimatter. Likely places of origin and consequently favoured observational targets generally include all locations where high concentrations of DM are expected, such as the galactic centre of the Milky Way, its halo or satellite galaxies, as well as the nearest neighbouring galaxies and clusters.  $\gamma$ -rays and neutrinos travel through the universe largely unimpeded and are thus easier to trace back to their source than charged particles, which are deflected by electromagnetic fields.

Because the Earth's atmosphere is opaque to high-energy photons,  $\gamma$ -ray telescopes have to be either space-based or monitor atmospheric showers induced by high-energy interactions at the top of the atmosphere. Air showers can be observed by optical telescopes through the Cherenkov or fluorescence light that they generate in the atmosphere, and via detecting the secondary particles reaching the ground. From the shape of the shower, it is possible to deduce the main mode of interaction of the primary particle (electromagnetic or strong), eliminating the hadron background.

Neutrino detectors commonly employ large numbers of PMTs spread over a considerable volume of (liquid or frozen) water. Neutrinos interacting with the water can produce charged leptons travelling at relativistic speeds, which then in turn emit Cherenkov radiation that the PMTs register. Because neutrino interactions are exceedingly rare, it is of utmost importance to instrument large volumes of water, with the IceCube Neutrino Observatory [82] watching a cubic kilometre of ice, for example. Another main concern for neutrino telescopes is the shielding from atmospheric muons, which can be achieved by placing the PMTs deep beneath the surface of the water used, or by positioning the

experiment underground. Focusing on signals of neutrinos coming from below even allows to use the entire Earth as shielding against unwanted backgrounds. Observational targets uniquely available to neutrino detectors are the insides of the Sun and the Earth, where DM particles could accumulate after scattering with constituents of these massive bodies.

Apart from highly energetic  $\gamma$ -rays and neutrinos, antimatter is investigated as a conceivable indication for DM. If an excess of antimatter above the otherwise expected amounts was observed, it could be due to the decay or annihilation of DM. Experiments looking for this effect have to be situated above most of the atmosphere to be able to detect antimatter originating from outer space, which is why they are carried by satellites or stratospheric balloons.

A persistent problem with any indirect detection method lies in the difficulty of interpreting any observed signal without doubts. On the one hand, there are known astrophysical objects, such as neutron stars, that are recognised or at least considered for producing the kinds of particles that were discussed. On the other hand, there may be entirely unknown phenomena capable of mimicking an indirect DM signal. Direct detection experiments and collider searches are conducted in a controlled laboratory environment and do not face these concerns

### 1.3.3. Collider Searches

In the high-energy collisions of SM particles (most often protons or electrons and positrons) at particle colliders, all kinds of elementary particles are produced and available for detailed study. Many of the particles known today were first discovered using this approach [83]. The accessible mass range is determined by the centre-of-mass energy of the collider, while the probability of producing a certain particle depends on the couplings involved, among other things. If DM particles have a mass that can be reached at current accelerators, and if they have sufficient couplings to the SM, they should be produced and leave characteristic signatures in the data recorded by collider experiments. Because they interact at most very weakly with the detector materials, one possible indicator of produced DM is a large amount of missing transverse momentum (or “transverse energy”), which goes along with a particle leaving the experiment undetected. Since the ascertainment of such an event requires at least some detectable signal, the sought-after scenarios include initial state radiation, leading to monojet events.

As for the other classes of DM searches, backgrounds are a major issue. In the case of collider searches, they stem from SM processes that result in the examined experimental signatures, obscuring a possible DM signal. For instance, a final state containing neutrinos can lead to a large amount of missing transverse momentum. A precise knowledge of background processes is therefore crucial, enabling the search for an excess above SM expectations. However, even if evidence for the production of an unknown particle were to be found at a collider experiment, it could prove difficult to study some of its important properties, like its lifetime. Consequently, the confirmation of any discovery via direct and/or indirect detection would still be of great importance.

### 1.3.4. Current Status

So far, no definitive discovery of DM has been made. Although there are claims of a scintillator-observed annual modulation signal as a possible indication of DM [84], other experiments either contradict or fail to replicate this signal [9], with further investigations to come [85]. Indirect detection experiments report excesses in high-energy cosmic rays and antimatter, but in view of uncertain astrophysical backgrounds, these present no conclusive evidence for DM decays or annihilations [10].

In the absence of a clear signal, progress can still be made by the calculation of *exclusion limits*. Using models for the local DM density in our region of the Milky Way, the number density of DM particles can be found for a given particle mass. With the help of additional astrophysical input, like the conjectured velocity distribution of the DM halo, the expected rate and energy of events in direct detection experiments can be related to the DM-nucleon interaction cross section and the DM particle mass. If no signal of this energy is observed, a statistical upper limit can be placed on the interaction cross section for the assumed mass, excluding a portion of the allowed parameter space for particle DM. Figure 1.5 shows the exclusion limits obtained by several direct detection experiments for a selected mass range. Similar limits can be found from indirect and collider searches, enabling a comparison and complementation of the different approaches. In the end, any future discovery will have to be studied in different channels. Direct detection will most likely be needed to provide conclusive proof for a discovery of a DM particle. Collider data can potentially provide a deeper understanding of the interactions of DM particles. Lastly, indirect detection could be the link to astronomical observations, confirming that the candidate in question is indeed responsible for the gravitational effects of DM [11].

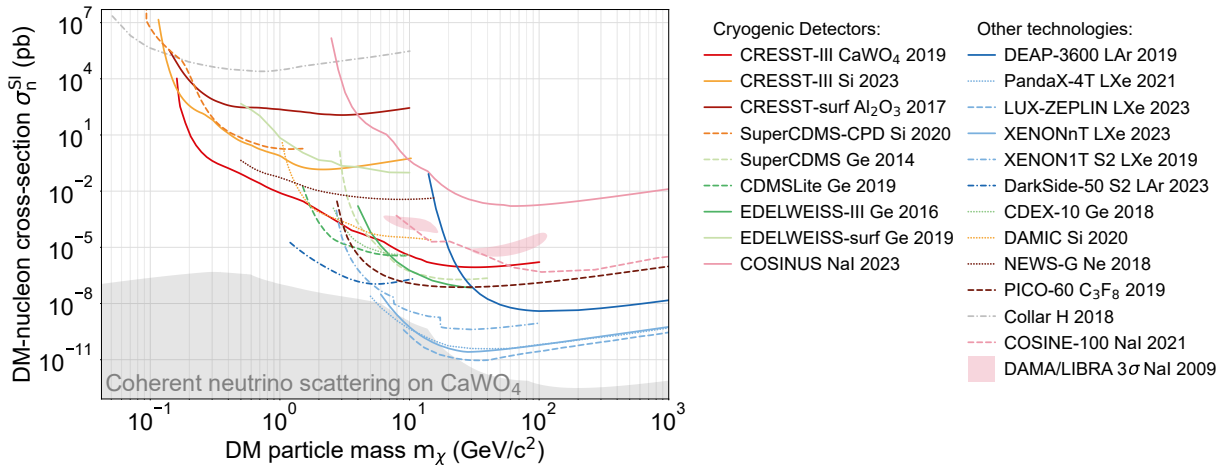


Figure 1.5.: Upper limits on the spin-independent DM-nucleon interaction cross section from various direct detection experiments with different target materials. The shaded red area marks parameter pairs compatible with the positive annual modulation signal reported by the DAMA/LIBRA experiment. The shaded grey area shows the *neutrino floor* or *neutrino fog* for a calcium tungstate target; the region where coherent scattering of solar and atmospheric neutrinos on the nuclei of this target becomes statistically significant, making DM detection significantly harder or even impossible. Taken from [86].

# 2. THE CRESST EXPERIMENT

The Cryogenic Rare Event Search with Superconducting Thermometers (CRESST) experiment is part of the direct DM detection effort, focuses on low DM masses, and is one of the leading experiments in the sub-GeV/ $c^2$  mass regime (see Figure 1.5). As implied by its name, CRESST employs cryogenic detectors based on bolometer crystals, using heat and scintillation light as detection channels. Limiting the interactions of SM particles with the detectors is paramount in achieving a high sensitivity for DM, as a possible signal is extremely faint. Consequently, understanding and reducing the background is a major part of the experimental effort.

## 2.1. Experimental Setup

Apart from the detectors and their readout electronics, the CRESST experimental setup comprises a number of other components, such as shieldings and a cryogenic system, which are discussed in this section.

### 2.1.1. Radiation Shieldings

CRESST is situated in *Hall A* of the *Laboratori Nazionali del Gran Sasso* (LNGS) underneath the Gran Sasso massif in central Italy. Shielded from cosmic radiation by a rock overburden of approximately 1400 m, corresponding to roughly 3800 m water equivalent, the LNGS experimental halls benefit from a reduction in muon flux by a factor of about  $10^6$ , as compared to the surface [87]. To attenuate or veto any remaining radiation of cosmic or terrestrial origin, the detectors are surrounded by several layers of passive and active shieldings. A Faraday cage is placed around the entire assembly for the reduction of electromagnetic interference [88]. Figure 2.1 shows a cross-section of the experimental setup, including the detectors, cryogenics and shielding systems. The outermost layer of the latter (after the Gran Sasso rock) consists of 45 cm of polyethylene [89] and – with its high content of hydrogen – is designed to moderate neutrons stemming from radioactive decays or cosmic rays scattering in the rock. Hydrogen nuclei have practically the same mass as neutrons, maximising the energy transfer in collisions. As a next layer, 20 plastic scintillator panels are installed to veto the remaining muon flux [88], which is on the order of  $3.3 \times 10^{-4} \text{ m}^{-2} \text{ s}^{-1}$  [90] and still has to be considered. The muon panels are instrumented with PMTs [88], and their veto triggers are included in the analysis. Inside the muon veto system lies the second active component of radiation shielding, a gas-tight chamber called the “radon box”. It is continuously flushed with clean nitrogen gas, creating a light overpressure, to prevent naturally occurring radioactive radon from accumulating in the vicinity of the detectors [89]. Enclosed by the radon box, there are several layers of passive shielding, mostly metal. Lead of 20 cm thickness [89] is used to provide protection against  $\gamma$ -rays. It is especially well suited for this purpose, owing to its high atomic number and density. Even though it is sourced from a specific mine for low inherent radioactivity [89], impurities such as  $^{210}\text{Pb}$  are impossible to avoid completely,

causing  $\alpha$ -,  $\beta$ - and  $\gamma$ -backgrounds in their decays. As a countermeasure, a 15 cm thick [89] radiopure copper layer is placed inside the lead shielding. Unlike lead, copper can be produced with a very low amount of contamination, making it suitable for application close to the detectors. Another 3.5 cm layer of polyethylene with high purity is installed within the copper shielding [91]. This is to mitigate the impact of neutrons that could not be stopped in the outer polyethylene layer, or that are produced in the other shieldings, either from radioactivity or by interactions with muons that pass through the muon veto undetected. Reducing the neutron background is particularly important because neutrons deposit energy in the detectors via nuclear recoil, resembling DM signals.

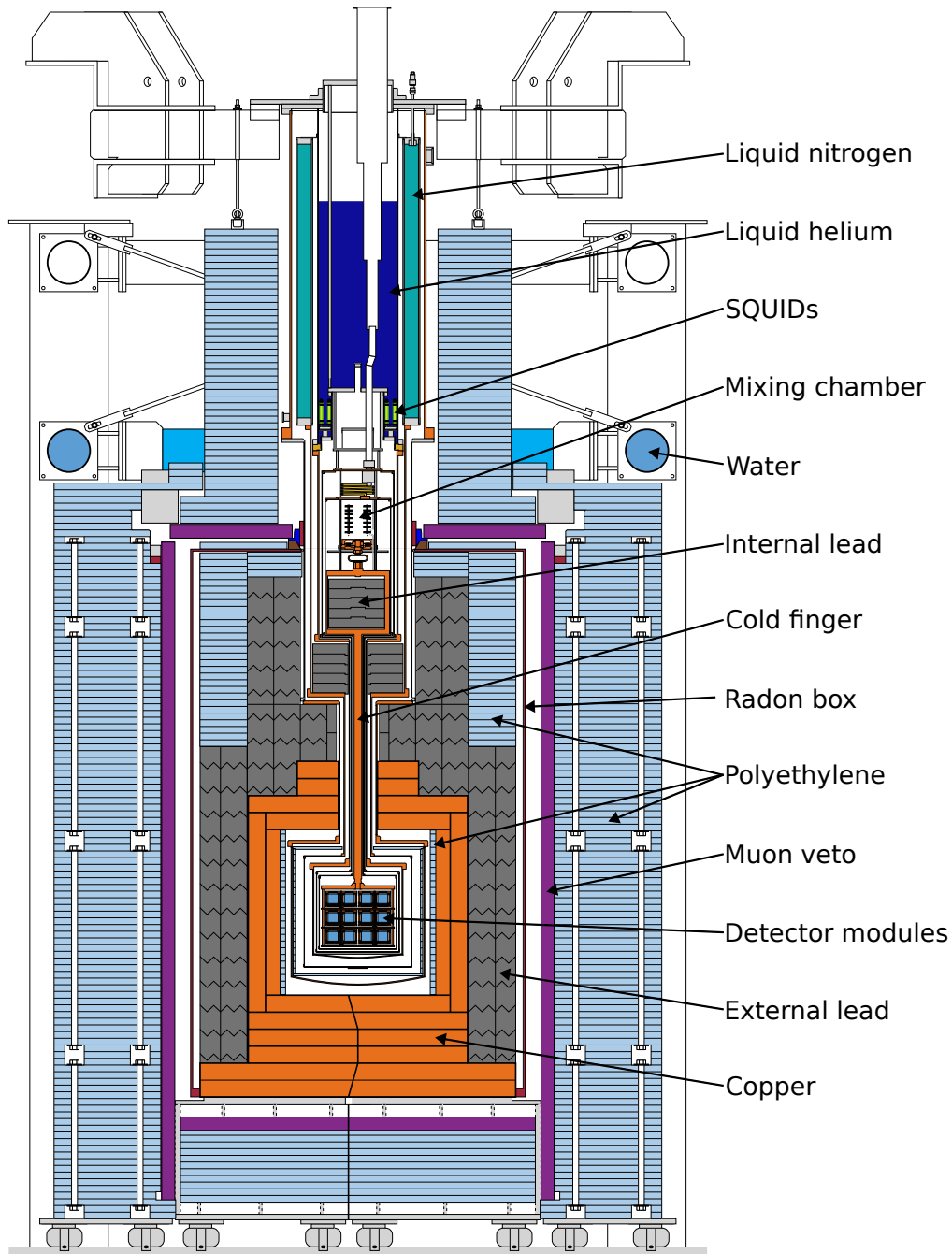


Figure 2.1.: Schematic drawing of the CRESST experiment. The largest part of the hardware is devoted to shielding the detectors at the centre of the setup. Adapted from [92].

## 2.1.2. Cryogenic System

In order to reach the mK temperatures needed for the operation of CRESST’s detectors, a  $^3\text{He}/^4\text{He}$  dilution refrigerator is utilised. This standard cooling apparatus exploits the endothermic dilution of  $^3\text{He}$  into a superfluid  $^4\text{He}$ -rich phase, reaching temperatures around 5 mK (far below the boiling point of either isotope) in the *mixing chamber*, where both isotopes come into contact. A commercial device, the refrigerator is not made of radiopure materials and thus positioned on top of the setup, leaving room for additional shieldings. “Internal” lead is placed below the mixing chamber, leaving no unshielded line of sight between cryostat and detectors. The cooling power is transmitted via a copper can surrounding part of the internal lead and a copper cold finger, establishing a thermal link between the mixing chamber and the detector holding structure. This coupling is weak by design, so that temperature variations of the cryostat are smoothed out, resulting in more stable detector temperatures [93].

## 2.1.3. Detector Holding Structure and Cabling

At the heart of CRESST, the detector modules (described in detail in Section 2.2) are mounted inside a copper structure, called the “carousel” due to its shape. The carousel is placed in a vacuum, attached to the cold finger and enclosed by a series of shieldings, as described above. It can accommodate up to 33 detector modules and is suspended on bronze ( $\text{CuSn}_6$ ) springs to provide damping of external vibrations [93].

The detector operation requires cable connections to be installed between the temperature sensors, the readout system, and the current sources and control electronics outside of the cold volume. For this purpose, flat woven cables are used, where the ones connecting to the sensors are made of superconducting NbTi, clad with a layer of CuNi to ensure an even temperature distribution along the wires. To minimise the heat influx through the cables, they are clamped in several copper heat sinks at progressively colder temperatures from top to bottom. The setup of the cables, connectors and other electronics is highly complex due to the various aspects that have to be considered in order to ensure vacuum tightness, fulfil cryogenic and shielding requirements and comply with the spacial constraints imposed by the experimental geometry [94].

## 2.2. CRESST Detectors

Since CRESST started searching for DM at LNGS in the year 2000 [95], the design of its detectors has seen continuous development and change. In the current CRESST-III phase, where data taking started in 2016 [96], lighter target masses than in previous phases are employed. The data that is analysed in this work stems from the “Run36” data taking campaign, which was carried out between August 2020 and February 2024. The detector modules of this period mostly feature the same basic layout, with differences in the used materials. A description of a typical Run36 module, the detection and readout principles as well as more details on the electronics are given in this section. Information on the module design can also be found in [97] and [98], for instance. Further details of the readout system are delineated in [94].

## 2.2.1. Modules

Figure 2.2 shows an illustrative graphic and a photo of “TUM93A”, a CRESST-III detector module. The production process of TUM93A at the *Technical University of Munich* is described in detail in [99]. Its main absorber crystal is a cuboid made from calcium tungstate ( $\text{CaWO}_4$ ), measures  $20 \times 20 \times 10 \text{ mm}^3$  and has a mass of about 24 g [99]. The scintillation light detector for the second readout channel consists of a 0.4 mm-thick square silicon-on-sapphire (SOS) wafer of 20 mm side length and 0.6 g mass, which is aligned to one of the main absorber’s larger faces. Both detectors are held in place by dedicated holding sticks, made of either  $\text{CaWO}_4$  or copper. The holding sticks are in turn fixed to the solid copper module enclosure with bronze clamps. In order to maximise the light collection efficiency of the light detector, the inside of the copper housing is coated with a reflective and scintillating foil. Both the main crystal and the SOS wafer are equipped with *transition edge sensors* (TESs), allowing for high-precision temperature measurements. While two of the three main absorber’s holding sticks are manufactured from copper, one is made of  $\text{CaWO}_4$  and is additionally instrumented with a TES; it is thus called “i-stick”. Close to each TES, a separate heater is placed on the crystal to allow for temperature control and calibration. Electrical and thermal connections of the TESs are realised through wire bonds to copper bond pads on the enclosure. At the back of the module, a low-activity radioactive  $^{55}\text{Fe}$  source is placed inside the housing, providing X-rays of a known energy for calibration of the detector.

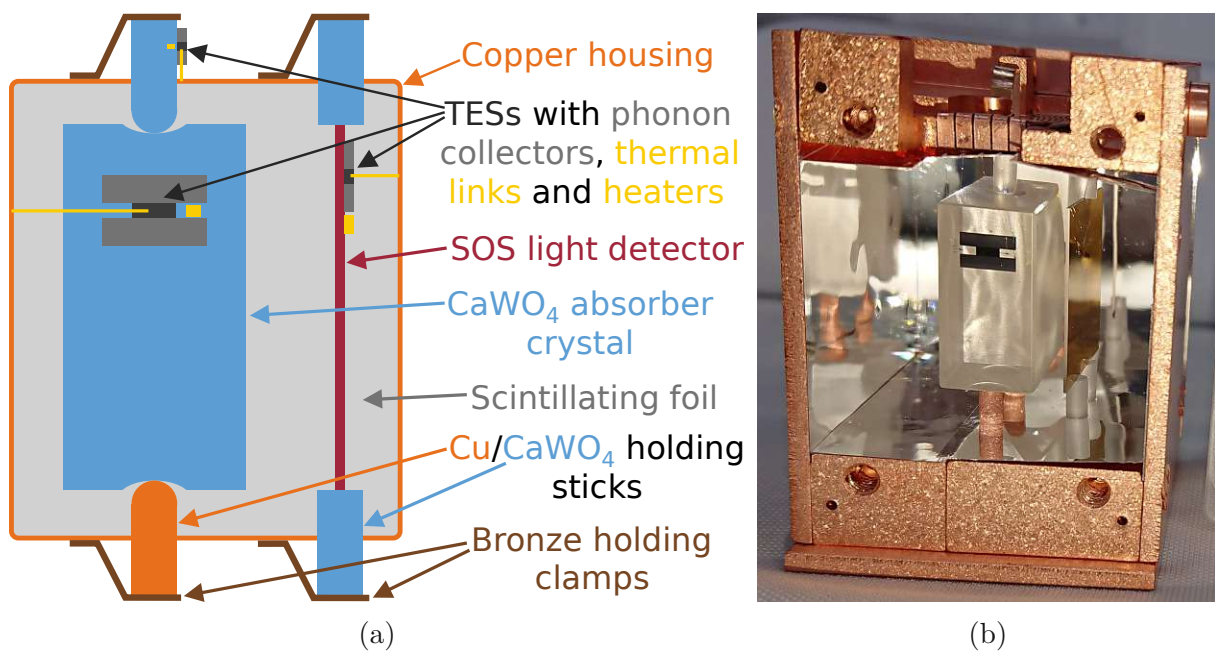


Figure 2.2.: (a) Schematic image of TUM93A. (b) Photo of the open module TUM93A with the copper front plate not attached.

Except for the “Gode” detectors, which are constructed with a beaker-shaped light detector, most Run36 modules feature a geometry similar to TUM93A. However, apart from  $\text{CaWO}_4$ , a row of other absorber materials like sapphire ( $\text{Al}_2\text{O}_3$ ) and lithium aluminate ( $\text{LiAlO}_2$ ) are used, resulting in different crystal masses for the same dimensions. The material of the holding sticks varies between copper and  $\text{CaWO}_4$ , with some crystal

mountings omitting the sticks altogether. A number of modules also forego the scintillating foil coating.

## 2.2.2. Cryogenic Detection Principle and Readout System

When a particle interacts with the absorber crystal, it deposits some energy  $E$ , leading to the generation of phonons and scintillation light. To allow for the latter, a scintillating material such as  $\text{CaWO}_4$  or  $\text{Al}_2\text{O}_3$  is used for the crystal. The phonons, corresponding to a rise in temperature  $\Delta T$  of the absorber, propagate through the crystal and reach the TES, which is thermally coupled to the copper housing and thereby to the thermal bath. A superconductor held at its transition temperature, the TES acts as a thermometer. It is sensitive to minute temperature changes  $\mathcal{O}(10\ \mu\text{K})$ , which are measured by changes in its resistance  $\mathcal{O}(1\ \text{m}\Omega)$  (for more details see Section 2.2.3). Since it measures the phonon response of an event, the main absorber together with its TES is known as the *phonon detector*. By absorption of the scintillation light, the *light detector* similarly experiences heating. Apart from the thermal links of the TESs, the heat also dissipates through the holding sticks, which is used to pick up an additional (phonon-induced) signal in modules with an i-stick.

Cooling the detectors down to temperatures  $\mathcal{O}(10\ \text{mK})$  greatly enhances their sensitivity, because their heat capacity  $C$  scales approximately like  $C \sim T^3$ , as explained by the Debye model [100] at low temperatures. Consequently, the temperature signal roughly follows

$$\Delta T = \frac{E}{C} \sim \frac{E}{T^3}. \quad (2.1)$$

Other than that, cryogenic temperatures are also needed for the utilisation of TESs and for the reduction of thermal noise.

The warming-induced resistance variations of the TESs are made measurable by integrating the latter into an electrical circuit and applying a constant bias current  $I_0$ , as shown in Figure 2.3. Forming a parallel circuit with the TES are an electromagnetic coil of inductance  $L$  and two reference resistors with a total resistance of  $R_R$ , balancing the circuit. The current through the coil  $I_L$  is then given by

$$I_L = I_0 \cdot \frac{R_T}{R_T + R_R}, \quad (2.2)$$

where  $R_T$  denotes the temperature-dependent TES resistance, and the coil generates a magnetic flux

$$\Phi_L = L \cdot I_L. \quad (2.3)$$

This flux is picked up by a *superconducting quantum interference device* or SQUID, a magnetometer of exceptional sensitivity that is more thoroughly explained in Section 2.2.4. All SQUIDS are mounted at the bottom of the cryostat's helium bath, as shown in Figure 2.1, keeping them cooled. Each SQUID converts the flux signal of its input coil to a voltage signal, which is coupled to a feedback coil in order to keep the flux through the SQUID constant. This configuration, known as *flux locked loop*, allows to linearise the SQUID output signal, which is then given by the feedback current necessary to steady the flux. Finally, this output current can be further amplified and converted to a voltage that is recorded for the data analysis.

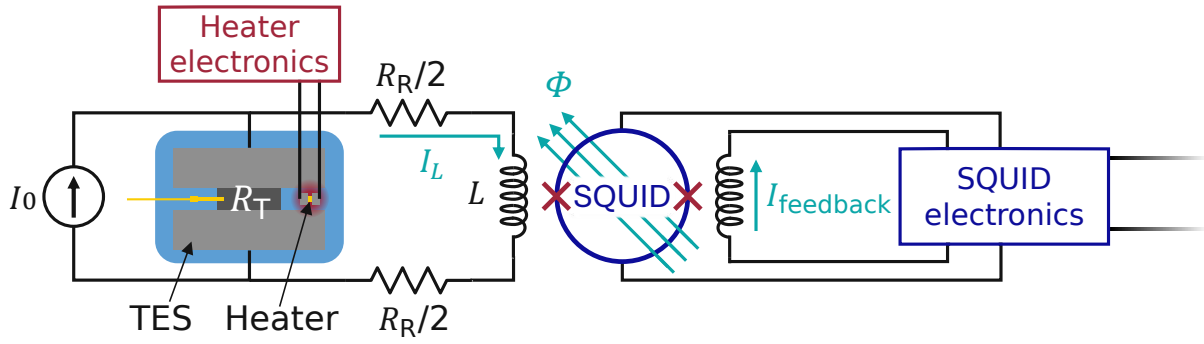


Figure 2.3.: Sketch of the readout system with bias current  $I_0$ , TES resistance  $R_T$ , two reference resistors of resistance  $R_R/2$  each, SQUID input coil with inductivity  $L$ , SQUID input and feedback currents  $I_L$  and  $I_{\text{feedback}}$ , as well as flux through the SQUID  $\Phi$ . The crosses in the SQUID represent Josephson junctions.

To summarise, particle interactions induce a heat signal, either directly or via scintillation light. The heat signal is successively converted to a current by the TESs, to a magnetic flux by the SQUID input coils, to a feedback current by the SQUIDs in flux locked loop arrangements and ultimately to an amplified output voltage by the remainder of the readout electronics.

### 2.2.3. Transition Edge Sensors

A superconductor is a material that, below a critical temperature  $T_c$ , exhibits a vanishing electrical resistance and expels magnetic fields from its interior.<sup>5</sup> Conventional superconductivity is explained by Bardeen-Cooper-Schrieffer (BCS) theory [101] and arises from the binding of electrons into Cooper pairs, facilitated through an effective electron-electron attraction mediated by phonons. As bosons, Cooper pairs can all occupy the same quantum state, which allows them to condense into the superconducting ground state. The resulting energy gap for excitations of individual electrons inhibits their scattering, enabling a collisionless current flow with zero resistance. Thermal excitations of sufficient energy to overcome the energy gap can break up Cooper pairs, leading to a breakdown of superconductivity above the critical temperature. This effect can be utilised to construct very sensitive thermometers, the TESs.

In CRESST-III, the TESs consist of tungsten films with thicknesses on the order of 200 nm [97] and transition temperatures typically between 15 and 30 mK [92]. Aluminium films acting as phonon collectors increase the energy transfer from the phononic to the electronic system, thereby enhancing the signal [97]. Each TES features two aluminium wire bond connections to its phonon collectors, supplying bias current for the TES operation, as well as one thermal link from the tungsten film to the module housing, consisting of a gold stripe and wire bond. Additionally, another gold film is placed on the crystal in vicinity of the TES to serve as an ohmic heater. It is provided with current by a separate pair of aluminium wire bonds, for a total of five connections per TES. By action of the cryogenic system (see Section 2.1.2) and the heater, the TES temperature  $T_T$  is stabilised at a working point (WP) precisely in the superconducting transition of the tungsten film,

<sup>5</sup>To be precise,  $T_c$  is the highest possible transition temperature between superconducting and normal conducting phase. A non-zero current density through and/or a magnetic field around the superconductor lowers the transition temperature, entirely suppressing the transition for large enough values.

making its resistance  $R_T$  highly responsive to temperature variations, as sketched in Figure 2.4. Ideally, the WP is chosen in the steepest part of the transition curve to obtain the best sensitivity. For not too large deviations from the WP ( $T_{WP}, R_{WP}$ ), the TES response is approximately linear:

$$R_T \approx R_{WP} + (T_T - T_{WP}) \left. \frac{\partial R_T}{\partial T_T} \right|_{T_T=T_{WP}} = R_{WP} + \Delta T_T \cdot r, \quad (2.4)$$

with the change in TES temperature  $\Delta T_T := T_T - T_{WP}$  and the slope of the transition curve at the WP  $r := \left. \frac{\partial R_T}{\partial T_T} \right|_{T_T=T_{WP}}$ . This approximation is not valid for large  $\Delta T_T$ , since the transition curve flattens at its top, when the TES enters its fully normal conducting state. The distance of the WP to the point where the TES becomes fully normal conducting defines the maximum possible signal pulse height. A more in-depth coverage of TESs used in CRESST can be found in [91].

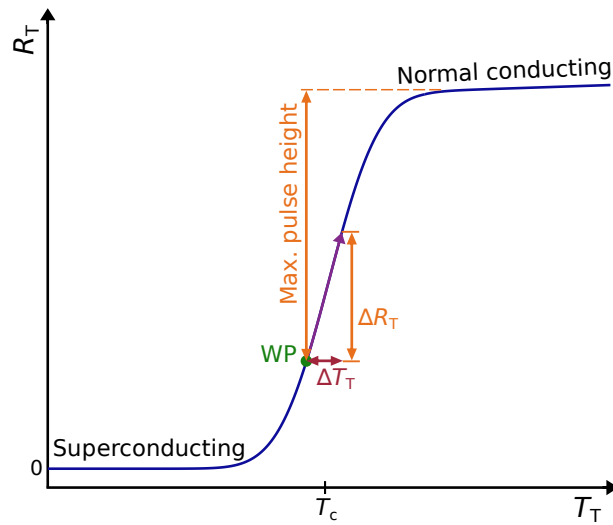


Figure 2.4.: Idealised depiction of a TES transition curve, showing the resistance of the superconducting film dependent on its temperature. Around the working point, temperature differences  $\Delta T_T \mathcal{O}(10 \mu\text{K})$  typically lead to changes in resistance  $\Delta R_T \mathcal{O}(1 \text{ m}\Omega)$  [92]. Adapted from [102].

## 2.2.4. Superconducting Quantum Interference Devices

Since the TES resistance  $R_T$  is  $\mathcal{O}(10 \text{ m}\Omega)$ , the bias current  $I_0$  has to be sufficiently small,  $\mathcal{O}(\mu\text{A})$  [92, 94]. Measuring the consequently even smaller current variations poses a challenge that can be overcome by using SQUIDs. These devices exploit another aspect of superconductivity, namely the *Meissner effect*, which refers to the expulsion of magnetic fields from a superconductor by the generation of screening currents close to its surface [103]. Even though the superconductor, barring the surface layer, is therefore field free, a hole in a superconducting ring can still be permeated by magnetic flux. It can be shown [104] that the flux threading such a loop can only take on integer multiples of the *flux quantum* (FQ)

$$\Phi_0 = \frac{h}{2e} \approx 2.068 \times 10^{-15} \text{ Wb}. \quad (2.5)$$

A direct current (DC) SQUID, as the ones used in CRESST [91], consists of a super-

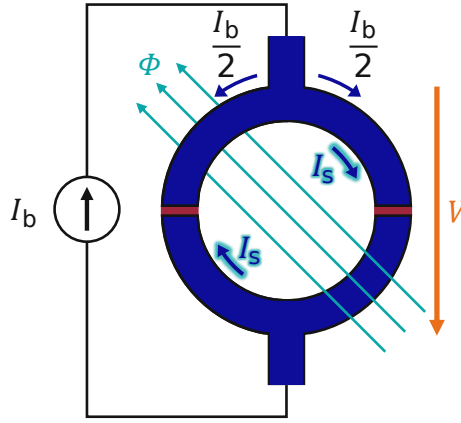


Figure 2.5.: Schematic graphic of a DC SQUID. The superconducting ring (blue) is interrupted by two Josephson junctions (red). The screening current  $I_s$  ensures that the flux through the SQUID  $\Phi$  is an integer multiple of the magnetic flux quantum  $\Phi_0$ . Depending on the bias current  $I_b$  and the externally applied flux, the voltage drop  $V$  across the SQUID can be zero or not.

conducting ring that is interrupted by two non-superconducting *Josephson junctions* (see Figure 2.5). Across these weak links, a supercurrent can still flow without a voltage drop – a quantum phenomenon known as the *Josephson effect*. For currents larger than the *critical current* of the junction, its superconductivity breaks down and unpaired electrons start to tunnel through the gap in addition to Cooper pairs, resulting in a voltage drop [105]. The critical current  $I_c$  of a DC SQUID, where two Josephson junctions are connected in parallel, is given by the maximum bias current for which both junctions remain superconducting. In the absence of screening currents through the loop of the SQUID, and assuming two identical junctions, the SQUID bias current  $I_b$  splits equally into the two branches, leading to a critical current of the SQUID that is twice that of either junction. However, if a magnetic flux  $\Phi_L$  is applied through the ring, an additional circular screening current  $I_s$  is superimposed on the bias current, in general. In one branch,  $I_s$  flows in the same direction as  $I_b$ , while in the other they are of opposite direction, yielding currents  $I_b/2 + I_s$  and  $I_b/2 - I_s$  across the two junctions, respectively. Because of this, the critical current of one of the junctions will in general be reached already for a smaller bias current, lowering the critical current of the SQUID in dependence on  $\Phi_L$ .

The total flux  $\Phi$  through the SQUID is the sum of the applied flux  $\Phi_L$  and the flux  $\Phi_s$  due to  $I_s$  and, as mentioned above, it has to satisfy

$$\Phi = \Phi_L + \Phi_s = n\Phi_0, \quad n \in \mathbb{Z} \quad (2.6)$$

due to the superconductivity of the SQUID. It is energetically favourable for  $\Phi_s$  to take the minimum possible absolute value, complementing  $\Phi_L$  to the closest integer multiple of  $\Phi_0$ . For this reason,  $\Phi_s$  shows a periodic sawtooth behaviour as a function of  $\Phi_L$ , taking increasingly negative values for  $\Phi_L \in [n\Phi_0, (n + \frac{1}{2})\Phi_0]$ , flipping sign at its minimum value of  $-\Phi_0/2$  and taking decreasing positive values for  $\Phi_L \in [(n + \frac{1}{2})\Phi_0, (n + 1)\Phi_0]$  before flipping sign again by going through 0 at  $\Phi_L = (n + 1)\Phi_0$  (see Figure 2.6a). The corresponding variation of  $I_s$  implies that  $I_c$  depends periodically on  $\Phi_L$ . This in turn entails a change of the voltage drop  $V$  across the SQUID, as its current-voltage

characteristic depends on  $I_c$ , with a lower critical current corresponding to a larger voltage drop (see Figure 2.6b). For a constant SQUID bias current  $I_b$ ,  $V$  therefore becomes a periodic function of  $\Phi_L$  with a period of  $\Phi_0$ , maxima for  $\Phi_L = (n + \frac{1}{2})\Phi_0$  and minima for  $\Phi_L = n\Phi_0$ , as shown in Figure 2.6c.  $V$  is fed into a feedback circuit that contains another coil, compensating any change in input flux. This flux locked loop eliminates the periodicity of the final output voltage, which is then linearly related to the input flux. However, if the input flux changes very rapidly, as is the case for fast-rising signal pulses, the feedback electronics may not react in time and the flux through the SQUID can change by one or several flux quanta before the regulation sets in, jumping to an equivalent point on the periodic  $V$ -vs- $\Phi_L$  curve (Figure 2.6c). Because the falling flanks of pulses are less steep than the rising edges, no equivalent jump takes place there and the new flux value is maintained after the pulse has passed, lowering the output voltage permanently. When several of these “flux quantum losses” (FQLs) occur during the course of one continuous detector operation and the output voltage becomes too low, the SQUID is reset to restore the initial configuration. The resulting experimental signatures are presented in Section 3.2.2, while Section 3.3.1 discusses how FQLs can be dealt with in the analysis. For more details on SQUIDs and their integration in CRESST, refer to [94, 105–107].

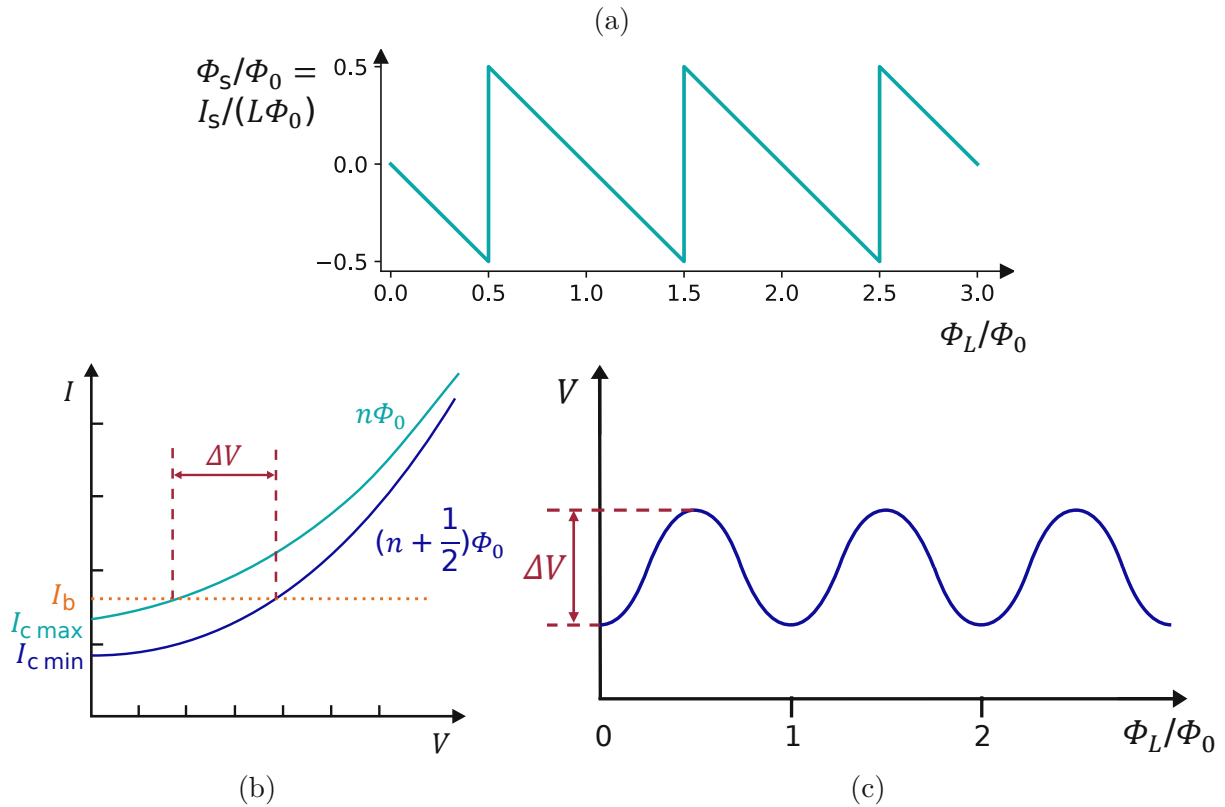


Figure 2.6.: (a) Screening flux, or equivalently screening current, in a DC SQUID, depending on the externally applied flux  $\Phi_L$ . (b) Current-voltage characteristic of a DC SQUID for different values of  $\Phi_L$ . Shown are the two extremal curves for a minimal/maximal critical current  $I_{c \min/\max}$ . Adapted from [105]. (c) Voltage drop over a DC SQUID as a function of  $\Phi_L$  for a constant bias current  $I_b$ . The dependency is oscillatory with a period of one flux quantum  $\Phi_0$ , and an amplitude  $\Delta V$  that is determined by the current-voltage characteristic and the choice of  $I_b$ . Adapted from [106].

## 2.2.5. Detector Operation and Data Acquisition

To maintain a stable detector temperature at the chosen WP, several measures are taken. Firstly, the cryostat needs to be refilled with liquid nitrogen and liquid helium about three times per week. The data taking is stopped for the refills, until stable conditions are reached again, causing gaps of several hours between the recorded data files, which typically cover around 50 h each. The rough operating temperature is given by the cryostat, but the fine tuning is achieved with the individual heaters on each detector. In addition to a constant heater current for temperature stabilisation, two classes of pulses are generated by a waveform generator (or pulser), sent through the heaters and read out by the detectors. *Control pulses* (CPs) are sent in regular intervals (usually 10 seconds) to probe the maximum pulse height by heating the TES beyond transition<sup>6</sup>. If the CP height indicates that the detector deviates from its WP, the heater DC is adjusted accordingly [99]. After every other CP, a *test pulse* (TP) is sent. TPs vary in amplitude and serve to establish the detector response. Specifically, they allow to correct for the nonlinearity of the TES transition, taking temporal temperature fluctuations around the WP into account. Sometimes, chosen at random, no TP is sent at the usual time, leaving instead an empty noise baseline for recording. The utilisation of both classes of heater pulses (CPs and TPs) in the analysis is more thoroughly addressed in Section 3.2.

Figure 2.7 illustrates the CRESST electronics, including the data acquisition (DAQ) and heater systems. The SQUID output voltage is passed through a filter, amplifier and shaper, before being used as input for the *hardware trigger*. When the signal surpasses a predefined trigger threshold, the output voltage is digitised and saved in an `.rdt` file for the time period of a *record window*. The sampling rate of the digitiser is 25 kHz, corresponding to a sample length of 40  $\mu$ s. For one hardware trigger record window,  $2^{14} = 16384$  samples, equivalent to 655.36 ms, are stored. The trigger time is placed at a quarter of the record window, thus also recording a portion of the pre-trigger region, which gives important information on the voltage baseline before the pulse. Aside from the hardware trigger, the raw stream of the SQUID output voltage is also digitised in its entirety and saved separately in a `.csmp1` file, using the same sampling rate of 25 kHz. Having the entire stream available allows to utilise optimised triggering algorithms with a *software trigger* (see Section 3.2.5). Moreover, arbitrarily long voltage traces can then be analysed by extending the record window.

For CPs and TPs, the time of the pulse injections are recorded, so that these artificial pulses can be tagged and discerned from event pulses. The injected TP amplitude (TPA) is additionally noted in V applied by the pulser for each TP. By use of a square rooter, the injected energy is linearly dependent on the TPA. The muon veto panels have their own DAQ with a trigger acting on the summed signal of all PMTs. In case of a veto trigger, the signals of each panel and the sum channel are digitised by a charge-to-digital converter (QDC) and stored in `.qdc` files, together with the trigger time. All timing information for the DAQ systems is provided by the same clock and timestamping unit, ensuring synchronicity.

---

<sup>6</sup>If the required heater DC for an optimal WP is very low, the heater settings may not allow the CPs to heat the TES into its fully normal conducting state, thus not representing the maximum pulse height. The stabilisation with CPs is still functional as long as a distinctly non-linear part of the TES transition curve is reached, causing deviations from the WP to affect the CP height.

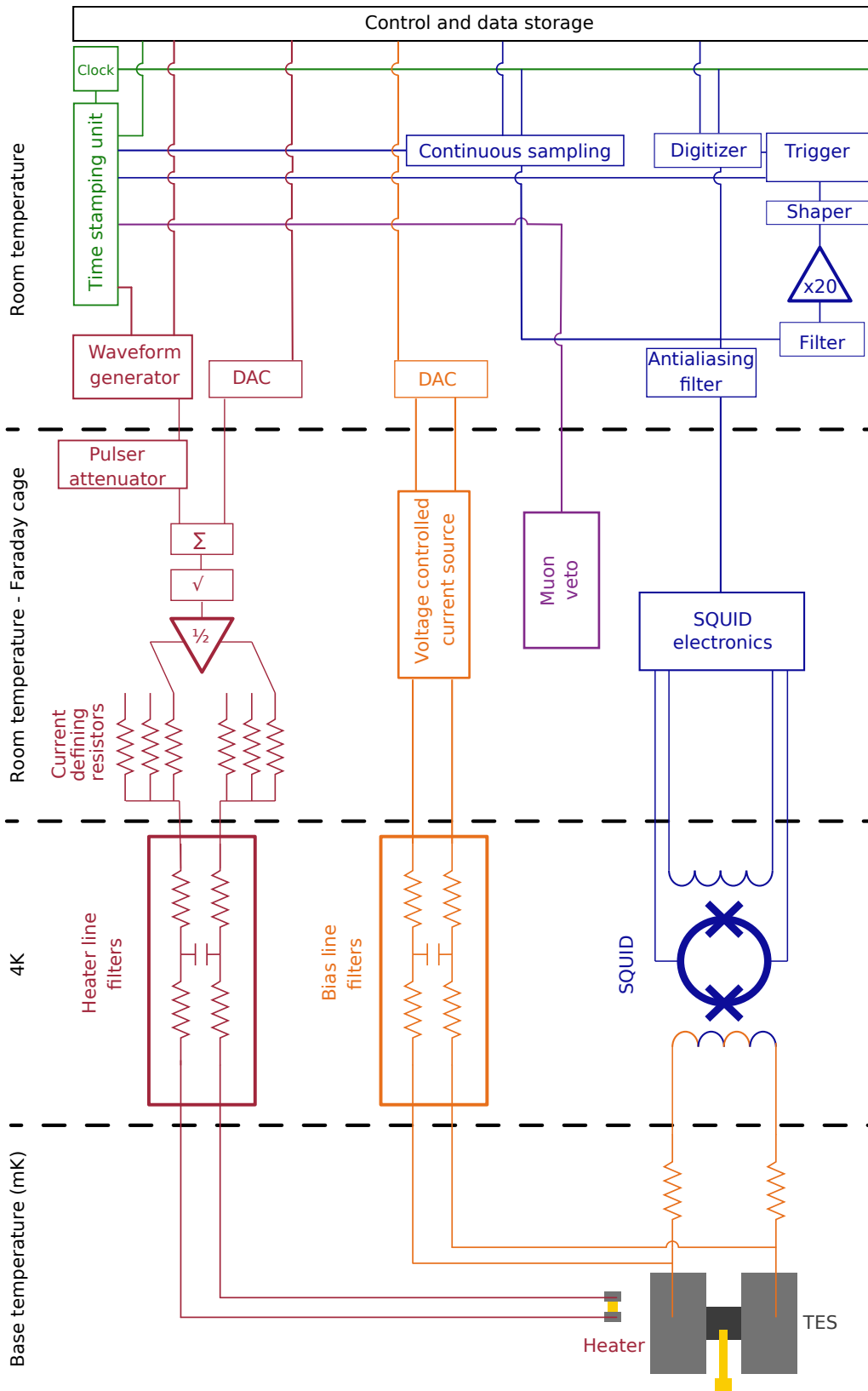


Figure 2.7.: Schematic of the CRESST electronics and DAQ. In green: timing system. Red: heater circuit. Orange: TES bias circuit. Purple: muon veto. Blue: SQUID electronics and detector DAQ. DAC stands for *digital-to-analogue converter*. Adapted from [108].

## 2.3. Background

Despite the various layers of passive and active shieldings (see Section 2.1.1), there are still several sources of background present. Naturally occurring radioactive nuclides contaminate each component of the setup, including the detector crystals and the shieldings. Great care is taken to produce the critical components with the highest possible radiopurity, but some residual radioactivity cannot be avoided. This section discusses the main mechanisms responsible for the background in CRESST detectors.

### 2.3.1. Natural Radioactivity

Radioactivity is the emission of radiation from an unstable nucleus. Through this process, nuclei can change their composition, transmuting into different nuclides, or release excitation energy. For a comprehensive introduction, refer to [109].

In  $\alpha$ -decays, the decaying parent nucleus  $X$  emits a  ${}^4\text{He}$  nucleus, also known as an  $\alpha$ -particle, thereby reducing its mass number  $A$  by 4 and its atomic number  $Z$  by 2:



where  $Y$  is the daughter nucleus resultant of this decay. The  ${}^4\text{He}$  nucleus has a high binding energy, making it an energetically favoured ejectile.  $\alpha$ -decay is most common in heavy elements, such as U, Th or Po. The kinetic energy of the emitted  $\alpha$ -particles is typically on the order of MeV. Due to their charge and relatively large mass,  $\alpha$ -particles are rapidly stopped by interactions with matter, depositing their entire kinetic energy in the process. Thus, the spectral signature of  $\alpha$ -decay is a peak of an energy that is unambiguously determined by the kinematics of the decay. The width of the peak is mostly due to the finite detector resolution, and its height follows from the number of occurred decays.

$\beta$ -decays happen when a neutron inside the initial nucleus  $X$  turns into a proton ( $\beta^-$ -decay), or vice versa ( $\beta^+$ -decay), under the emission of an electron  $e^-$  and an electron-antineutrino  $\bar{\nu}_e$  ( $\beta^-$ ), or a positron  $e^+$  and an electron-neutrino  $\nu_e$  ( $\beta^+$ ). The corresponding formula reads



Akin to  $\beta$ -decay is the process of electron capture, in which an atomic electron reacts with a proton in the nucleus to form a neutron, emitting an electron neutrino. The resulting nuclide is the same as after a  $\beta^+$ -decay of the parent.

By undergoing  $\beta$ -decay, a more stable ratio of protons to neutrons in the nucleus is reached. Being only slightly more penetrating than  $\alpha$ -particles, the  $\beta$ -particles ( $e^\pm$ ) are also quickly absorbed by matter, while the weakly interacting  $\nu_e/\bar{\nu}_e$  mostly escape completely. As a consequence,  $\beta$ -decay does not cause peaks in the energy spectrum, since the  $\nu_e/\bar{\nu}_e$  can carry away any fraction of the total decay energy, or  $Q$  value, which commonly goes up to a few MeV. Conversely, the kinetic energy of the emitted  $\beta$ -particle can also fall between 0 and the maximum defined by  $Q$ , resulting in a continuous contribution to the spectrum that ends at  $Q$ .

Following  $\alpha$ - and  $\beta$ -decays, the newly produced daughter nucleus is often in an excited

state. Relaxing to its ground state, it can emit a  $\gamma$ - or X-ray-photon, with energies ranging from  $\mathcal{O}(\text{keV})$  to  $\mathcal{O}(\text{MeV})$ . These photons do not interact as strongly as  $\alpha$ - or  $\beta$ -particles and are not necessarily stopped within the detector volume. The ones that are absorbed lead to a characteristic *photopeak* in the spectrum, while the rest causes less specific, more continuous background components.

### 2.3.2. Origin of Radionuclides

Created in astrophysical processes, primordial radionuclides are part of Earth since its formation. Of the species with sufficiently long half-lives, some amounts still remain today. The slow decay of these primary nuclides produces secondary nuclides. These are either stable or decay again, leading to a *decay chain*. Due to  $\alpha$ -decays being the only common decays that change the mass number (by 4), the nuclides of a chain have mass numbers in the same equivalence class modulo 4. Of the four resulting decay chains, three have primary nuclides (chain heads) with long enough lifetimes that the chains are still present in nature. These are the chains from  $^{238}\text{U}$  to  $^{206}\text{Pb}$ , from  $^{235}\text{U}$  to  $^{207}\text{Pb}$  and from  $^{232}\text{Th}$  to  $^{208}\text{Pb}$ , which are shown in Figure 2.8.

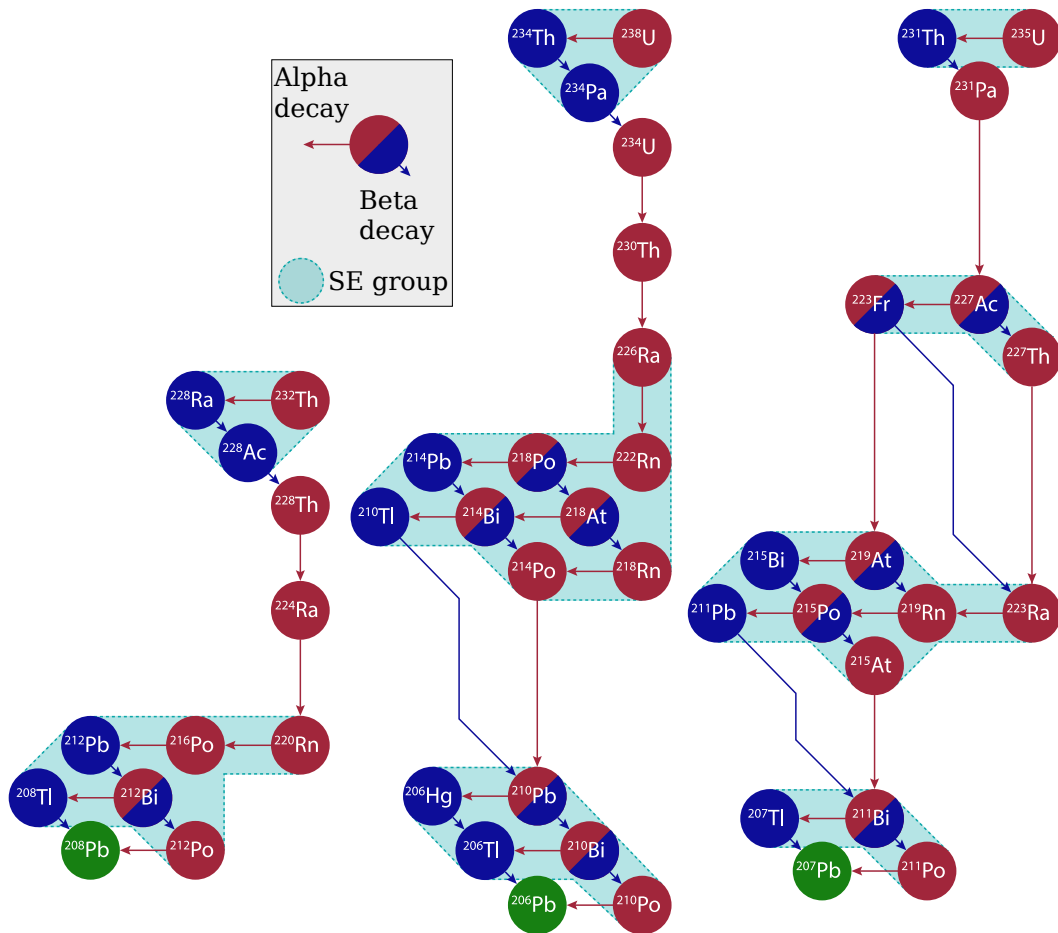


Figure 2.8.: The three natural decay chains, starting with (from left to right)  $^{232}\text{Th}$ ,  $^{238}\text{U}$  and  $^{235}\text{U}$  and all ending in a stable isotope of Pb. Highlighted in teal are secular equilibrium groups that were found to be adhered to in the  $\text{CaWO}_4$  crystal of the “TUM40” detector, which was operated in CRESST-II. Adapted from [110].

The abundances of the nuclides in a chain are related to each other, as their half-lives and decay branching ratios are fixed. In particular, a daughter nuclide that decays much faster than its parent nuclide will decay at the same rate at which it is produced, causing the decay activities of both parent and daughter to be equivalent. This scenario is called *secular equilibrium* (SE) [109]. There can even be larger groups of nuclides related by it, as long as the parent’s half-life is sufficiently long in comparison to all other half-lives of the SE group. Equilibrium conditions are helpful for the assessment of spectral background components, as they can link prominent  $\alpha$ -peaks to the less conspicuous contributions of  $\beta$ - or  $\gamma$ -decays. However, SE can be broken, when the natural abundances of nuclides are changed during processing or purification, either by preferential removal of some members of an SE group, or by inadvertent introduction of additional contaminations. To radionuclides that are not part of a decay chain, such as  $^{40}\text{K}$ , no SE relations can be applied.

All primordial radionuclides and their active decay products constitute the *radiogenic* background component. A different source of natural radionuclides is *cosmogenic activation*. In this process, a highly energetic cosmic ray or a product thereof, like an atmospheric neutron, interacts with a nucleus to create one or several new nuclides, which are (partly) radioactive. To minimise cosmogenic activation of experimental components, the purified copper used for structures and shieldings, as well as the detector crystals, were stored underground before their installation in CRESST [99, 111].

Radioactive contaminations of the target crystals themselves make up the “internal” background sources. Radionuclides in all other parts, like the carousel and the shieldings, are collectively referred to as “external” background sources.

### 2.3.3. Low Energy Excess

In recent years, a background component that is not well understood has been observed at the lowest energies accessible to the CRESST detectors. This *low energy excess* (LEE) shows an exponential rise of events for decreasing energies and currently limits the sensitivity of CRESST to low-mass DM. It is also present in other DM direct search experiments, where it causes similar problems [112]. In an effort to study the LEE and mitigate its impact, novel CRESST detector designs have been developed and are operated in the current “Run37” data taking campaign. Among them are, for instance, modules with two identical TESs on the same absorber crystal [113].

### 2.3.4. Background Simulations and Modelling

For the purpose of identifying the main background contributions, simulations are performed and compared to the signals observed in the detectors. Due to challenges in simulating the LEE, it is not yet included in the models. The simulations are carried out with the *ImpCRESST* [114] tool, which is based on the particle-matter-interaction simulation software *Geant4*. Here, the geometry of the detector setup is modelled and decays along with propagations and energy depositions of the decay products are simulated. This procedure is performed one by one for each considered radionuclide in the internal and several external parts, creating a *spectral template* for each background component. Such a template is thus a simulated energy spectrum resulting from a specific radionuclide in a specific location, taking into account all the complex interactions and energy loss mechanisms that can occur.

Granted that the simulations model the physical system with sufficient accuracy, it should be possible to reproduce a good approximation to the complete observed energy spectrum by scaling the simulated templates by their respective activities and adding them up. In the present case, the activities are to be determined by performing a *Bayesian maximum likelihood fit* of the simulated templates to the measured data. Within this framework, which is detailed in [115, 116], a likelihood function  $\mathcal{L}$  is constructed, describing how probable it is to obtain the observed spectrum for a given choice of activities. The experimental spectrum is in the form of a histogram with  $n_{\text{bin}}$  bins and  $n_j$  entries in the  $j$ -th bin. From the simulations,  $v_j(\vec{A})$  is the expected number of hits in bin  $j$ , depending on the activities of each template that are contained in the parameter vector  $\vec{A}$ . The  $k$ -th component  $A_k$  of  $\vec{A}$  is the activity of the  $k$ -th background component. If SE between two or several background components is assumed, the associated templates can be treated together with one common activity. The probability  $P(n_j)$  to observe  $n_j$  counts in the  $j$ -th bin, given an expected value of  $v_j(\vec{A})$ , follows a Poisson distribution:

$$P(n_j) = \frac{v_j(\vec{A})^{n_j} e^{-v_j(\vec{A})}}{n_j!}. \quad (2.9)$$

The likelihood function for the fit can then be formulated as a product of Poissonians, one per bin:

$$\mathcal{L}(\vec{A}) = \prod_{j=1}^{n_{\text{bin}}} \frac{v_j(\vec{A})^{n_j} e^{-v_j(\vec{A})}}{n_j!}. \quad (2.10)$$

An estimate for the activities that maximises  $\mathcal{L}$  can be found with a *simulated annealing* algorithm. In short, simulated annealing samples the high-dimensional parameter space of possible activities, converging to a point of maximum likelihood. The results of the fit can provide an explanation for the observed spectrum, which is especially interesting for spectral features that cannot easily be ascribed to any one impurity prior to the fit. The attained activity estimates can be used to assess the amounts of contaminations in the crystals and other components of the experimental hardware. This identification of the main impurities provides valuable input for the development of future production and purification procedures.

# 3. CRESST DATA ANALYSIS

The aim of this chapter is to describe how the raw data produced by CRESST is processed and analysed. The standard CRESST analysis concepts and routines are introduced. Building on this, more specialised procedures that are intended for the analysis of highly energetic events in Run36 detectors, with energy depositions larger than some tens of keVs, are discussed and refined. In this regime, the standard analysis methods fail, making the utilisation of alternative techniques necessary.

## 3.1. Types of Recorded Data

This section briefly reviews the two kinds of detector data recorded by CRESST, mentioned already in Section 2.2.5.

### 3.1.1. Hardware-Triggered Data

As a first step in the analysis of a detector module's data, the hardware-triggered data is considered. It consists of voltage traces with a fixed record length of  $2^{14}$  samples, as described in Section 2.2.5. One `.rdt` file usually spans the time between two cryostat refills, containing the data that was recorded by all readout channels in this interval. Among the recorded data are particle events, TPs, and empty baselines for noise analysis (from when a TP was intentionally left out). One example of each of these is shown in Figure 3.1, recorded by the phonon detector of the module TUM93A, which is referred to as *TUM93A-Ph*.

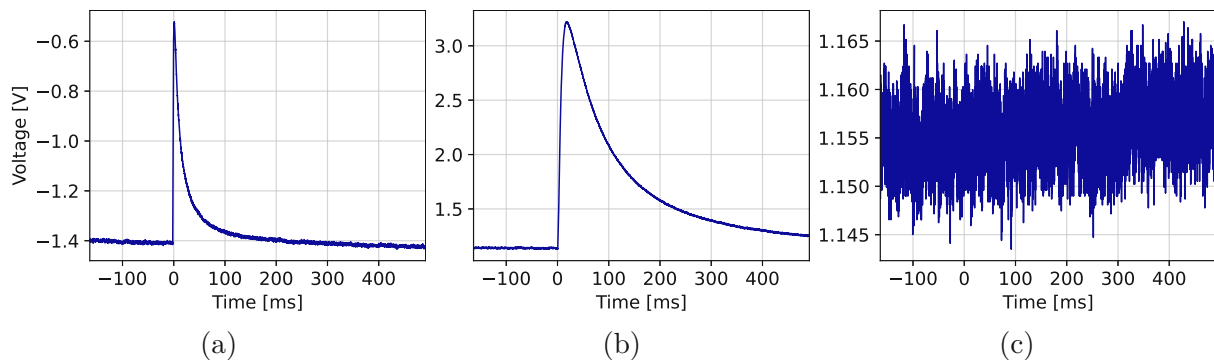


Figure 3.1.: Voltage traces from the hardware-triggered data of TUM93A-Ph. Shown are (a) a particle event, (b) a TP, and (c) an empty baseline consisting of noise. Time is measured starting from a quarter of the record window, where the trigger was set off.

The hardware-triggered data provides a quick first look at the quality of the data being recorded and thus is used to monitor the detector output during data taking campaigns.

Moreover, the hardware-triggered data is used to extract information for the triggering of the continuous stream, as explained below.

### 3.1.2. Continuously Recorded Data

Without any prior triggering, the SQUID output voltage of each channel is recorded in a `.csmp1` file as a continuous stream, covering the same duration as the corresponding `.rdt` file. The stream is a full recording of one detector's signal, with no losses of potentially relevant information due to suboptimal trigger settings, thus allowing for a full exploitation of the data recorded by the experiment. Specifically, filters that enhance the signal-to-noise ratio can be applied to the stream before or after triggering on it (see Sections 3.2.5 and 3.2.6). Different trigger thresholds can be selected depending on the analysis objective, with the lowest achievable threshold being desired for DM search analyses, but slightly higher thresholds proving advantageous for some background analyses. Moreover, the duration of voltage traces extracted from the stream is not limited by a fixed record window length. A portion of the stream from TUM93A-Ph is shown in Figure 3.2. The stream contains CPs, TPs and pulses from particle interactions in the crystal. The CPs and TPs can be identified in the stream by their separately recorded timestamps and are used for active stabilization and calibration of the detector, respectively. An optimum filter trigger (see Section 3.2.5) finds particle pulses from the stream.

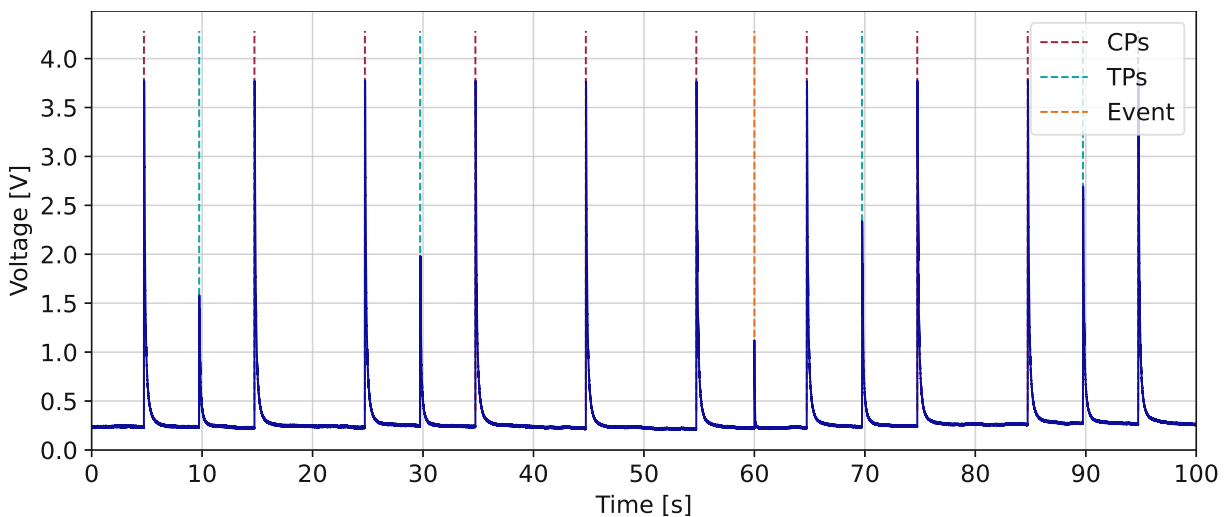


Figure 3.2.: A section of 100 s of the voltage stream from TUM93A-Ph, containing CPs in intervals of 10 s, TPs, and one event. The TPs are sent after every other CP, unless when one TP is left out to record an empty baseline with the hardware trigger DAQ, as is the case around 50 s.

## 3.2. Standard Analysis Methods

### 3.2.1. Fundamental Analysis Parameters

There are various parameters describing different aspects of the pulse shape, or other properties of a voltage trace, that are routinely used for the analysis. A selection of some parameters that are particularly relevant for the present work is listed and briefly

explained in Table 3.1. Before the parameter calculation, the voltage trace is smoothed by applying a moving average of 50 samples length. Moreover, the baseline voltage is shifted to zero by computing the mean voltage of the first eighth of the record window and subtracting it from the entire voltage trace.

Parameter	Description
<b>ph</b> – pulse height	Maximum voltage value within the record window. Used as a proxy for the event energy, where calibration has to be performed for accurate results.
<b>mt</b> – maximum time	Time of the maximum sample.
<b>on</b> – onset	Time of the last sample before the <b>mt</b> that subceeds 20 % of the <b>ph</b> .
<b>rt</b> – rise time	Time of the last sample before the <b>mt</b> that subceeds 80 % of the <b>ph</b> .
<b>dt</b> – decay time	Time it takes for the pulse to fall from 90 % of the <b>ph</b> to $\frac{1}{e} \approx 37\%$ of the <b>ph</b> .
<b>md</b> – minimum derivative	The minimum value of the event array’s numerical derivative (difference of consecutive samples).
<b>bd</b> – baseline difference	Difference of the baseline voltage after and before the pulse. Calculated as the difference between the averages of either the last and first 500 samples or the last and first eighth of the voltage trace.

Table 3.1.: Frequently used analysis parameters. All listed values are calculated after taking a 50-sample moving average of and subtracting the baseline from the voltage trace. Absolute time values are measured starting from one quarter of the record window.

### 3.2.2. Special Event Types and Artefacts

In addition to heater pulses and relatively low energy events (such as those shown in Figures 3.1a and 3.2), other conspicuous features may appear on the stream, the most common of which are addressed in the following and depicted in Figure 3.3.

Highly energetic events can heat the TES enough to leave the linear part of its transition curve, causing an irregular shape of the event pulse (Figure 3.3a). Depending on the amount of heating beyond the linear range, the manifestation of this effect can go from a slight rounding of the top part of the pulse to an outright truncation of the pulse at the maximum voltage level - the *saturation voltage*  $V_{\text{sat}}$ . The saturation voltage is equal to the sum of baseline voltage and maximum **ph**. As long as the maximum **ph** is not reached, the **ph** can still be used to determine the energy, as is discussed in Section 3.2.6. However, for energy depositions high enough to heat the TES to its normal conducting state, the **ph** is always at its maximum and independent of the energy. These saturated events plateau at the top as long as the TES remains fully normal conducting. In this case, a different method has to be used to extract the event’s energy from the voltage trace, as is described at length in section 3.3.

Pulses associated with a large energy deposition typically rise more quickly than their lower-energy counterparts. The fastest rising pulses can cause FQLs (see Section 2.2.4), leading to a drop in the baseline voltage compared to the baseline before the pulse (see

Figure 3.3b). Because the jump in flux occurs during the rapidly rising edge of the pulse, FQLs lower the  $\text{ph}$  by a value corresponding to one or several flux quanta. Consequently, the actual magnitude of these pulses is incorrectly underestimated when only considering their  $\text{ph}$ s.

After several FQLs, the SQUID is reset, entailing a rapid rise of the signal voltage by an amount much greater than the maximum  $\text{ph}$  (Figure 3.3c). SQUID resets that are triggered as events can therefore be identified by their impossibly large apparent  $\text{ph}$ s.

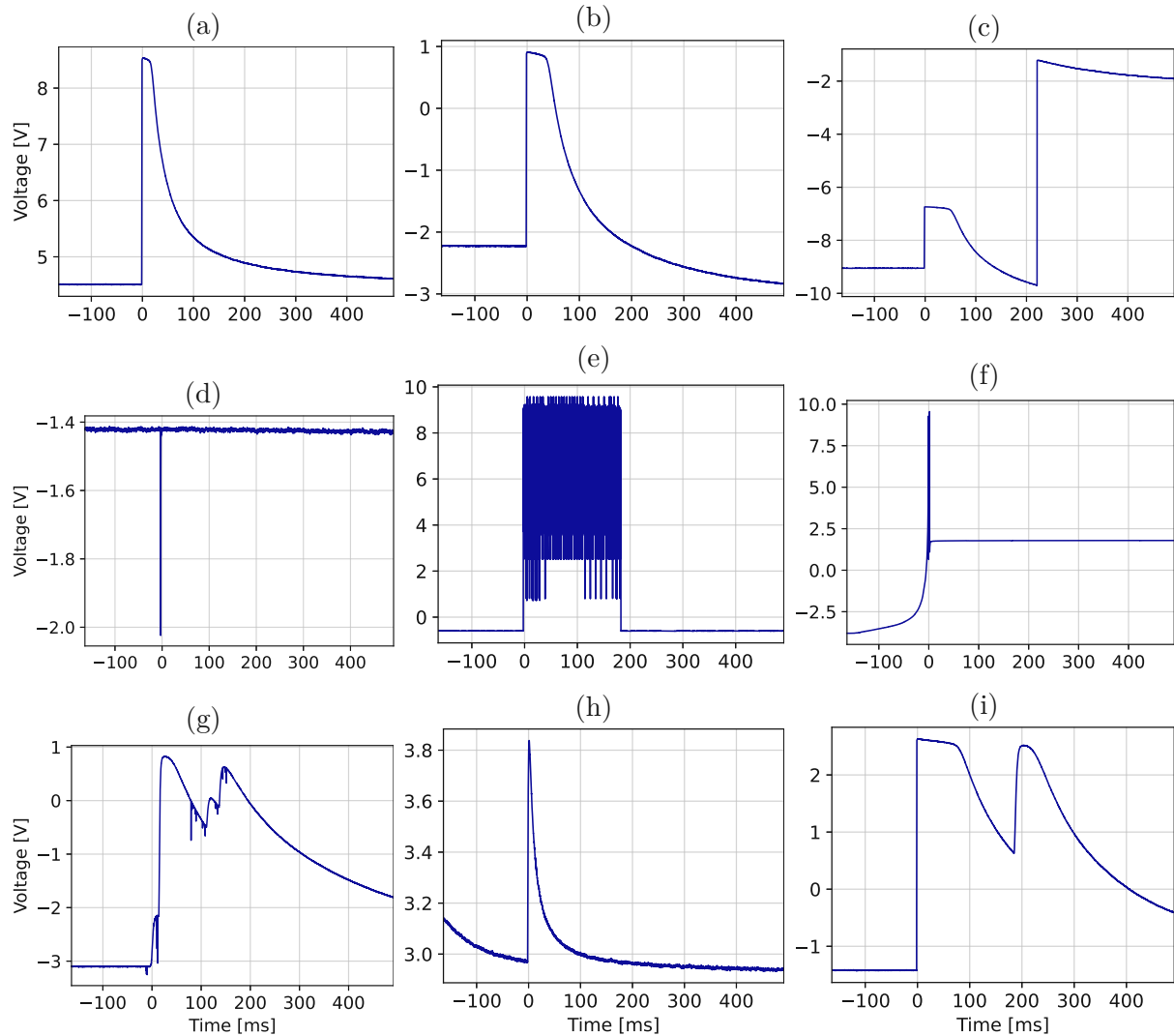


Figure 3.3.: Extraordinary events and artefacts. (a) Saturated event. (b) Saturated event with FQL. (c) Saturated event with FQL and subsequent SQUID reset at around 220 ms. (d) Delta spike. (e), (f), (g) Miscellaneous electronic artefacts. (h) Decaying baseline due to pileup in the pre-trigger region. (i) Pileup after the triggered event pulse. All samples shown stem from TUM93A-Ph.

Apart from effects of the TES and SQUID operation, other electronic artefacts are also present on the stream. “Delta spikes” (Figure 3.3d) are negative voltage spikes of only one to a few samples length (hence the name) and are presumably created by the DAQ electronics [117]. An origin from a regular detector signal can be ruled out for them, due to their negative deviations from the baseline voltage and their extremely short durations.

Moreover, delta spikes typically occur in all readout channels with a virtually identical appearance, indifferent of the detector specifics, making their electronic origin even more clear. Because of the specifics of the trigger algorithm (see Section 3.2.5), delta spikes can be triggered as events, but they can be recognised by their low *md*.

Furthermore, there are some rarer electronic artefacts, like the ones shown in Figures 3.3e, 3.3f and 3.3g. Artefacts like those in Figures 3.3e and 3.3f appear only in one channel, but are again easily excluded from the analysis by their *ph* or *md*, or a combination of these. The last shown artefact class, of which Figure 3.3g displays a sample, resembles a pileup of several pulses with superimposed delta spikes. The delta spike are again present in all channels, while the further appearance differs between the channels.

Another special case arises from the pileup of several pulses, when a pulse sets in before the previous one has completely decayed. This phenomenon can take various specific forms, depending on the relative timing of the involved pulses and their characteristics. Especially common are pileups between events and CPs or TPs. Pileups between several events are rare because of the low event rate, and pileups between CPs and TPs themselves are impossible by design. When an event pulse sits on the falling flank of a CP or TP, a seemingly decaying baseline can often be observed within the bounds of the record window (Figure 3.3h). In some cases, decaying baselines can even cause a trigger without an event pulse. If the concerned heater pulse starts after the event pulse, it is more straightforward to recognise the pileup as such (Figure 3.3i). The latter case is in practice only observed for large event pulses, as the largest pulse in a given record window is usually the one that is triggered, so that the heater pulse is triggered for smaller events (see also Section 3.2.5).

### 3.2.3. Event Selection

For the sake of data selection, different cuts are applied to remove unwanted pulses from the analysis. In the code, cuts are realised as conditions, where only events that fulfil the cut conditions are considered further. Stricter cuts result in a higher confidence of their success, and thus in the data quality, but they might also wrongly exclude more valid events. Consequently, optimising the particular choice of cuts for a given analysis task is often highly involved. To correct for the number of wrongly removed events, the *cut efficiency* or *survival probability* can be determined. For this, artificial events are placed on the empty baselines of the hardware-triggered data, or directly on the stream. These simulated events are then triggered and the same cuts are applied to them as for the real events. The fraction of artificial events that remain in the dataset after the cuts defines the survival probability.

#### Stability Cut

Regardless of the pulse shape, events from periods with unstable detector conditions are removed by the *stability cut*, which concerns the CP height that is recorded for each CP. In unstable periods, where the TES temperature deviates from the WP, the CP height changes accordingly. CPs are defined as unstable if their heights deviate more than a certain number (e.g. 3) of statistical standard deviations (SDs) from the mean height of all CPs in the considered dataset. Any event recorded between two unstable CPs is flagged by the stability cut.

## Rate Cut

As DM and radioactive backgrounds are expected to cause approximately constant event rates, a *rate cut* on the recorded event rate may be employed to remove periods with higher than usual rates. The excess of events can be due to electronic or mechanical disturbances, such as external vibrations, which cause artefacts that are triggered as events. For the rate cut, the number of events within a given period is grouped into 10 min long bins. Bins where the event count deviates by more than a chosen number of SDs from the mean are then discarded.

## Muon Veto Coincidence Cut

Another cut that is standardly applied concerns the muon veto (see also Sections 2.1.1 and 2.2.5) and serves to exclude events that could be caused by muons, or secondary particles produced by muon interactions in the materials surrounding the detectors. All events starting within a chosen time interval (commonly  $\pm 2$  ms or  $\pm 5$  ms) around a muon veto trigger are discarded.

## Cuts on Pulse Parameters

Other cuts aim to exclude artefacts from the collection of events. As hinted at in Section 3.2.2, cuts on the *md* are able to discard delta spikes and other electronic artefacts with fast changing voltage values.

The *bd* is important for many cuts. Completely regular events should have a *bd* close to zero, subject only to noise fluctuations. Events with an FQL return to a lower voltage after the pulse and can therefore be selected or removed by their *bd*. Decaying baselines that are triggered result in a negative *bd* as well. Within a record window length of  $2^{14}$  samples, highly saturated pulses do not decay completely, with some even staying in saturation until after the end of the record window. Consequently, the *bd* is positive for these events, indicating that a longer record window has to be used to analyse these pulse and find a more meaningful value of the *bd*. Pileups can also lead to a positive *bd*. The highest values of the *bd* are reached by SQUID resets, making it possible to discard them using this criterium, or by a cut on the *ph*.

Furthermore, cuts can be applied to ensure specific pulse properties, such as an *on* that falls in a given range to remove miss-triggered events. When constructing a standard event (see Section 3.2.4), only pulses with similar shapes are to be selected, warranting extensive cuts on various pulse parameters.

### 3.2.4. Standard Event, Noise Power Spectrum and Optimum Filter

A typical event pulse is required for several analysis procedures, including the survival probability simulation discussed in Section 3.2.3, the creation of an optimum filter for triggering (see below), or the reconstruction of pulse height with a template fit (TF), discussed in Sections 3.2.6 and 3.3.3. In order to obtain such a *pulse template*, the arithmetic mean of a number of carefully chosen events is computed and normalised to have a maximum value of 1. The result is used as a *standard event* (SEV), shown in Figure 3.5a. Before averaging, the baselines are removed from the pulses, in the same way as for the calculation of analysis parameters (see Section 3.2.1).

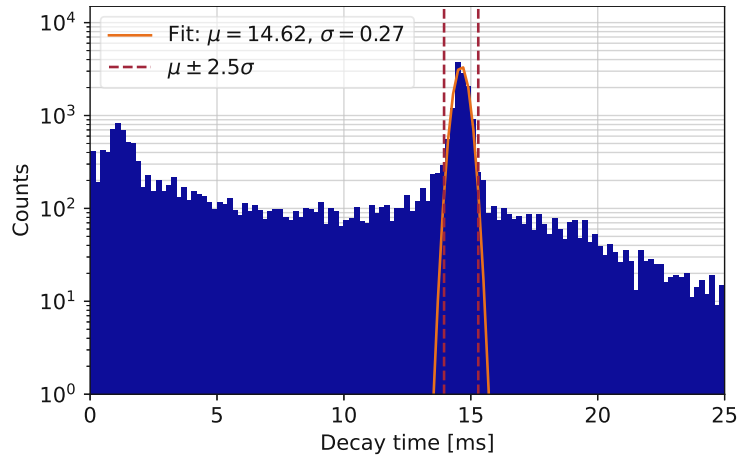


Figure 3.4.: Cut on the  $dt$  of events from the “bck” dataset of TUM93A-Ph, used to create an SEV. Events within a symmetrical interval extending 2.5 fit SDs  $\sigma$  on either side of the fit mean  $\mu$  are accepted.

The SEV captures the shape of an event pulse, while irregularities and noise are largely removed by the averaging. The more events are used to calculate the SEV, the better the noise suppression and confidence in the SEV’s validity. However, all included pulses must be as similar as possible in shape for the SEV to resemble a true particle event. Moreover, great care must be taken to exclude any artefacts, including pileups, from the averaged voltage traces. In the detectors discussed in this work, the  $^{55}\text{Fe}$  source provides an accumulation of events with similar shapes that can be utilised. To this end, several cuts on parameters such as the  $ph$ ,  $on$ ,  $rt$ ,  $dt$  and  $bd$  are defined. This can be done by plotting a histogram of the respective parameter, and selecting a region with a large number of events. The exact cut-off values can be defined by fitting a Gaussian to the selected peak and excluding all events that deviate further than a few SDs from the mean, introducing minimal human bias. An exemplary cut is visualised in Figure 3.4. To create an even cleaner SEV, the first version of the template can be fit to all pulses used in its creation, following the template fit procedure laid out in Section 3.2.6. If the concerned voltage trace contains a pileup, other artefacts, or a greatly different pulse shape, the root mean square (RMS) fit error (a measure for the goodness of fit) will be higher than for a typical pulse. Discarding events with a high fit RMS and subsequently recalculating the SEV results in an improved template.

As a counterpart to the SEV, which describes a typical pulse, a *noise power spectrum* (NPS), as depicted in Figure 3.5b, can be constructed, characterising the noise conditions of the detector. For this purpose, the empty baselines recorded by the hardware trigger DAQ are used. To remove any event pulses from the dataset, the same set of standard parameters as for events are computed, and baselines with a  $ph$  significantly above 0 are discarded. Moreover, the empty baselines are fitted with a 3<sup>rd</sup> degree polynomial, excluding the ones with an exceptionally high fit RMS. Additional cuts can again be applied to eliminate artefacts like delta spikes. Processing the thus cleaned baselines further, the discrete Fourier transform of each of them is calculated, decomposing the noise into its frequency spectrum. The power spectrum of one baseline is then given as the absolute square of the frequency spectrum, and the total NPS is found by taking the arithmetic mean of the individual power spectra for all selected baselines.

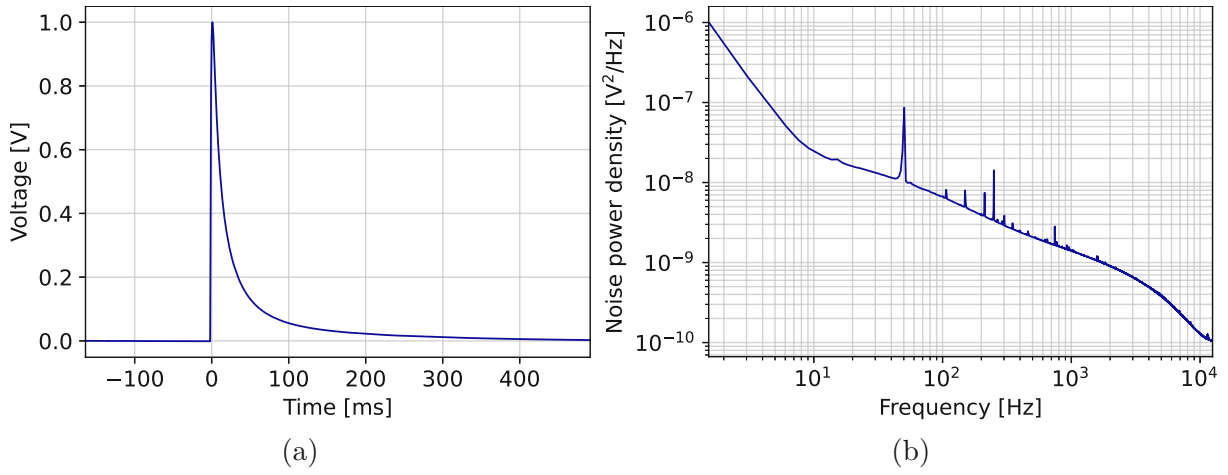


Figure 3.5.: (a) SEV created for the “bck” dataset of TUM93A-Ph. Compared to a typical event (Figure 3.1a), noise contributions are strongly suppressed. (b) NPS created for the “bck” dataset of TUM93A-Ph, with some distinct peaks and an overall decay towards higher frequencies.

The observed detector noise can stem from any component of the setup, or from external influences. A prominent peak in the NPS (Figure 3.5b) is located at 50 Hz, the electric grid frequency. Higher harmonics of this noise source are also visible on the spectrum, as well as some other small peaks. Aside from the peaks, the present NPS decays towards higher frequencies, largely following an approximately exponential behaviour, with an exponent around  $-0.6$  times the frequency (determined by fitting with an exponential curve).

Utilising the information contained in the SEV and NPS, the signal-to-noise ratio of the recorded data can be maximally enhanced by filtering it with a so-called *optimum filter* (OF). Following [118], the OF transfer function  $H(\omega)$ , depending on the frequency  $\omega$ , is calculated as

$$H(\omega) = K \frac{\hat{s}^*(\omega)}{N(\omega)} e^{-i\omega\tau_M}, \quad (3.1)$$

with the complex conjugate  $\hat{s}^*(\omega)$  of the Fourier-transformed SEV, the NPS  $N(\omega)$ , the time (sample index)  $\tau_M$  where the SEV  $s(t)$  reaches its maximum value, and a normalisation constant  $K$ . To apply the OF to a voltage trace, the trace is Fourier transformed to the frequency domain, multiplied by  $H(\omega)$  and subsequently backtransformed to the time domain.  $K$  is chosen so that the filtered SEV has a maximum value of 1. The OF created from the SEV and NPS of Figure 3.5 is shown in Figure 3.6, alongside an event that it was applied to. Evidently, the high-frequent noise is successfully suppressed by the filtering, and the filtered pulse is symmetric around its maximum. The strong suppression of 50 Hz noise leads to oscillations of the same frequency in the filtered pulse.

### 3.2.5. Stream Triggering and Threshold

The OF described above is an effective tool for triggering continuously recorded data. By enhancing the signal-to-noise ratio, it allows for a lower energy threshold for event detection. The OF is continuously applied on the whole stream, and the triggered event traces thus obtained are recorded in a file for further analysis. The algorithm triggers

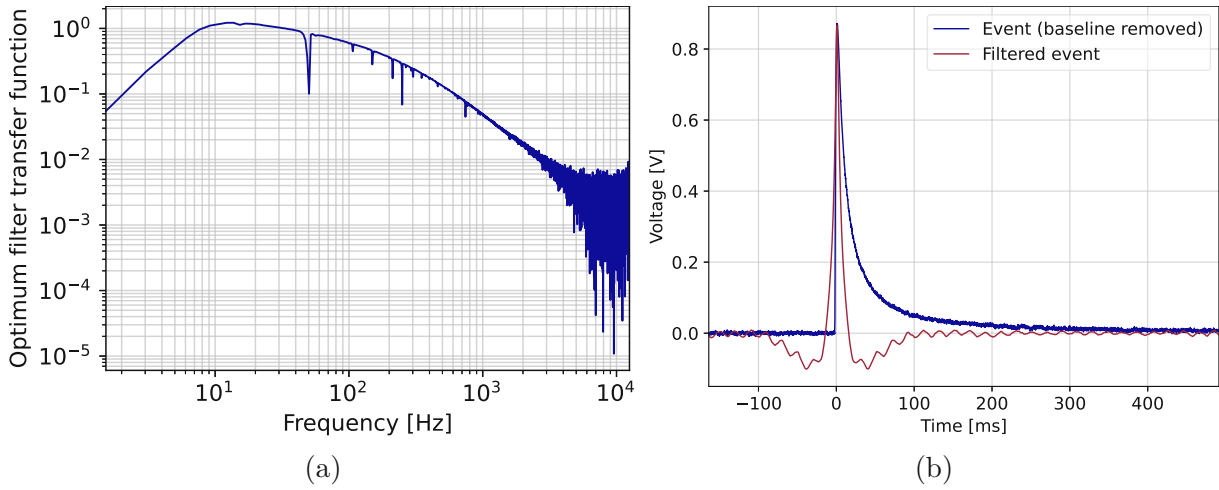


Figure 3.6.: (a) OF created for the “bck” dataset of TUM93A-Ph. (b) An event before and after optimum filtering. The baseline was removed by subtracting the mean of the first eighth of the record window.

when a sample of the filtered stream surpasses the predefined threshold. The trigger is then blocked for a specified length of time, called *trigger dead time*, to avoid triggering again on the same pulse. Within the interval defined by the dead time, the maximum sample is taken as the position of the triggered pulse. This *OF trigger* is standardly used for the extraction of events from the stream data, and more details on it can be found e.g. in [108]. As a possible alternative, a *z-score trigger* may be used, triggering when a sample deviates from the mean baseline voltage further than a set number of SDs. In either case, heater pulses are identified by their timestamps, which are read from a separate file, and marked as such, while all other triggers are attributed to events. Through the (mainly 50 Hz) oscillations of the filtered stream (see Figure 3.6b), per se negative delta spikes can still be triggered as events. Decaying baselines may similarly cause a pronounced signal after filtering, necessitating a sufficient trigger dead time or careful cuts in the analysis.

To define the threshold for the OF trigger, the empty baselines already used in the creation of the NPS (see Section 3.2.4), with the same cuts applied to exclude events and artefacts, are processed with the OF. The maximum voltage sample  $V_{\max}$  of each filtered record window is found and, following [119], their distribution is fitted with a function

$$P_d(V_{\max}) = \frac{d}{\sqrt{2\pi}\sigma} e^{-\left(\frac{V_{\max}}{\sqrt{2}\sigma}\right)^2} \left( \frac{1}{2} + \frac{\text{erf}\left(V_{\max}/(\sqrt{2}\sigma)\right)}{2} \right)^{d-1}, \quad (3.2)$$

using a maximum likelihood fit. Here,  $P_d(V_{\max})$  is the probability distribution of finding a maximum filtered voltage  $V_{\max}$  in a record window of  $d$  samples length, assuming a Gaussian distribution of filtered noise samples, whereas erf denotes the Gaussian error function<sup>7</sup>. For a threshold (filtered) voltage  $V_{\text{th}}$ , the expected rate of noise triggers  $R_{\text{NT}}(V_{\text{th}})$ , that is noise record windows with a maximum sample above  $V_{\text{th}}$ , is given by

$$R_{\text{NT}}(V_{\text{th}}) = \frac{1}{t_{\text{win}}} \int_{V_{\text{th}}}^{\infty} P_d(V_{\max}) dV_{\max}, \quad (3.3)$$

<sup>7</sup> $\text{erf}(x) = \frac{2}{\sqrt{\pi}} \int_0^x e^{-t^2} dt$

with the time of the record window  $t_{\text{win}} = d \cdot 40 \mu\text{s}$ . The threshold is now chosen to at most result in a set number (commonly 1) of noise triggers per  $\text{kg d}^8$  of detector exposure. For this,  $R_{\text{NT}}(V_{\text{th}})$  is divided by the detector mass  $m_{\text{det}}$  and set to the desired value, yielding  $V_{\text{th}}$ . An example of such a fit and the resulting threshold is shown in Figure 3.7. For some detectors, like “TUM93A-L”, the light detector of the TUM93A module, where the LEE significantly pollutes the noise baselines, a more complicated model is chosen to describe both the Gaussian noise and the additional exponential pollution [120].

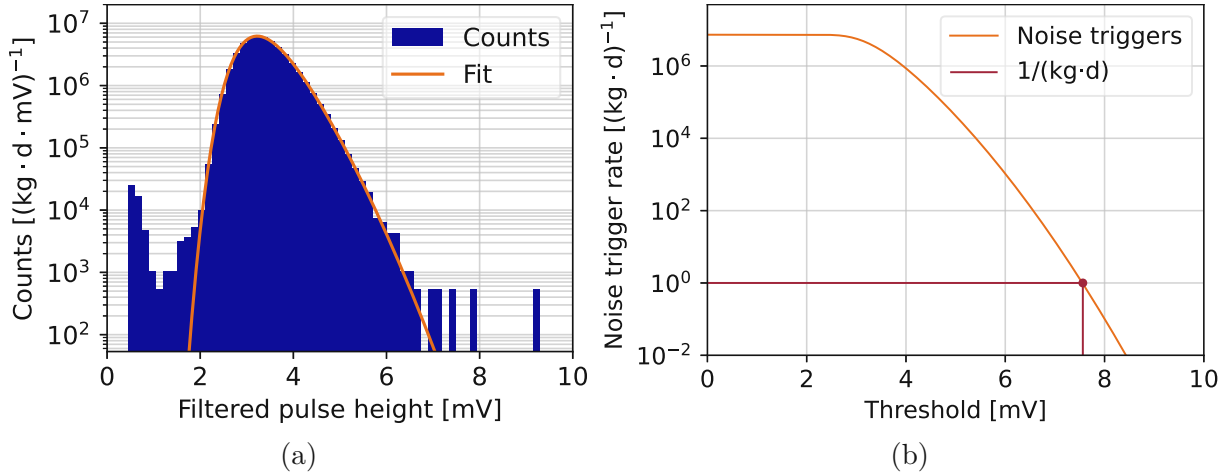


Figure 3.7.: (a) Histogram of filtered pulse heights of noise traces, as given by the maximum sample after filtering, fitted with a Gaussian noise model (eq. 3.2). The data is taken from the “bck” dataset of TUM93A-Ph. (b) Determination of the OF trigger threshold for 1 noise trigger per  $\text{kg d}$  of detector exposure, following eq. 3.3. The threshold for this choice is determined to be 7.563 mV.

### 3.2.6. Energy Reconstruction

After triggering on the continuous stream, a new and refined dataset of events is available for the analysis. All common analysis parameters are computed and cuts can be applied. Usually, the main aim is to obtain an energy spectrum of the analysed detector. For the calculation of DM limits, the most relevant range is that of low energies, while background analyses can benefit from knowledge about all energy ranges in which events occur.

In the relatively low-energy region, where the maximum  $\text{ph}$  is not reached, some standard techniques are routinely employed to determine the deposited energy of a given event pulse. In the simplest approach, the  $\text{ph}$  can be used as a proxy for energy. Especially for very low energies, though, this parameter is susceptible to noise fluctuations and it is beneficial to refine the procedure. One option is to fit the SEV to each pulse, scaling it by a factor, shifting it in time and fitting the baseline with a polynomial (often a constant). The scaling factor of this *template fit* (TF) is called  $\text{tfph}$  (TF pulse height) and is more robust with regard to fluctuations than the regular  $\text{ph}$ . The quality of the fit can be assessed via the fit RMS, as mentioned in Section 3.2.4. If the pulse is given by  $p(t)$  and

<sup>8</sup>The unit used here for exposure is kilograms (of detector mass) times days (of detector operation). Lighter detectors offer less target for interactions of DM (or other) particles, thus they have to operate longer for the same exposure.

the fitted function by  $f(t)$ , depending on the sample index (discrete time variable)  $t$ , the RMS is calculated as  $\text{RMS} = \sqrt{\frac{1}{N} \sum_t (p(t) - f(t))^2}$ , for  $N$  considered samples. Another alternative is offered by the OF, which is also used for triggering. The maximum voltage value of the filtered pulse defines the **ofph** (OF pulse height), which benefits from the noise suppression through the OF, resulting in a better resolution that is especially advantageous at the lowest energies.

Whichever of the above approaches is chosen, in a next step, the TPs are used to correct for the non-linearity of the TES response and for drifts in the detector response. The latter are caused by temperature fluctuations around the WP that happen in spite of the stabilisation with CPs. For the calibration, the **ph** (or a variant thereof) is calculated for all TPs and plotted over time. For each injected TPA, a band of reconstructed **phs** is visible, with a finite width due to fluctuations and the resolution of detector and analysis. A piecewise linear function or spline is fit to each band, appending pieces for each period of stable detector operation, resulting in a single line that models the reconstructed TP **ph** depending on time (see Figure 3.8a). Using these interpolations for all TPAs, a time-dependent transfer function is found, mapping the reconstructed **ph** to an equivalent TPA (Figure 3.8b). As the injected energy depends linearly on the TPA, converting the event **phs** to equivalent TPAs removes the non-linearity stemming from the TES transition curve, up until the point where the TES goes into saturation.

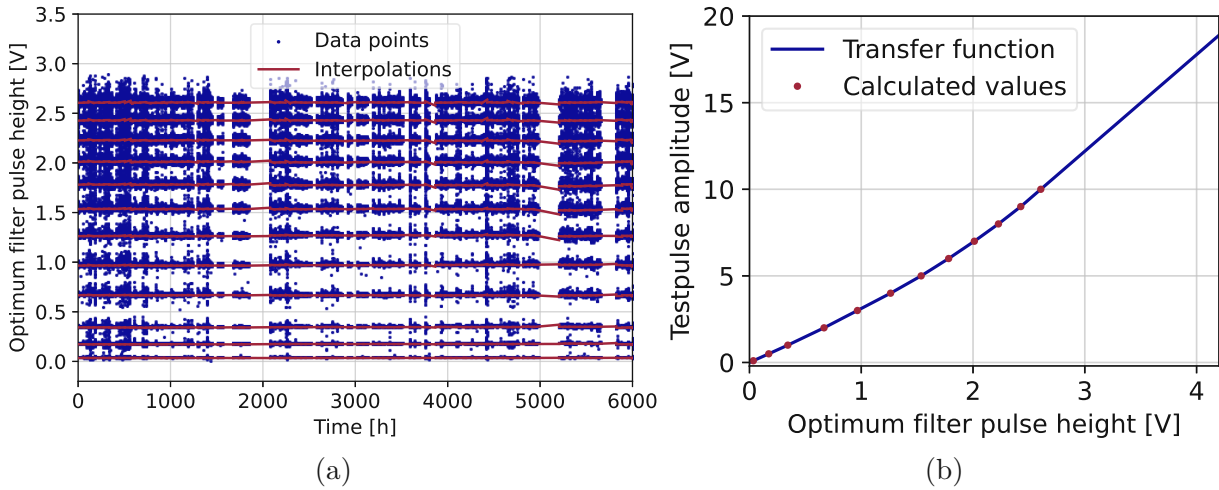


Figure 3.8.: (a) Linear interpolations of the reconstructed **ofph** for TPs in the “bck” dataset of TUM93A-Ph, one for each TPA. (b) Transfer function for one chosen point in time. For each TPA, the corresponding **ofph** is calculated using the interpolations from (a).

Finally, to convert the TPA equivalents to energy deposited in the detector by recoil events, a calibration source is needed. In the present case, a radioactive  $^{55}\text{Fe}$  source, which emits characteristic K- $\alpha$  and K- $\beta$  X-rays corresponding to energies of  $E_{\text{K-}\alpha} = 5.9 \text{ keV}$  and  $E_{\text{K-}\beta} = 6.5 \text{ keV}$  respectively, is used for the calibration. The more prominent K- $\alpha$  peak is identified in the TPA equivalent spectrum and fitted with a Gaussian, the mean of which is  $\mu_{\text{K-}\alpha}$ . Thereafter, the conversion factor  $C$  from TPA equivalent to energy is found as  $C = E_{\text{K-}\alpha} / \mu_{\text{K-}\alpha}$ . The K- $\beta$  line can similarly be used to refine the estimate.

### 3.3. Extension of the Accessible Energy Range

As described in Section 2.2.1, the detector modules operated during the Run36 data taking campaign mostly employ a  $20 \times 20 \times 10 \text{ mm}^3$  absorber crystal, which is smaller than in previous CRESST detectors. The lower resulting thermal mass and heat capacity improve the energy threshold for DM searches. However, they pose problems for the analysis of more energetic events, such as the ones caused by many background sources, because the corresponding pulses are often saturated. For completely saturated pulses, the **ph** does not further increase with the deposited energy and thus cannot be used for energy reconstruction. Even though the OF trigger still correctly triggers saturated pulses, the **ofph** is also no longer a reliable measure for energy. In contrast, the TF can be adjusted to be applicable to these pulses, providing one method to extend the available energy range with the *truncated template fit* (TTF). Another approach to address the issue at hand is the *saturation time analysis* (STA), which is especially well-suited for the application to pulses of the highest observed energies, stemming mainly from  $\alpha$ -decays.

As another consequence of the small detector masses, FQLs are a common occurrence in the high-energy region, necessitating a correction before the actual pulse analysis. Since pulses of higher energies are larger, a record window longer than  $2^{14}$  samples is needed to fully accommodate them and therefore, continuously recorded data has to be used. Another aspect to consider is that of pileups, mainly with heater pulses, which become increasingly likely for the long record windows used. If ignored, they can lead to a faulty energy reconstruction. Therefore, measures mitigating the impact of pileups are implemented.

#### 3.3.1. Flux Quantum Loss Correction

The signature of an FQL is that of a clearly saturated pulse that does nevertheless not reach the maximum **ph**, followed by a decay to a lower baseline than before the pulse. Naively, the **bd** could be used to estimate the voltage drop associated with an FQL, proceeding separately for each affected pulse. However, pileups both before and after the considered pulse can influence the **bd**, therefore motivating the utilisation of a more sophisticated technique, which is called “minimum-minimum difference” (MMD). For this method, the minimum values of the voltage trace before and after the pulse are found. To reduce the influence of noise, averages over 500 samples are taken from intervals 600 to 100 samples before the minima. Excluding the actual minimum values from the averages additionally serves noise mitigation, as the minima are likely to sit at negative outliers. Not averaging symmetrically around the minima, but only before them, prevents the inclusion of a pulse setting in after the minimum (this could be the main pulse for the first minimum or a pileup for the second one). Pulses before the minima do not have as large an influence, as the decaying flank is much less steep than the rising edge of a pulse. The two obtained averages are used as best estimates for the baseline voltages after and before the pulse, and their difference, the **mmd**, is then a more reliable estimate of the baseline difference. In an alternative attempt to estimate the FQL-induced voltage drop, the latter is calculated as the difference between the maximum **ph**, which is assumed to be known, and the **ph** of the concerned pulse. Since fluctuations around the WP entail changes of the maximum **ph**, this method was found to be less precise and not further pursued.

An even better accuracy and precision of the FQL correction (FQLC) are achieved by considering the periodic SQUID response (Figure 2.6c), due to which the voltage drop  $V_{\Phi_0}$  corresponding to the loss of a single FQ  $\Phi_0$  is always the same. The `mmd` is calculated for all triggered events and plotted in a histogram, featuring several peaks at negative values, depending on the number of flux quanta lost, as shown in Figure 3.9a.  $V_{\Phi_0}$  is found as a value close to the lower end of the first peak, because incomplete pulse decays and pileups systematically increase the mean value. Pileups in the pre-trigger region can lower the `mmd`, but this effect is less pronounced. In the actual FQLC, any pulse with a `mmd` below a certain threshold is corrected by an integer multiple of  $V_{\Phi_0}$ , rounding up the number of FQ lost. By this procedure, even exceedingly long pulses and the ones worst affected by pileups should be corrected with the appropriate voltage.

The FQLC is applied as a positive shift to the voltage trace starting at the `on`, where the change of flux through the SQUID takes place. For this to be as precise as possible, the `on` is recalculated without prior smoothing, since the standardly calculated `on` precedes the true start of the pulse due to the smoothing. As a result, a step artefact would be created by the FQLC shift, causing problems in the further analysis, especially for the TTF. An event before and after FQLC is shown in Figure 3.9b.

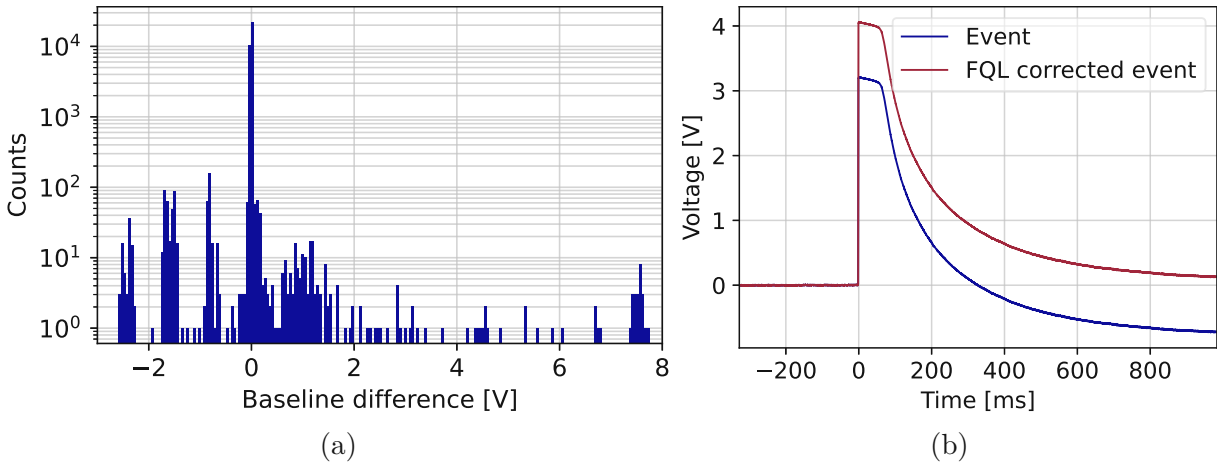


Figure 3.9.: (a) Histogram of baseline differences calculated with the MMD approach and a record window length of  $2^{17} = 131072$  samples for the “bck” dataset of TUM93A-Ph. At negative voltages, the peaks are due to FQLs, while the accumulation at low positive values is the result of pileups. The highest values are caused by SQUID resets. The equivalent voltage of a FQ was found to be  $V_{\Phi_0} \approx 0.85$  V. (b) FQLC applied to an affected event, using the value of  $V_{\Phi_0}$  determined in (a).

### 3.3.2. Saturation Time Analysis

In contrast to all other presented methods for event energy reconstruction, the STA, which was developed in [99], examines not the (reconstructed) height, but rather the width of a pulse. While the TES resistance does not vary significantly once saturation is reached, the duration for which the TES is fully normal conducting does increase with the deposited energy. Resultingly, the time that the pulse spends at the saturation voltage can be used as a proxy for the energy. The saturation time `st` can be defined as the time that the

pulse voltage, after baseline subtraction, is greater than a chosen percentage of the  $ph$ . The exact choice of which value to use is not overly important, as more energetic pulses remain longer above any given threshold. Setting the criterium to 90% of the  $ph$  has proven to be a solid choice, as this puts the end point of the  $st$  interval on a steep part of the falling pulse flank, reducing the effects of noise, while also being high enough to keep the probability of pileups during the concerned time interval low. Computationally, the  $st$  is found by starting at the  $mt$  of the pulse and calculating the duration of the interval between the first samples in either direction that fall below 90% of the  $ph$ . For this, the  $mt$  is only searched in a certain interval around the expected peak position of the event pulse to avoid targeting large pileup pulses. The start point of the  $st$  interval, sitting on the steep rising edge, is calculated without smoothing, while moving-average smoothing with a length of 10 samples is applied before calculating the end point on the falling flank, suppressing the noise contributions there. For the calculation to proceed without error, a correct subtraction of the pre-pulse baseline is necessary. As a consequence of the longer record window used for the analysis of large pulses, pileups in the pre-trigger region become more likely, because the window is also extended before the pulse, so that the pulse always starts at a fourth of the window. In order to lessen the impact of pre-trigger pileups on the baseline removal, the baseline voltage is computed following the approach used for the MMD (see Section 3.3.1). Figure 3.10 shows the STA in action.

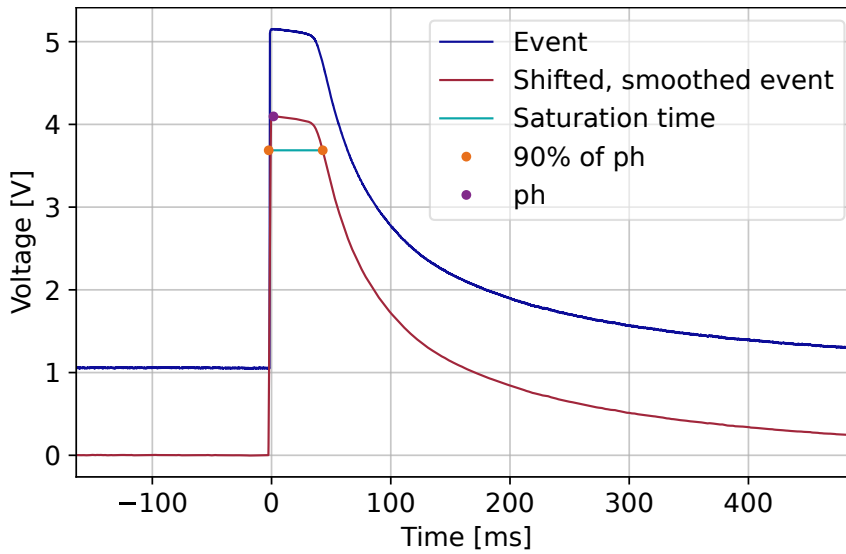


Figure 3.10.: Visualisation of the STA applied to an exemplary event of the “bck” dataset of TUM93A-Ph.

Applying the STA to all saturated pulses of a given dataset results in an  $st$  spectrum. To convert it to an energy spectrum, discernible lines from background radioactivity, typically  $\alpha$ -lines, are used for calibration. Simplifying the pulse shape model discussed in [121], the decaying flank of a pulse, with the baseline subtracted, is modelled by an exponential function

$$V(t) = V_0 \cdot e^{-(t-t_0)/\tau}, \quad (3.4)$$

which is assumed to be valid only below the saturation level. If there was no saturation, the pulse would have an original amplitude of  $V_0$ , starting decay at  $t = t_0$  with a time constant  $\tau$ . Defining  $t_{sat}$  as the time that the pulse spends above a certain level, e.g.

$0.9V_{\text{sat}}$ , allows to establish a relation between  $t_{\text{sat}}$  and  $V_0$ :

$$V(t_{\text{sat}}) = 0.9V_{\text{sat}} = V_0 \cdot e^{-(t_{\text{sat}}-t_0)/\tau} \rightarrow V_0 = 0.9V_{\text{sat}} \cdot e^{(t_{\text{sat}}-t_0)/\tau}. \quad (3.5)$$

Assuming a linear relationship between the deposited energy  $E$  and  $V_0$ , the conversion from  $t_{\text{sat}}$  to  $E$  should approximately follow

$$E = a \cdot e^{b(t_{\text{sat}}-c)} + d, \quad (3.6)$$

with parameters  $a$ ,  $b$ ,  $c$  and  $d$  that are to be determined by a least-squares fit to the identified lines. The parameter  $d$  is empirical and often necessary for a good fit, showing that the simplified pulse shape model is not totally valid. The exponential behaviour is nevertheless well-motivated and in good agreement with the data. No calibration with TPs is done for the STA, as the TPs are limited to much lower amplitudes than relevant. In any case, a small fluctuation of the WP should not have a significant impact on the reconstructed energy of the very large considered pulses.

### 3.3.3. Truncated Template Fit

The TTF builds on the TF described in Section 3.2.6, again fitting an SEV template to the pulse in question, as shown in Figure 3.11. In order to reliably fit large pulses, whose shape deviates from the scaled-up template in the top part due to saturation, the fit is only performed to the lower part of the pulse. The cut-off voltage level (after baseline subtraction)  $V_{\text{trunc}}$ , called *truncation voltage* or *truncation level*, has to be predefined for each detector and dataset. Ignoring all voltage samples above this level allows to accurately fit templates scaled to many multiples of the original (maximum) pulse height with a relatively low fit RMS. The  $\text{tfph}$ , the scaling factor of the template, is then assumed to be unaffected by the effects of saturation, if the truncation level is chosen adequately. One way to find a reasonable truncation voltage is to perform a regular TF on pulses of all available  $\text{ph}$ s and determine at which  $\text{ph}$  the quality of the fit starts to decline. In a plot of TF RMS over  $\text{ph}$  or  $\text{tfph}$ , the RMS can be seen to rise for higher pulses, indicating a change in pulse shape.  $V_{\text{trunc}}$  should be chosen at or below the point where a strong increase in RMS sets in.

As for the regular TF, a clean SEV is needed for the fitting procedure. The added requirement of sufficient length to fit large pulses makes cleaning measures to exclude pileups and other irregularities even more important. Additional measures can be taken to remove remainders of decaying baselines that may be present after averaging.

Before performing the TTF, an FQLC is applied to affected pulses. In contrast to the STA, pileups in the pre-trigger region are not of great concern for the TTF, since a wrong baseline removal would only result in a shift of the template, not influencing the scaling or fit quality strongly. In contrast, pileups after the analysed pulse, to which the STA is relatively indifferent, stand to cause an over-scaling of the template along with a high fit RMS. Avoiding this, each voltage trace is examined for secondary peaks with a z-score trigger, limiting the fit range to the time before the first pileup pulse starts. Alternatively, the timestamps generated by the initial triggering could have been used for this purpose, but this approach was not implemented due to difficulties of its integration into the software.

To improve the TTF's accuracy, it can be beneficial to re-fit pulses that are assigned a high  $\text{tfph}$  (clearly above the maximum  $\text{ph}$ ) with a higher  $V_{\text{trunc}}$ . Still, fits with a large RMS should be rejected. Defining a maximum permissible RMS value is a trade-off between the amount of attained data and the confidence in the accuracy and precision thereof. As the RMS rises with the  $\text{tfph}$ , RMS cut values depending on the  $\text{tfph}$  can be sensible.

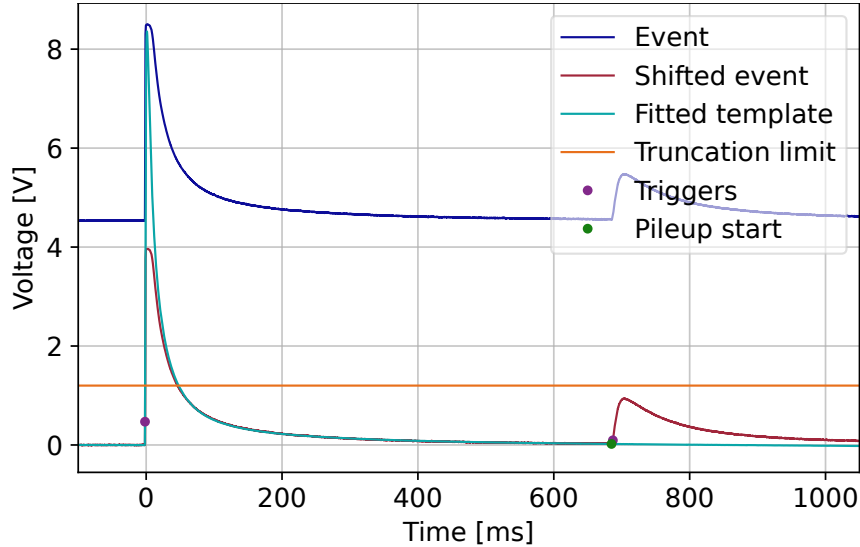


Figure 3.11.: TTF applied to an exemplary event of the “bck” dataset of TUM93A-Ph. All samples above the truncation limit and after the pileup start are disregarded for the fit.

The necessary effort to create an appropriate template and define a truncation level makes the TTF less convenient in application, as compared to the STA. In general, the STA also offers superior resolution at very high energies, but the TTF is capable of producing a continuous spectrum from the lowest to the highest energies, bridging the gap between standard methods and the STA.

For energy calibration, the iron peaks provide a handle in the low energy region, and the  $\alpha$ -lines are used at high energies. Because the resolution of the TTF might be too degraded to discern individual  $\alpha$ -peaks, the STA can aid by tagging the events pertaining to each peak. An empirically motivated polynomial calibration curve can then be fitted to the acquired data points. Again, no TP calibration is performed, but non-linearities of the TES response are mitigated by the truncated fit, which is designed to only consider the linear parts of the analysed pulses. Fluctuations around the WP can nevertheless cause a reduced resolution that might be notable at low energies.

# 4. RESULTS OF THE ANALYSIS

In this chapter, the reconstruction of energy depositions from the measured pulses in several Run36 modules is described, utilising the techniques established in the previous chapter. The reconstructed energies span from sub-keV detector thresholds to several MeVs, extending to the previously inaccessible high-energy range. In principle, both the phonon and light channels can be analysed, allowing to distinguish different event classes, such as  $\alpha$ -events,  $e^-$ - and  $\gamma$ -events, and nuclear recoils. However, the goal of the present analysis is to provide data for a likelihood fit of simulated templates. The latter are so far only available for the phonon detectors, which are referred to by the module name with a suffix “-Ph”. As a consequence, the light channels are mostly disregarded in the performed analyses.

In the first step, datasets for the analysis are selected. Results for the modules “TUM93A”, “TUM93C”, “Comm1” and “Comm2” are presented here. The former two were manufactured at the Technical University of Munich and cut from the same crystal (called “TUM93”), while the latter two employ commercially produced crystals. All four modules use  $\text{CaWO}_4$  crystals of 24 g weight as main absorbers and 0.6 g SOS wafers as light detectors. The “Comm” modules utilise bronze clamps for the crystal holding and have no scintillating foil coating, while the “TUM” modules hold their detectors mostly with copper sticks, with TUM93A having one i-stick. As the same analysis methods are applied to all modules, they are only described in detail for the first discussed module, TUM93A. Throughout, the *Python* package *cait* (Cryogenic Artificial Intelligence Tools) [122], developed specifically for the analysis of cryogenic DM experimental data, is used.

## 4.1. Datasets

There are various datasets available, pertaining to separate periods of Run36, as depicted in Figure 4.1. The data inspected for DM and background analyses stems from the background data taking periods, that make up the bulk of the runtime. The first background dataset is referred to as “bck”, for background. In order to study the LEE, which, aside from DM search, is a main experimental goal of Run36, several warm-ups (WUs) of the detectors to different temperatures were performed. During these times, data taking is paused and the detectors are held at the WU temperature for a certain duration, before being cooled down again. This does not only have an effect on the LEE rate, which is increased by the WUs and decays thereafter, but can also affect the general detector conditions. After the WUs, more background data is taken. The longest such dataset, “awu” (after warm-up) follows on a WU to 60 K and is interrupted by some short WUs to relatively low temperatures (see Figure 4.1). Data from after WUs to higher temperatures is contained in datasets separately labelled as “awu 11 K” and “awu 130 K”. Additionally, calibrations with a  $^{57}\text{Co}$ -source and a neutron source were carried out and the corresponding data is placed in the “cal” and “ncal” sets, respectively. Associated data from before or after the calibration periods is referred to as “pre-cal” or “post-cal” data.

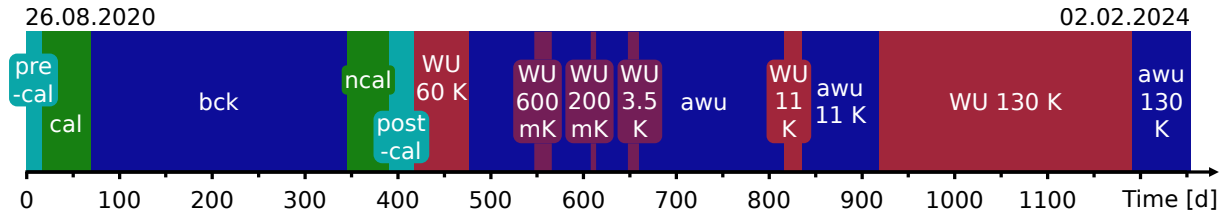


Figure 4.1.: Timeline of Run36 with the different datasets and their names. Calibration periods are in green, associated time ranges before and after the actual calibration in teal, background data taking intervals in blue and WU periods in red. During the WUs, no data is taken.

In any general analysis, it is desirable to include all background files from the entire data-taking campaign to have maximum statistics. However, there can be periods when the detector operation faced severe problems that must be excluded from the analysis. Using a CRESST-internal log, some of the most problematic files can be excluded a priori, while other faults or instabilities may become apparent only during the examination of the recorded data, and the file list is refined over the course of the analysis. The appendix A contains the final lists of files used for the analyses presented below. Due to differences in the detector response between the datasets, all analyses are done separately for the bck and awu data.

## 4.2. TUM93A

The analysis steps leading to the creation of high-energy spectra are shown in this section, using the example of TUM93A-Ph. A preliminary fit of simulated templates to the spectra is also presented.

### 4.2.1. Hardware Triggered Data and Software Triggering

Following the procedures described in Chapter 3, an SEV, NPS and OF are created from the hardware-triggered data, separately for the bck and awu datasets. For the creation of the SEV, cuts on the *on*, *bd*, *rt*, *ph*, *dt* and *md* are applied to select only pulses of similar shapes (stemming from  $^{55}\text{Fe}$  K- $\alpha$  events) and to discard artefacts. Before calculating the NPS, noise baselines with pulses, irregularities and artefacts are removed based on their *ph*, 3<sup>rd</sup>-degree-polynomial-fit-RMS and *bd*. The cuts are carried out in the order given here, with only the surviving fraction being used to determine the limits for the next cut, facilitating the choice of meaningful parameter intervals. Additionally cutting on the light channel parameters makes the selections more stringent. The trigger threshold determined via the OF is used only as a lower limit. A higher threshold is chosen, cutting off the part of the spectrum dominated by the LEE, which is not modelled in the simulations. This has the benefit of triggering significantly less events, which speeds up all subsequent procedures. Moreover, a higher threshold allows to reduce the time interval around heater pulses, within which triggers are always counted as heater pulses, as the 50 Hz oscillations around heater pulses caused by the optimum filtering can be erroneously triggered for the lower threshold, but not for the higher one. The threshold of the phonon channel for the

stream triggering is thus chosen at 20 mV for both the bck and awu datasets. The light detector and i-stick are not used for triggering.

## 4.2.2. Energy Reconstruction Methods

An SEV of  $2^{16}$  samples length is created for the TTF, largely using the same cuts as for the hardware-triggered SEV. For a cleaner result, the preliminary SEV is used to exclude irregular pulses and artefacts, as described in Section 3.2.4. An example for a voltage trace discarded by this cut is shown alongside the final SEV in Figure 4.2. Even after careful cuts, decaying baselines in the pre-trigger region are present in some of the selected voltage traces and a baseline correction is applied to remove their effect from the final SEV. The improvements in SEV quality achieved by these procedures are relatively small, but crucial when performing a TTF to large pulses, where the SEV is scaled up by factors up to over 1000 and only the lowest parts are considered for the fit.

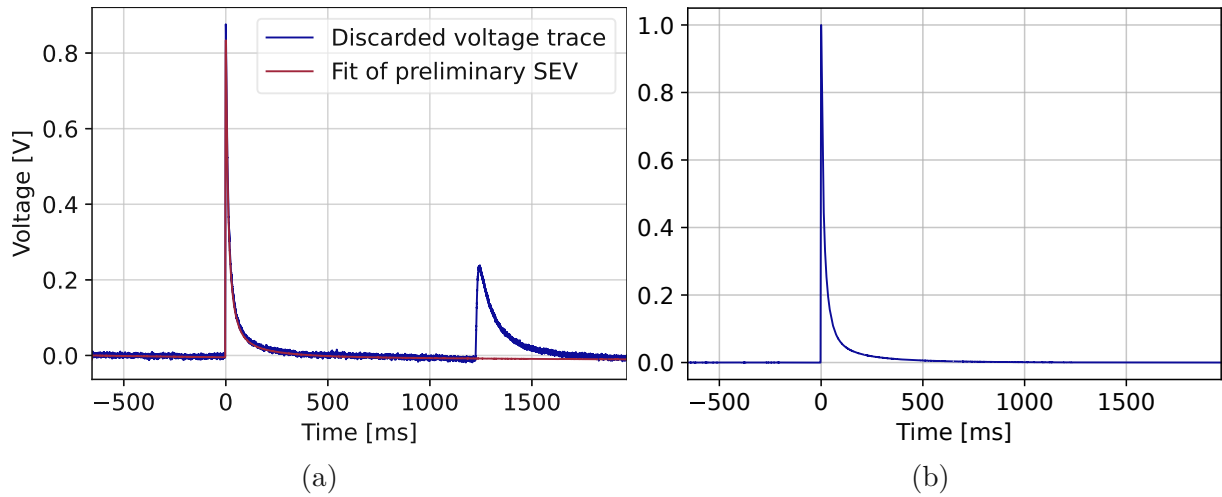


Figure 4.2.: (a) Voltage trace containing a pileup, fitted with the preliminary SEV. It is discarded by a cut on the fit RMS, after passing all other cuts. (b) Long SEV used for the TTF of TUM93A-Ph in the bck dataset. As opposed to the preliminary SEV in (a), the baseline does not fall below 0 owing to the baseline correction.

From voltage traces of  $2^{17}$  samples length,  $V_{\Phi_0}$  is determined, as shown in Section 3.3.1. A value of  $V_{\Phi_0} = 0.85$  V to 0.87 V is found for both datasets of all analysed channels, also in the other modules studied, demonstrating the uniformity of the different SQUID circuits. The threshold voltage drop for the FQLC is chosen as  $-\frac{1}{3}V_{\Phi_0}$ , meaning that any event with a `mm` below  $-(n + \frac{1}{3}) \cdot V_{\Phi_0}$  is corrected by  $n \cdot V_{\Phi_0}$ .

Utilising a record length of  $2^{16}$  samples for the TTF and  $2^{18}$  samples for the STA, both methods are applied to the event pulses. Before calibrating the resulting `st` and `tfph` spectra to energies, some data quality cuts are undertaken. These include a cut on the `ph` to exclude SQUID resets, on the `md` to remove delta spikes and on the `on`, discarding miss-triggered pulses and other artefacts. Furthermore, a rate cut and a muon veto cut are used. For the latter, all events triggered within a 10 ms coincidence window centred on the muon veto triggers are excluded. No CP stability cut is employed as the largest investigated

pulses can cause a wrong reconstruction of the CP  $ph$ , resulting in unstable time intervals around these events. For the STA, an additional cut removes pulses with very low  $ph$ s that are certainly not saturated (even considering multiple FQLs) and consequently not eligible for the STA. This is important to avoid faulty reconstructions by the STA that could otherwise occur for very small pulses or artefacts, resulting in an erroneously high reconstructed energy. The precise cut values used for all modules, including TUM93A, are summarised in Table 4.1.

Module	TUM93A		TUM93C		Comm1		Comm2	
Dataset	bck	awu	bck	awu	bck	awu	bck	awu
Rate	3 SDs around the mean rate							
Muon veto coincidence	$\pm 5$ ms							
Maximal $ph$ [V] – SQUID resets	5	4.7	2.9	2.55	3.1	3	3	2.8
Minimal $md$ [mV/sample] – delta spikes	-7.4	-7	-3	-2.4	-4	-4.5	-2.8	-3.1
on [ms]	[-4,-2]	[-3.4,-2.7]	[-4,-2]	[-4,-3.5]	[-5,-3]	[-4.6,-4.2]	[-5,-3]	[-4.6,-4.2]
Minimal $ph$ [V] for STA	0.1		0.02		0.02		0.06	

Table 4.1.: Cut values used in the analysis.

### 4.2.3. Calibration

For the energy calibration, it can be necessary to subdivide the bck and awu datasets into separate *calibration intervals*, if the detector conditions vary significantly between these periods. To define the intervals, the  $st$ ,  $tfph$ ,  $ph$  and TP  $ph$  are plotted over time, showing the evolution of the detector response (Figure 4.3).

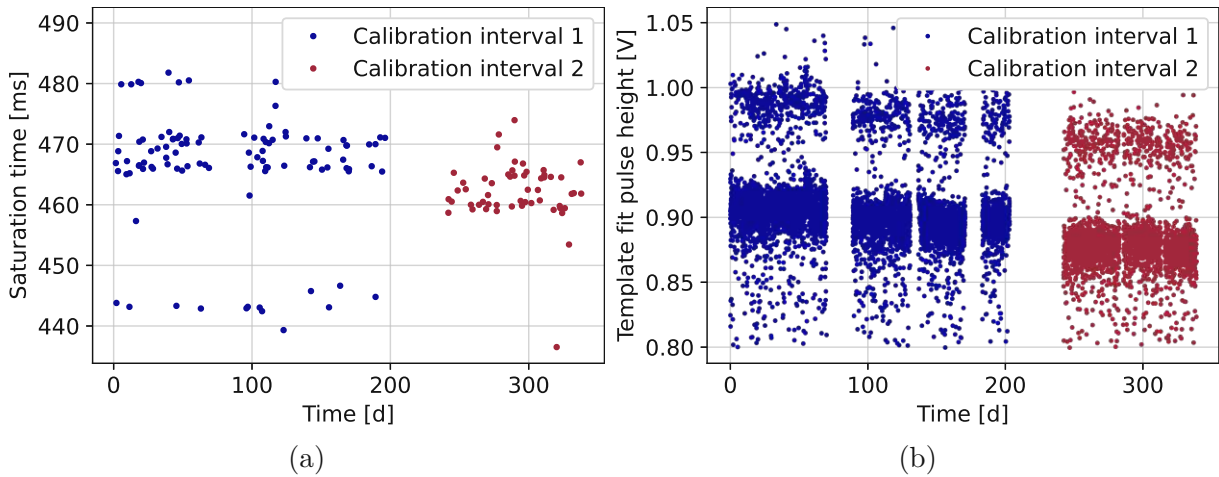


Figure 4.3.: Temporal evolution of the TUM93A-Ph detector response in the awu dataset. The (a)  $st$  in the region of  $\alpha$ -lines and the (b)  $tfph$  in the region of the  $^{55}\text{Fe}$ -lines are shown. The chosen calibration intervals, separate due to a significantly differing detector response, are represented in blue and red, respectively.

The choice of calibration intervals has to take into account that more subdivisions provide a better resolution and accuracy, while a sufficient amount of events has to be available in each interval to perform the calibrations reliably. Short time periods with an outlying detector behaviour, sometimes consisting of singular files, are discarded. This approach resembles the energy reconstruction in the low energy range, where the detector response is probed precisely by the TPs, a fit to the TP phs can be done for each TPA (see Section 3.2.6), and where unstable intervals can also be excluded. For highly energetic events, no certain information on the true amplitude of any given event is known, lines used for calibration can overlap, and the available statistics are more limited, so the simpler mode of manually defined calibration intervals is used. For TUM93A-Ph, no subdivisions are made in the bck dataset, while the awu dataset is divided into two calibration intervals. The TPs are not used for energy reconstruction in the analyses presented in this chapter, since their range is limited to relatively low energies and extrapolations would be subject to large uncertainties.

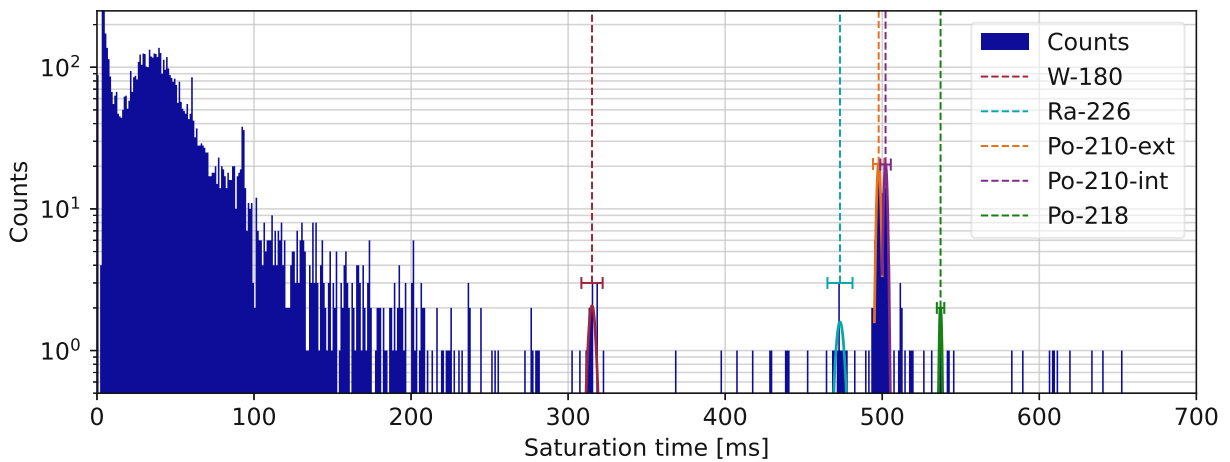


Figure 4.4.: Saturation time spectrum from the bck dataset of TUM93A-Ph. Several  $\alpha$ -lines are identified and fitted with Gaussians. The error bars indicate intervals of  $\pm 3$  fit SDs around the fit means. The histogram bins have a width of 1 ms.

The calibration of STA and TTF proceeds as described in Section 3.3, separately for each calibration interval. For the STA,  $\alpha$ -lines in the `st` spectrum are identified by comparing them to literature values and, if possible, previous studies. In the present case, [99] and [123] are consulted to ascertain which backgrounds should be expected, and the line energies are extracted from the *NuDat 3.0* web application [124]. As an exception, the  $\alpha$ -decay energy of  $^{180}\text{W}$ , an isotope with a half-life longer than  $10^{18}$  y, is taken from [125]<sup>9</sup>. The most prominent feature of the TUM93A  $\alpha$ -spectrum is a double line caused by the decay of  $^{210}\text{Po}$ :



with a total decay energy of  $Q = 5.407$  MeV, of which the  $\alpha$ -particle carries 5.304 MeV. For  $^{210}\text{Po}$ -contaminations at the crystal surface, the recoiling  $^{206}\text{Pb}$ -nucleus might escape the crystal, reducing the energy detected in the phonon channel by 103 keV [123], as compared to internal contaminations in the crystal bulk. Both the internal and the “external” (surface) lines are resolved by the STA, albeit with an overlap. Starting from this double-peak, further  $\alpha$ -lines are identified and fitted with Gaussians, as shown in Figure 4.4. Of

<sup>9</sup>The first unambiguous detection of this decay was reported by CRESST in [125].

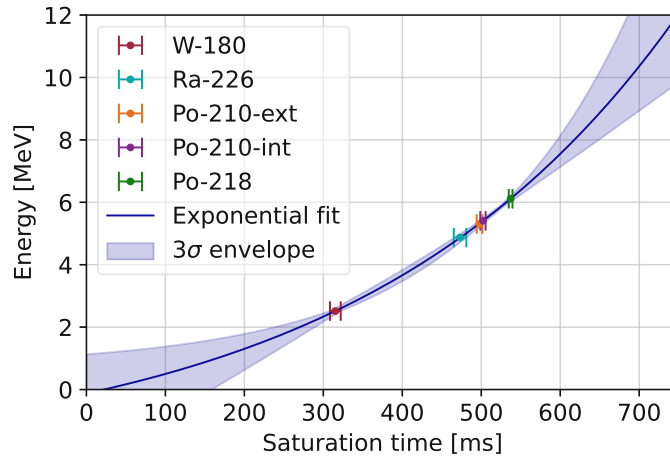


Figure 4.5.: Exponential calibration curve mapping  $st$  to energy for the bck dataset of TUM93A-Ph. The data points are obtained by Gaussian fits from the lines identified in Figure 4.4. The resulting uncertainties, given by the fit SD  $\sigma$ , are represented by the  $\pm 3\sigma$  error bars and their effect on the calibration curve is reflected by the  $3\sigma$  envelope.

the indicated peaks, the one due to  $^{226}\text{Ra}$  is potentially overlapping with a peak from  $^{234}\text{U}$ , but the difference in decay energies is lower than the expected resolution, so the peak is still used for calibration. The mean values of the Gaussian fits, together with the decay energies from the literature are fitted with an exponential calibration curve of  $st$  to energy  $E$ , see Figure 4.5. The uncertainties of the Gaussian peak fits, quantified by the fit SD  $\sigma$ , are propagated to the calibration curve by shifting each data point by  $+3\sigma$  or  $-3\sigma$  and performing the exponential fit on all possible combinations. The envelope of the resulting set of exponential curves is shown in Figure 4.5 and is used to monitor the quality and robustness of the calibration. A narrow envelope is desirable in the energy region of interest.

Identifying spectral lines is challenging, especially without prior knowledge of their activities for the detector considered. Following an iterative approach to determine the peaks in the spectrum, the calibration curve is fitted to a preliminary list of identified lines. The resulting energy spectrum helps to recognise errors in the preliminary list, yielding an updated list which is used in the next iteration.

The peaks identified in the  $st$  spectrum are further put to use in the calibration of the  $tfph$  spectrum, by tagging events that belong to a certain peak. Only the tagged events are then considered for fitting a Gaussian to the corresponding peak in the  $tfph$  spectrum. This allows to use the  $\alpha$ -peaks for calibration even if the resolution of the TTF is too bad to identify them directly. The spectra in the medium energy region between the  $^{55}\text{Fe}$  calibration peaks and the  $\alpha$ -range are typically rather flat and any potentially present peaks are hard to identify. Therefore, the  $^{55}\text{Fe}$  K- $\alpha$  line at 5.9 keV is used as another data point for the  $tfph$  calibration. Figure 4.6 shows the corresponding parts of the spectrum. An additional data point is artificially placed at 0  $tfph$  and 0 energy and a second degree polynomial calibration curve is then fit to the data, as shown in Figure 4.7. In the present case, the result is an almost linear conversion, with a rather large uncertainty indicated by the  $3\sigma$  envelope.

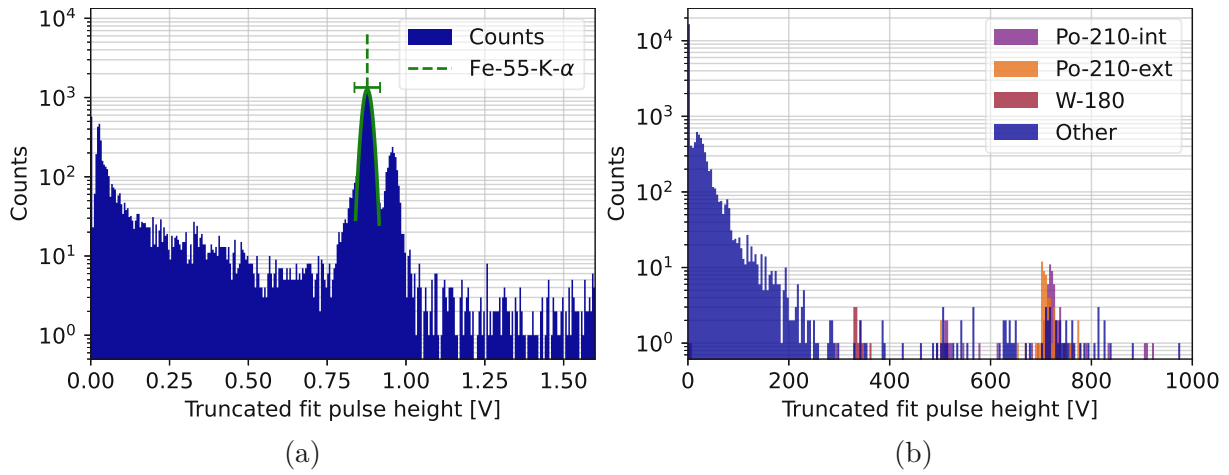


Figure 4.6.: Truncated templated fit pulse height spectrum of TUM93A-Ph in the bck dataset. (a) The low-energy region, where the  $^{55}\text{Fe}$  double-peak is visible and the K- $\alpha$  line is fit with a Gaussian. The bin width is 5 mV. At the lowest energies, the LEE can be observed, but is cut off due to the chosen trigger threshold. (b) Larger range of the spectrum containing  $\alpha$  peaks, labelled through identification from the STA, with a bin width of 4 V.

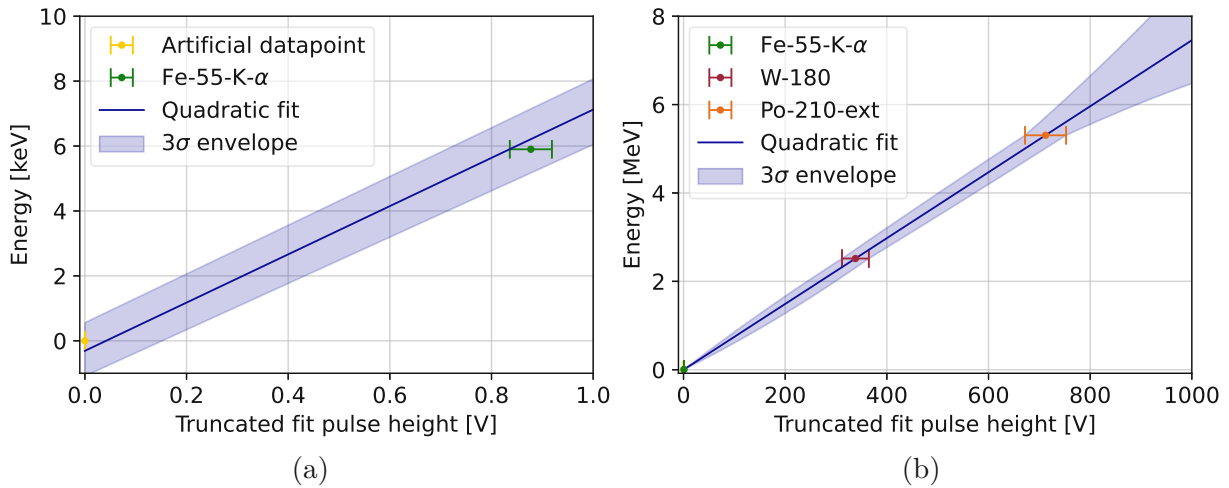


Figure 4.7.: Quadratic calibration curve mapping the  $\text{tfph}$  to energy in the bck dataset of TUM93A-Ph. The error bars represent 3 SDs around the fit mean. (a) An artificial data point is placed at the origin, as can be seen in this zoom to low energies. (b) The  $^{180}\text{W}$  and the  $^{210}\text{Po}$  surface peaks are used in the  $\alpha$ -region. The errors are propagated as in the STA calibration.

#### 4.2.4. Spectra and Likelihood Fit of Simulated Templates

The obtained calibration curves are applied to compute energy spectra from both the STA and the TTF in each calibration interval and the spectra resulting from all calibration intervals of both datasets are summed up. Figures 4.8 and 4.9 show the spectra obtained from the STA and the TTF in the  $\alpha$ -region and below, respectively. To make the spectra comparable between different modules or datasets, the number of detected counts in each histogram bin is divided by the detector exposure in kg d. To find the latter, the total live time of the detector is computed by summing the durations of all files used and

subtracting the time blocked due to heater pulses and the rate cut. The product of live time and absorber crystal mass gives the exposure, which is found to be 9.41 kg d in the case at hand.

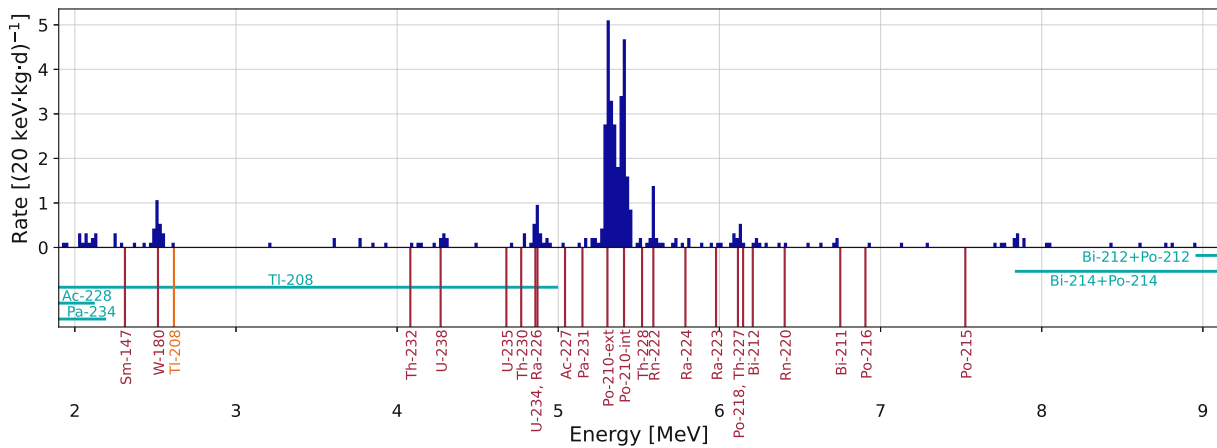


Figure 4.8.: High-energy spectrum of TUM93A-Ph as reconstructed via the STA, using the bck and awu datasets, plotted with a histogram bin width of 20 keV. Below the spectrum, literature values of  $\alpha$ -decay energies are shown in red, and potential continuous contributions from  $\beta$ -decays (or the pileup of  $\beta$ - and  $\alpha$ -decays) are depicted in teal. The energy of the  $\gamma$ -line of  $^{208}\text{Tl}$  that was reported in [123] is indicated in orange.

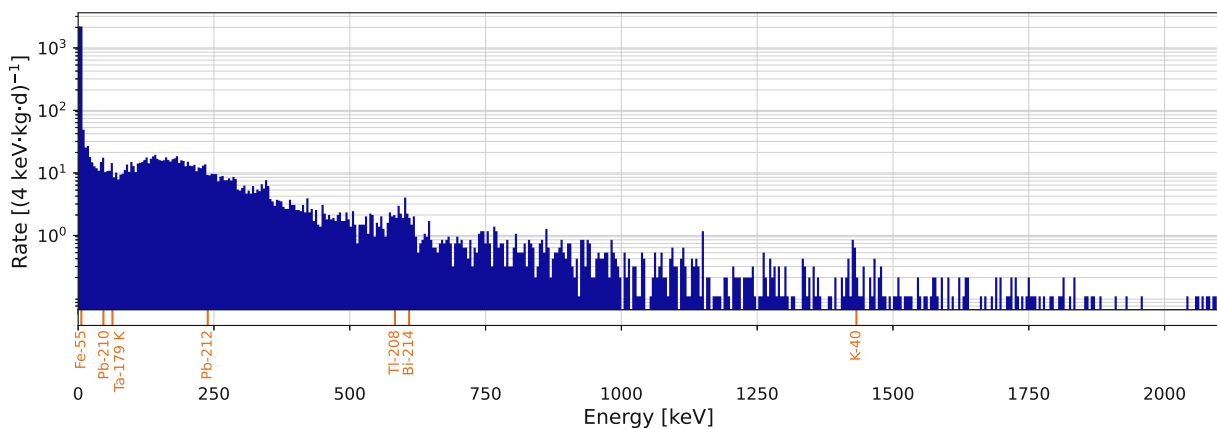


Figure 4.9.: Spectrum of TUM93A-Ph reconstructed by the TTF, up to an energy of 2100 keV, with a bin width of 4 keV. On the very left, a peak mainly due to the  $^{55}\text{Fe}$  calibration source and the LEE can be seen. Some  $\gamma$ -peaks, with literature values marked in orange, are discernible in the otherwise very continuous spectrum.

The lines in the STA spectrum are in good agreement with literature values from [124]. At the lowest and highest energies shown, contributions from continuous  $\beta$ -spectra are apparent. In the high-energy case, they are due to the pileup of a  $\beta$ -decay (for example of  $^{214}\text{Bi}$ ) and an  $\alpha$ -decay of the resulting daughter nucleus (e.g.  $^{214}\text{Po}$ ) that happen in close succession, too fast to resolve the individual contributions. Below the  $\alpha$ -region, the spectrum consists mainly of continuous components, as shown in Figure 4.9.

The calibrations are subject to errors. Systematic errors stem from the imperfect modelling of the true conversion functions by an exponential or quadratic function. The finite resolution of the data points used for calibration introduces statistical uncertainties that are especially evident in the TTF calibration, as visualised by the  $3\sigma$  envelope.

Events with apparent energies differing from the  $Q$ -values can also be due to other causes than incorrect calibrations. Firstly, the energy deposited in the main absorber may be smaller than the total decay energy, especially for external backgrounds. This can be understood from simulations and is taken into account by the likelihood fit. Secondly, the STA and TTF are not infallible and the event energy can occasionally be wrongly reconstructed, especially if artefacts come into play.

A comparison of the spectra due to both methods can be made, cross-checking their validity. Indeed, the same spectral features are observed in both cases. However, for energies much lower than the lowest calibration line of the STA (the  $^{180}\text{W}$ -line at 2516 keV), the spectrum reconstructed with the STA is shifted to the right, compared to that found by the TTF. This can be understood from the error of the STA's energy calibration, which rises significantly below the  $\alpha$ -region, as shown in Figure 4.5. The resolutions of the STA and the TTF are comparable at medium energies, down to the point where the STA fails because the pulses are no longer fully saturated. In contrast, the TTF has a degraded resolution in the  $\alpha$ -region, as compared to the STA, but less of a systematic offset, since  $\alpha$ -lines are used for its calibration alongside the  $^{55}\text{Fe}$  K- $\alpha$  line.

Comparing the STA  $\alpha$ -spectrum to the analysis previously performed in [99], the statistics are improved. In the energy range from 2.3 MeV to 10.1 MeV, the present work reconstructs 411 events at a rate of  $43.7 (\text{kg d})^{-1}$ , as compared to 311 events in [99], where the rate is  $37.7 (\text{kg d})^{-1}$ . This improvement of about 32% in reconstructed events and 16% in rate can be ascribed to the use of extended file lists as well as the optimisation of trigger settings (see the discussion on the trigger threshold in Section 4.2.1) and analysis methods. The latter are implemented as discussed in Section 3.3 for use with Python and `cait`, while [99] uses a *ROOT*-based analysis. Moreover, the cuts applied (listed in Table 4.1) are not identical to the ones employed in [99].

To finalise the preparation of data for the likelihood fit, the two spectra from the STA and the TTF are combined. Owing to its superior resolution, the STA is the method of choice in the high-energy region. It is however inapplicable to unsaturated pulses, so the TTF is the preferred option at lower energies. In the present case, the STA spectrum is used for energies exceeding 2 MeV, while the TTF provides the data for all lower energies. Owing to the low number of events around 2 MeV, this choice allows to stitch the spectra together seamlessly. Because the two spectra are never completely identical, care has to be taken to prevent the same event from appearing in both spectra. This is done by including in the STA spectrum all events with energies  $\geq 2$  MeV reconstructed by the STA, and in the TTF spectrum all events for which both methods yield an energy  $< 2$  MeV.

Apart from the spectra, the likelihood fit is also provided with the corresponding detector exposure. No survival probability simulation is carried out, since the analysed high-energy pulses do not follow the SEV shape and are moreover frequently affected by artefacts such as FQLs or SQUID resets. The latter change how pulses are processed by the trigger and through cuts, but are difficult to model. Accurately simulating these pulses and superimposing them on the stream would go far beyond the scope of this work. However, the

employed cuts are designed to keep as many physical events as possible. Still, the lack of this simulation introduces an additional uncertainty into the data.

The results of an exemplary likelihood fit to the present spectra are shown in Figure 4.10, where the TTF spectrum was used for energies between 1 keV and 2 MeV, and the STA spectrum for energies between 2 MeV and 7 MeV. Assumptions of partial secular equilibrium are made for the fit. In the lower energy region, the fit ascribes large parts of the continuous spectrum to  $^{40}\text{K}$  and leaves significant portions of the background below 500 keV unexplained. In the  $\alpha$ -region, most peaks are covered. An exception is the external  $^{210}\text{Po}$  line, which was not simulated. Likewise, the template for  $^{180}\text{W}$  is missing. The resolution of the simulated templates does not match the data, with the fitted peaks being too wide. A refined fit is in preparation by the CRESST simulation group.

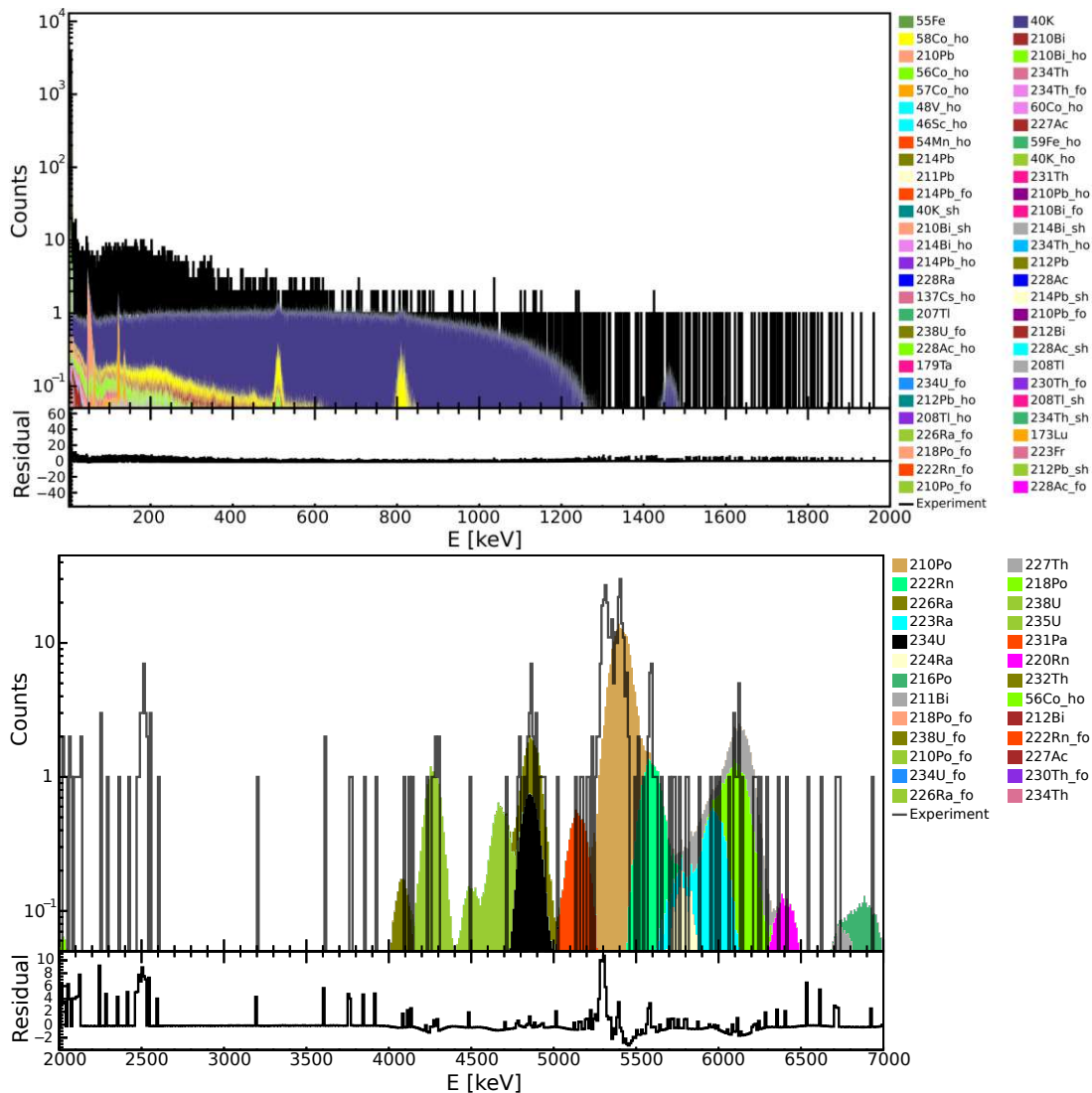


Figure 4.10.: Results of a likelihood fit of simulated spectral templates to the spectra produced in this work for TUM93A-Ph. The experimental data is shown as a black line and the spectral contributions ascribed by the fit are color-coded. Templates for the contributions of detector holders, scintillating foil and shielding are labelled with suffixes “ho”, “fo” and “sh”, respectively, with all other templates belonging to internal backgrounds.

### 4.3. TUM93C, Comm1 and Comm2

The procedures delineated in Section 4.2 for TUM93A are similarly applied to the phonon detectors of modules TUM93C, Comm1 and Comm2. Differences lie in the file lists (see the Appendix A) and all other instances where specifics of the detector response are considered, such as the choices of cut values (see Table 4.1) or calibration intervals.

The resulting spectra are shown in Figures 4.11, 4.12 and 4.13, with the same energy ranges and bin widths as for TUM93A, while the associated exposures are summarised in Table 4.2. As for TUM93A, the entire bck dataset of TUM93C is calibrated at once, but in the awu dataset, 3 instead of 2 calibration intervals are used. For both Comm modules, the bck dataset is subdivided into 4 and the awu dataset into 2 calibration intervals, though the individual intervals are not identical. For the calibration of TUM93C, the same lines are used as for TUM93A, while the calibrations of Comm1 and Comm2 rely on lines from  $^{55}\text{Fe}$ ,  $^{147}\text{Sm}$ ,  $^{238}\text{U}$ ,  $^{226}\text{Ra}$  (not resolved individually from  $^{234}\text{U}$ ),  $^{210}\text{Po}$  (internal and surface),  $^{222}\text{Rn}$  and  $^{211}\text{Bi}$ .

A large share of the awu dataset has to be excluded from the analysis of Comm1 due to heater pulses whose timestamps seem to be missing from the corresponding files, causing them to be regarded as events by the trigger. The same issue can be overcome for the other modules by means of a stringent cut on the onset, but not in Comm1, leading to a reduced exposure.

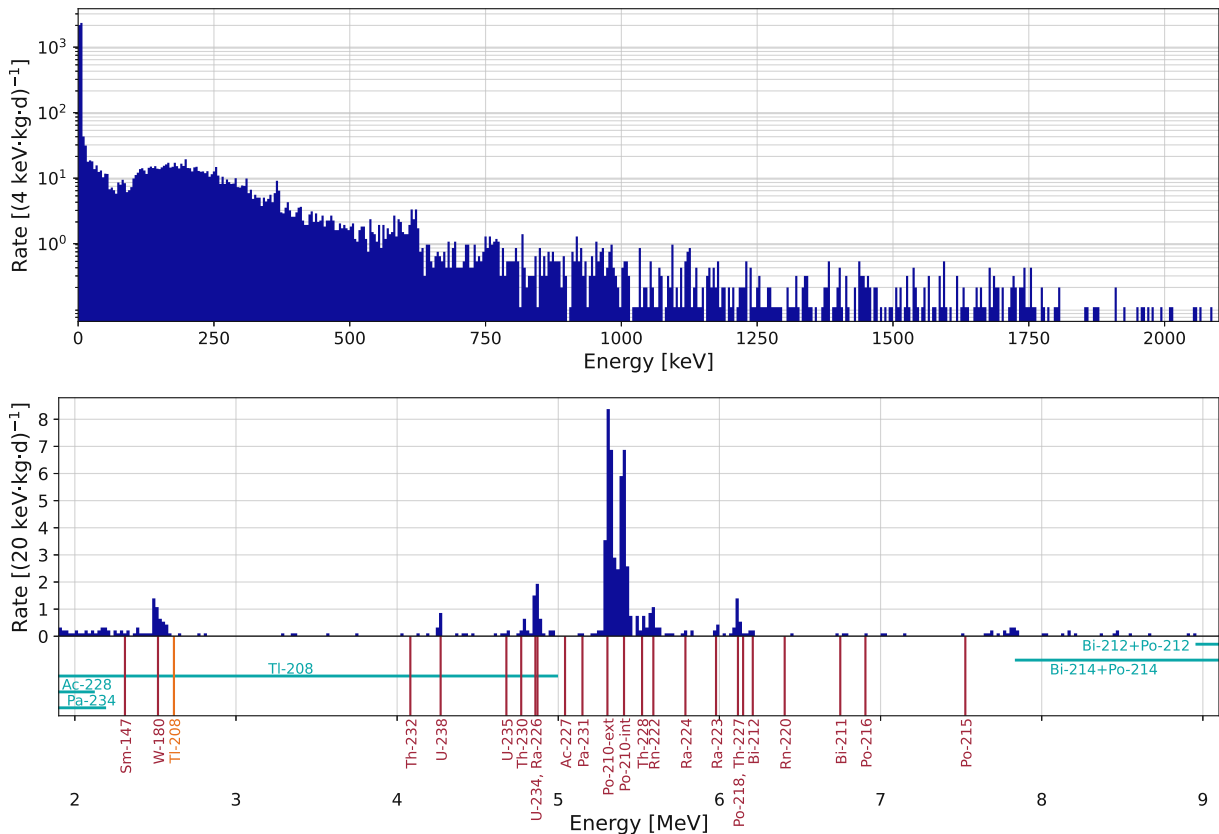


Figure 4.11.: Spectra of TUM93C-Ph found with the TTF (top) and the STA (bottom). Literature values for potentially expected contributions to the spectrum are shown as in Figure 4.8.

Since the absorbers of TUM93A and TUM93C are cut from the same crystal, the spectra are expected to be similar, with differences being explicable by segregation effects during crystal growth. From a rough estimate, an increased level of impurities is seen in TUM93C, which was cut from the lower part of the crystal: between 2 MeV and 9 MeV, 425 counts are registered in TUM93A and 669 in TUM93C, even though the exposure of TUM93C is slightly lower (see Table 4.2). The apparent peaks in the spectra of both modules are agree well in their positions and relative heights, but the rates are generally higher in TUM93C. Analysing the properties of the TUM93 crystal overall, a combined likelihood fit to the data of both detectors could be performed.

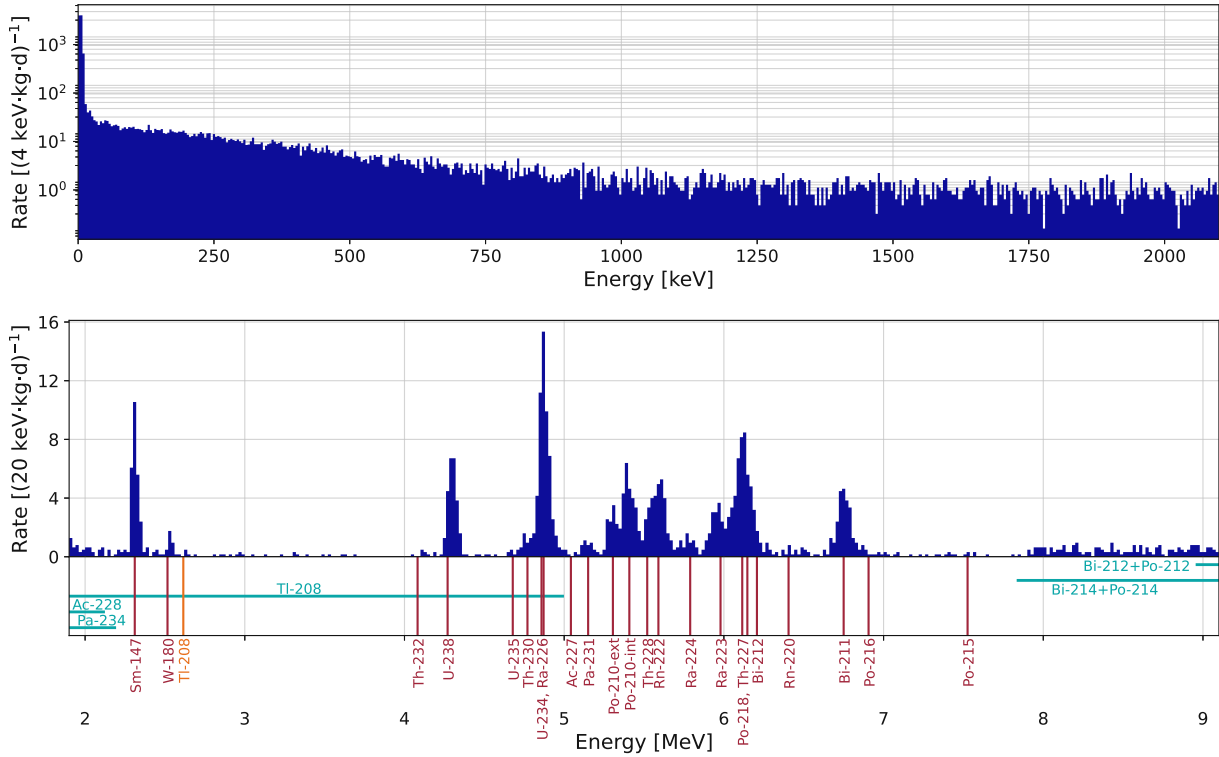


Figure 4.12.: Spectra of Comm1-Ph found with the TTF (top) and the STA (bottom). Literature values for potentially expected contributions to the spectrum are shown as in Figure 4.8.

Module	TUM93A	TUM93C	Comm1	Comm2
<b>Exposure bck</b> [kg d]	4.60	4.62	4.34	4.52
<b>Exposure awu</b> [kg d]	4.80	4.70	1.92	4.56
<b>Total exposure</b> [kg d]	9.41	9.31	6.26	9.08

Table 4.2.: Detector exposures due to the selected files (see the lists in the Appendix A) and the dead time induced by heater pulses and rate cuts.

The commercial crystals exhibit a much higher level of radioactive contaminations than TUM93, as is evident from the spectra in Figures 4.12 and 4.13. Apart from the  $^{210}\text{Po}$  double-peak, a number of other peaks are clearly developed in the  $\alpha$ -region. For the spectra created via the TTF, the resolution is significantly degraded, leading to a lack of clear features that is even more noticeable than in the TUM detectors. This can be

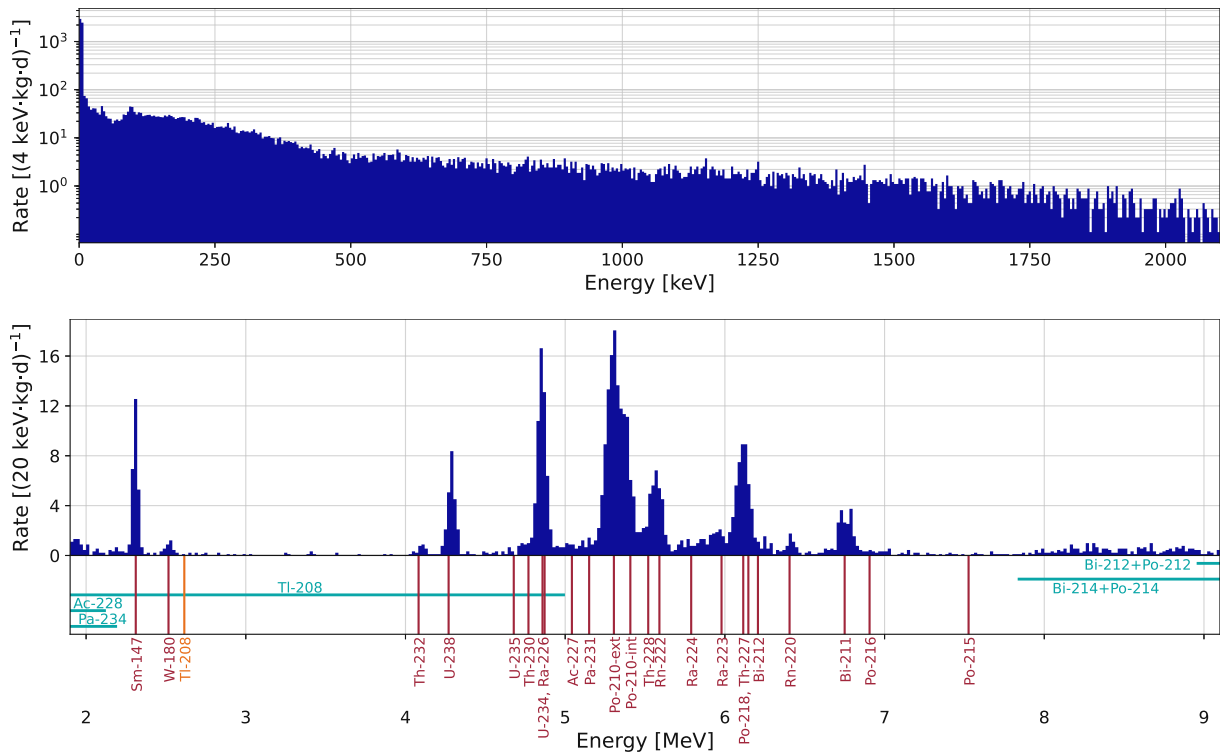


Figure 4.13.: Spectra of Comm2-Ph found with the TTF (top) and the STA (bottom). Literature values for potentially expected contributions to the spectrum are shown as in Figure 4.8.

explained at least in part by much longer saturation times in the Comm detectors for the same energy deposition. SEV fits to the resulting very long pulses perform poorly. The tagging of  $\alpha$ -peaks for the energy calibration of the TTF is decidedly necessary, as no  $\alpha$ -peaks can a priori be resolved in the TTF spectra. Even with the help of the STA, the calibration curves of the TTF are affected by large uncertainties. The use of an even longer record window, with a length of e.g.  $2^{17}$  samples, could prove to be beneficial for the TTF, but the creation of a clean SEV of this length comes with its own set of challenges, due to limited statistics and the high probability of pileups. With the given record length of  $2^{16}$  samples, some improvements of the TTF performance for the Comm modules could potentially be achieved by more optimal choices of the truncation level, the pileup handling and the baseline fit. However, the anticipated gains in resolution are expected to be rather small and it may be a better approach to extend the use of the STA to much lower energies in the Comm modules. For this to be accurate, at least one additional data point for calibration would be needed at lower energies, which seems difficult to find, given the flat spectra, unless an artificial data point is used. Another challenge would be the determination of a meaningful separation point (other than 2 MeV) to stitch the spectra from both methods together, because no resolution of either method can be ascertained without the presence of peaks. Anyhow, the present spectra from the STA already provide a solid basis for likelihood fits in the high-energy region.

At the highest examined energies, pulses likely stemming from fast consecutive  $\beta$ - and  $\alpha$ -decays are observed in all four detectors. As for other decays, the rates of these events are higher in the Comm modules, and a spectrum of the relevant region from Comm2 is shown in Figure 4.14. Some of the events with the highest reconstructed energies can be

ascribed to the successive  $\alpha$ -decays of  $^{219}\text{Rn}$  and  $^{215}\text{Po}$ . Clearly, the resolution of the STA is degraded at the large energies concerned. Moreover, the lines used for calibration all lie below 7 MeV, so the confidence in the conversion's accuracy in the considered energy range is rather low. Still, the in principle feasibility to extend the reach of the STA to energies beyond 10 MeV is demonstrated.

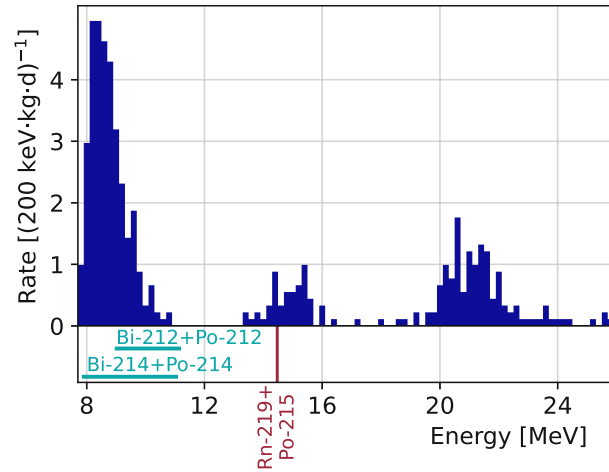


Figure 4.14.: Spectrum of Comm2-Ph reconstructed with the STA for the highest accessible energies. The literature energies of contributions expected in this range (following [123]) are marked below the spectrum.

# 5. CONCLUSION

A thorough understanding of the backgrounds present in CRESST is necessary to further improve the quality of its detectors and enhance the experiment's potential for the discovery of dark matter. Due to recent detector designs employing small target crystal masses, a large portion of the background spectra is not readily accessible through methods intended for the analysis of low-energy events, which are most relevant for the dark matter search in CRESST. In the scope of this thesis, two approaches that extend the available energy range were examined, implemented, improved and applied to data taken by four different detectors during the Run36 data taking campaign. Procedures for reconstructing the event energy with these techniques were discussed. For calibration, prominent lines from radioactive  $\alpha$ -decays and a  $^{55}\text{Fe}$  X-ray source were used, taking into account temporal changes of the detector response.

The two methods treated are the truncated template fit and the saturation time analysis. The former allows, in principle, to generate a continuous spectrum from the lowest energies accessible to the experiment, up to the MeV region, where contributions from  $\alpha$ -decays can be observed. However, the construction of a suitable pulse template, and the necessity to choose several meta-parameters for the application of this procedure make an exploitation of its full potential challenging. Especially when the considered pulses are very long, the resolution of the truncated template fit is severely limited, as is particularly apparent for the Comm1 and Comm2 detectors investigated in this work. Using even longer voltage traces could help to improve the method's performance in these cases, but seems difficult. As the tool of choice for long, completely saturated pulses, the saturation time analysis is capable of determining the energies of highly energetic events with good precision. The use of longer voltage traces to extend the energy reach is straightforward for this method.

The obtained  $\alpha$ -spectra of the investigated modules contain a number of distinct peaks that are clearly resolved by the saturation time analysis. Conforming to the expectations, the commercially produced crystals of the Comm1 and Comm2 modules evidently contain larger amounts of radioactive impurities than the purified TUM93 crystal. The precise composition of the background components and their activities are to be determined via Bayesian likelihood fits of spectral templates to the calculated spectra. Ideally, a survival probability simulation for high-energy pulses would be used to correct the spectra for the loss of physical events that were not triggered, or removed by cuts. However, this appears complicated to carry out accurately, mainly due to the irregular pulse shapes and artefacts associated with large pulses. Nonetheless, the analysis chain developed in the context of this thesis can be used to extend the energy ranges of other detectors. Ultimately, spectra from all modules can be analysed and compared to gain an understanding of the overall backgrounds of Run36 detectors.

# A. LISTS OF ANALYSED FILES

Tables A.1, A.2, A.3 and A.4 list the files used in the analyses of TUM93A, TUM93C, Comm1 and Comm2, respectively. As the selections were refined to exclude problematic files throughout the analyses, these lists are only strictly valid for the main part of the analyses, performed on the continuously recorded data. Some additional files may have been used in the processing of hardware-triggered data, and been discarded after software triggering.

bck_002	bck_003	bck_004	bck_005	bck_006	bck_007	bck_008	bck_009	bck_010
bck_011	bck_012	bck_013	bck_014	bck_016	bck_017	bck_018	bck_019	bck_020
bck_021	bck_022	bck_024	bck_025	bck_026	bck_027	bck_028	bck_030	bck_031
bck_032	bck_034	bck_036	bck_037	bck_038	bck_039	bck_040	bck_041	bck_042
bck_043	bck_044	bck_045	bck_046	bck_047	bck_048	bck_049	bck_050	bck_051
bck_052	bck_054	bck_055	bck_056	bck_057	bck_058	bck_060	bck_061	bck_062
bck_066	bck_067	bck_069	bck_070	bck_071	bck_072	bck_073	bck_074	bck_077
bck_078	bck_079	bck_080	bck_081	bck_082	bck_083	bck_084	bck_085	bck_086
bck_087	bck_088	bck_089	bck_090	bck_091	bck_092	bck_093	bck_094	bck_095
bck_096	bck_097	bck_098	bck_099	bck_100	bck_101	bck_102	bck_103	bck_104
bck_105	bck_106	bck_107	bck_108	bck_109	bck_110	bck_111	bck_112	bck_113
bck_114	bck_116	bck_119	bck_120	bck_121	bck_122	bck_123	bck_124	bck_125
bck_127	bck_128	bck_129	bck_130	bck_131				
awu_bck_002	awu_bck_003	awu_bck_005	awu_bck_007	awu_bck_008	awu_bck_009			
awu_bck_010	awu_bck_011	awu_bck_012	awu_bck_013	awu_bck_014	awu_bck_015			
awu_bck_016	awu_bck_017	awu_bck_018	awu_bck_019	awu_bck_020	awu_bck_021			
awu_bck_022	awu_bck_023	awu_bck_024	awu_bck_025	awu_bck_026	awu_bck_027			
awu_bck_028	awu_bck_029	awu_bck_030	awu_bck_031	awu_bck_032	awu_bck_033			
awu_bck_034	awu_bck_035	awu_bck_037	awu_bck_038	awu_bck_039	awu_bck_040			
awu_bck_041	awu_bck_042	awu_bck_043	awu_bck_044	awu_bck_045	awu_bck_046			
awu_bck_047	awu_bck_048	awu_bck_049	awu_bck_050	awu_bck_051	awu_bck_052			
awu_bck_053	awu_bck_054	awu_bck_055	awu_bck_056	awu_bck_057	awu_bck_059			
awu_bck_063	awu_bck_064	awu_bck_065	awu_bck_066	awu_bck_067	awu_bck_068			
awu_bck_069	awu_bck_070	awu_bck_072	awu_bck_073	awu_bck_074	awu_bck_075			
awu_bck_076	awu_bck_077	awu_bck_078	awu_bck_079	awu_bck_080	awu_bck_081			
awu_bck_082	awu_bck_083	awu_bck_084	awu_bck_085	awu_bck_086	awu_bck_087			
awu_bck_088	awu_bck_090	awu_bck_091	awu_bck_092	awu_bck_093	awu_bck_094			
awu_bck_095	awu_bck_099	awu_bck_113	awu_bck_114	awu_bck_115	awu_bck_116			
awu_bck_117	awu_bck_118	awu_bck_119	awu_bck_120	awu_bck_121	awu_bck_122			
awu_bck_123	awu_bck_124	awu_bck_125	awu_bck_126	awu_bck_127	awu_bck_128			
awu_bck_129	awu_bck_130	awu_bck_132	awu_bck_133	awu_bck_134	awu_bck_135			
awu_bck_136	awu_bck_137	awu_bck_138	awu_bck_139	awu_bck_140	awu_bck_141			
awu_bck_142	awu_bck_143	awu_bck_144	awu_bck_146	awu_bck_147	awu_bck_148			
awu_bck_149	awu_bck_150	awu_bck_151	awu_bck_152	awu_bck_153	awu_bck_154			
awu_bck_155								

Table A.1.: Files used in the analysis of TUM93A.

---

bck_002	bck_003	bck_004	bck_005	bck_006	bck_007	bck_008	bck_009	bck_010
bck_011	bck_012	bck_013	bck_014	bck_016	bck_017	bck_018	bck_019	bck_020
bck_021	bck_022	bck_024	bck_025	bck_026	bck_027	bck_028	bck_030	bck_031
bck_032	bck_034	bck_036	bck_037	bck_038	bck_039	bck_040	bck_041	bck_042
bck_043	bck_044	bck_045	bck_046	bck_047	bck_048	bck_049	bck_050	bck_051
bck_052	bck_054	bck_055	bck_056	bck_057	bck_058	bck_060	bck_061	bck_062
bck_066	bck_067	bck_069	bck_070	bck_071	bck_072	bck_073	bck_074	bck_077
bck_078	bck_079	bck_080	bck_081	bck_082	bck_083	bck_084	bck_085	bck_086
bck_087	bck_088	bck_089	bck_090	bck_091	bck_092	bck_093	bck_094	bck_095
bck_096	bck_097	bck_098	bck_099	bck_100	bck_101	bck_102	bck_103	bck_104
bck_105	bck_106	bck_107	bck_108	bck_109	bck_110	bck_111	bck_112	bck_113
bck_114	bck_115	bck_116	bck_119	bck_120	bck_121	bck_122	bck_123	bck_124
bck_125	bck_127	bck_128	bck_129	bck_130	bck_131			
awu_bck_002	awu_bck_003	awu_bck_005	awu_bck_007	awu_bck_008	awu_bck_009			
awu_bck_010	awu_bck_011	awu_bck_012	awu_bck_013	awu_bck_014	awu_bck_015			
awu_bck_016	awu_bck_017	awu_bck_018	awu_bck_019	awu_bck_020	awu_bck_021			
awu_bck_022	awu_bck_023	awu_bck_024	awu_bck_025	awu_bck_026	awu_bck_027			
awu_bck_028	awu_bck_029	awu_bck_030	awu_bck_031	awu_bck_032	awu_bck_033			
awu_bck_034	awu_bck_035	awu_bck_037	awu_bck_038	awu_bck_039	awu_bck_040			
awu_bck_041	awu_bck_043	awu_bck_044	awu_bck_045	awu_bck_046	awu_bck_047			
awu_bck_048	awu_bck_049	awu_bck_050	awu_bck_051	awu_bck_052	awu_bck_053			
awu_bck_054	awu_bck_055	awu_bck_056	awu_bck_057	awu_bck_059	awu_bck_063			
awu_bck_064	awu_bck_065	awu_bck_066	awu_bck_067	awu_bck_068	awu_bck_069			
awu_bck_070	awu_bck_072	awu_bck_073	awu_bck_074	awu_bck_075	awu_bck_076			
awu_bck_077	awu_bck_078	awu_bck_079	awu_bck_081	awu_bck_082	awu_bck_083			
awu_bck_085	awu_bck_086	awu_bck_088	awu_bck_092	awu_bck_093	awu_bck_095			
awu_bck_099	awu_bck_112	awu_bck_113	awu_bck_114	awu_bck_115	awu_bck_116			
awu_bck_117	awu_bck_118	awu_bck_119	awu_bck_120	awu_bck_121	awu_bck_122			
awu_bck_123	awu_bck_124	awu_bck_125	awu_bck_126	awu_bck_127	awu_bck_128			
awu_bck_129	awu_bck_130	awu_bck_132	awu_bck_133	awu_bck_134	awu_bck_135			
awu_bck_136	awu_bck_137	awu_bck_138	awu_bck_139	awu_bck_140	awu_bck_141			
awu_bck_142	awu_bck_143	awu_bck_144	awu_bck_146	awu_bck_147	awu_bck_148			
awu_bck_149	awu_bck_150	awu_bck_151	awu_bck_152	awu_bck_153	awu_bck_154			
awu_bck_155								

---

Table A.2.: Files used in the analysis of TUM93C.

bck_002	bck_003	bck_004	bck_005	bck_006	bck_007	bck_008	bck_009	bck_010
bck_011	bck_012	bck_013	bck_014	bck_016	bck_017	bck_018	bck_019	bck_020
bck_021	bck_022	bck_024	bck_025	bck_026	bck_027	bck_028	bck_030	bck_031
bck_032	bck_034	bck_036	bck_037	bck_038	bck_039	bck_040	bck_041	bck_042
bck_043	bck_044	bck_045	bck_046	bck_047	bck_048	bck_049	bck_050	bck_051
bck_052	bck_054	bck_055	bck_056	bck_057	bck_058	bck_060	bck_061	bck_062
bck_066	bck_067	bck_069	bck_070	bck_071	bck_072	bck_073	bck_074	bck_077
bck_078	bck_079	bck_080	bck_081	bck_082	bck_084	bck_085	bck_086	bck_087
bck_088	bck_089	bck_090	bck_091	bck_092	bck_093	bck_095	bck_096	bck_097
bck_098	bck_099	bck_100	bck_101	bck_102	bck_104	bck_105	bck_106	bck_107
bck_108	bck_109	bck_110	bck_111	bck_112	bck_113	bck_114	bck_120	bck_121
bck_122	bck_123	bck_124	bck_125	bck_127	bck_128	bck_129	bck_130	bck_131
awu_bck_002	awu_bck_003	awu_bck_005	awu_bck_007	awu_bck_008	awu_bck_009			
awu_bck_010	awu_bck_011	awu_bck_012	awu_bck_013	awu_bck_014	awu_bck_015			
awu_bck_016	awu_bck_017	awu_bck_018	awu_bck_019	awu_bck_020	awu_bck_021			
awu_bck_022	awu_bck_023	awu_bck_024	awu_bck_025	awu_bck_026	awu_bck_027			
awu_bck_028	awu_bck_029	awu_bck_037	awu_bck_039	awu_bck_040	awu_bck_041			
awu_bck_042	awu_bck_043	awu_bck_044	awu_bck_045	awu_bck_046	awu_bck_047			
awu_bck_048	awu_bck_049	awu_bck_050	awu_bck_051	awu_bck_052	awu_bck_053			
awu_bck_054	awu_bck_057	awu_bck_063	awu_bck_070	awu_bck_072	awu_bck_081			
awu_bck_086	awu_bck_087	awu_bck_088	awu_bck_093	awu_bck_094				

Table A.3.: Files used in the analysis of Comm1.

---

bck_002	bck_003	bck_004	bck_005	bck_006	bck_007	bck_008	bck_009	bck_010
bck_011	bck_012	bck_013	bck_014	bck_016	bck_017	bck_018	bck_019	bck_020
bck_021	bck_022	bck_024	bck_025	bck_026	bck_027	bck_028	bck_030	bck_031
bck_032	bck_034	bck_036	bck_037	bck_038	bck_039	bck_040	bck_041	bck_042
bck_043	bck_044	bck_045	bck_046	bck_047	bck_048	bck_049	bck_050	bck_051
bck_052	bck_054	bck_055	bck_056	bck_057	bck_058	bck_060	bck_061	bck_062
bck_066	bck_067	bck_070	bck_071	bck_072	bck_073	bck_074	bck_077	bck_078
bck_079	bck_080	bck_081	bck_082	bck_083	bck_084	bck_085	bck_086	bck_087
bck_088	bck_089	bck_090	bck_091	bck_092	bck_093	bck_094	bck_095	bck_096
bck_097	bck_098	bck_099	bck_100	bck_101	bck_102	bck_103	bck_104	bck_105
bck_106	bck_107	bck_108	bck_109	bck_110	bck_111	bck_112	bck_113	bck_114
bck_119	bck_120	bck_121	bck_122	bck_123	bck_124	bck_125	bck_127	bck_128
bck_129	bck_130	bck_131						
awu_bck_002	awu_bck_003	awu_bck_005	awu_bck_007	awu_bck_008	awu_bck_009			
awu_bck_010	awu_bck_011	awu_bck_012	awu_bck_013	awu_bck_014	awu_bck_015			
awu_bck_016	awu_bck_017	awu_bck_018	awu_bck_019	awu_bck_020	awu_bck_021			
awu_bck_022	awu_bck_023	awu_bck_024	awu_bck_025	awu_bck_026	awu_bck_027			
awu_bck_028	awu_bck_029	awu_bck_030	awu_bck_031	awu_bck_032	awu_bck_033			
awu_bck_034	awu_bck_035	awu_bck_037	awu_bck_038	awu_bck_039	awu_bck_040			
awu_bck_041	awu_bck_042	awu_bck_043	awu_bck_044	awu_bck_045	awu_bck_046			
awu_bck_047	awu_bck_048	awu_bck_049	awu_bck_050	awu_bck_051	awu_bck_052			
awu_bck_053	awu_bck_054	awu_bck_055	awu_bck_056	awu_bck_057	awu_bck_059			
awu_bck_063	awu_bck_064	awu_bck_065	awu_bck_066	awu_bck_067	awu_bck_068			
awu_bck_069	awu_bck_070	awu_bck_072	awu_bck_073	awu_bck_074	awu_bck_075			
awu_bck_077	awu_bck_078	awu_bck_079	awu_bck_081	awu_bck_082	awu_bck_086			
awu_bck_087	awu_bck_088	awu_bck_091	awu_bck_093	awu_bck_094	awu_bck_112			
awu_bck_113	awu_bck_114	awu_bck_115	awu_bck_116	awu_bck_117	awu_bck_118			
awu_bck_119	awu_bck_120	awu_bck_121	awu_bck_122	awu_bck_123	awu_bck_124			
awu_bck_126	awu_bck_127	awu_bck_128	awu_bck_129	awu_bck_130	awu_bck_132			
awu_bck_133	awu_bck_134	awu_bck_135	awu_bck_136	awu_bck_137	awu_bck_138			
awu_bck_139	awu_bck_140	awu_bck_141	awu_bck_142	awu_bck_143	awu_bck_144			
awu_bck_146	awu_bck_147	awu_bck_148	awu_bck_149	awu_bck_150	awu_bck_151			
awu_bck_152	awu_bck_153	awu_bck_154	awu_bck_155					

---

Table A.4.: Files used in the analysis of Comm2.

# BIBLIOGRAPHY

- [1] Isaac Newton. *Philosophiæ Naturalis Principia Mathematica*. England, 1687.
- [2] T. Standage. *The Neptune File: Planet Detectives and the Discovery of Worlds Unseen*. Allen Lane, 2000. ISBN: 978-0-7139-9472-8. URL: <https://archive.org/details/neptunefile0000unse/page/n9/mode/2up>.
- [3] CMS Collaboration. “Observation of a new boson at a mass of 125 GeV with the CMS experiment at the LHC”. In: *Physics Letters B* 716.1 (2012), pp. 30–61. ISSN: 0370-2693. DOI: <https://doi.org/10.1016/j.physletb.2012.08.021>. URL: <https://www.sciencedirect.com/science/article/pii/S0370269312008581>.
- [4] ATLAS Collaboration. “Observation of a new particle in the search for the Standard Model Higgs boson with the ATLAS detector at the LHC”. In: *Physics Letters B* 716.1 (2012), pp. 1–29. ISSN: 0370-2693. DOI: <https://doi.org/10.1016/j.physletb.2012.08.020>. URL: <https://www.sciencedirect.com/science/article/pii/S037026931200857X>.
- [5] Peter W. Higgs. “Broken Symmetries and the Masses of Gauge Bosons”. In: *Physical Review Letters* 13.16 (Oct. 19, 1964), pp. 508–509. ISSN: 0031-9007. DOI: [10.1103/PhysRevLett.13.508](https://doi.org/10.1103/PhysRevLett.13.508). URL: <https://link.aps.org/doi/10.1103/PhysRevLett.13.508> (visited on 12/28/2024).
- [6] F. Englert and R. Brout. “Broken Symmetry and the Mass of Gauge Vector Mesons”. In: *Physical Review Letters* 13.9 (Aug. 31, 1964), pp. 321–323. ISSN: 0031-9007. DOI: [10.1103/PhysRevLett.13.321](https://doi.org/10.1103/PhysRevLett.13.321). URL: <https://link.aps.org/doi/10.1103/PhysRevLett.13.321> (visited on 12/28/2024).
- [7] G. S. Guralnik, C. R. Hagen, and T. W. B. Kibble. “Global Conservation Laws and Massless Particles”. In: *Physical Review Letters* 13.20 (Nov. 16, 1964), pp. 585–587. ISSN: 0031-9007. DOI: [10.1103/PhysRevLett.13.585](https://doi.org/10.1103/PhysRevLett.13.585). URL: <https://link.aps.org/doi/10.1103/PhysRevLett.13.585> (visited on 12/28/2024).
- [8] Gianfranco Bertone, Dan Hooper, and Joseph Silk. “Particle dark matter: evidence, candidates and constraints”. In: *Physics Reports* 405.5 (Jan. 2005), pp. 279–390. ISSN: 03701573. DOI: [10.1016/j.physrep.2004.08.031](https://doi.org/10.1016/j.physrep.2004.08.031). URL: <https://linkinghub.elsevier.com/retrieve/pii/S0370157304003515> (visited on 03/20/2025).
- [9] Susana Cebrián. “Review on dark matter searches”. In: *Journal of Physics: Conference Series* 2502.1 (May 1, 2023), p. 012004. ISSN: 1742-6588, 1742-6596. DOI: [10.1088/1742-6596/2502/1/012004](https://doi.org/10.1088/1742-6596/2502/1/012004). URL: <https://iopscience.iop.org/article/10.1088/1742-6596/2502/1/012004> (visited on 12/30/2024).
- [10] Jennifer M. Gaskins. “A review of indirect searches for particle dark matter”. In: *Contemporary Physics* 57.4 (Oct. 2016), pp. 496–525. ISSN: 0010-7514, 1366-5812. DOI: [10.1080/00107514.2016.1175160](https://doi.org/10.1080/00107514.2016.1175160). URL: <https://www.tandfonline.com/doi/full/10.1080/00107514.2016.1175160> (visited on 12/30/2024).

- [11] Albert De Roeck. “Dark matter searches at accelerators”. In: *Nuclear Physics B* 1003 (June 2024), p. 116480. ISSN: 05503213. DOI: [10.1016/j.nuclphysb.2024.116480](https://doi.org/10.1016/j.nuclphysb.2024.116480). URL: <https://linkinghub.elsevier.com/retrieve/pii/S0550321324000464> (visited on 12/30/2024).
- [12] Vera C. Rubin and W. Kent Ford Jr. “Rotation of the Andromeda Nebula from a Spectroscopic Survey of Emission Regions”. In: *apj* 159 (Feb. 1970), p. 379. DOI: [10.1086/150317](https://doi.org/10.1086/150317). URL: <https://ui.adsabs.harvard.edu/abs/1970ApJ...159..379R>.
- [13] V. C. Rubin, N. Thonnard, and W. K. Ford Jr. “Extended rotation curves of high-luminosity spiral galaxies. IV - Systematic dynamical properties, SA through SC”. In: *The Astrophysical Journal* 225 (Nov. 1978), p. L107. ISSN: 0004-637X, 1538-4357. DOI: [10.1086/182804](https://doi.org/10.1086/182804). URL: <http://adsabs.harvard.edu/doi/10.1086/182804> (visited on 01/06/2025).
- [14] D. H. Rogstad and G. S. Shostak. “Gross Properties of Five Scd Galaxies as Determined from 21-CENTIMETER Observations”. In: *The Astrophysical Journal* 176 (Sept. 1972), p. 315. ISSN: 0004-637X, 1538-4357. DOI: [10.1086/151636](https://doi.org/10.1086/151636). URL: <http://adsabs.harvard.edu/doi/10.1086/151636> (visited on 01/06/2025).
- [15] M. S. Roberts and A. H. Rots. “Comparison of Rotation Curves of Different Galaxy Types”. In: *Astronomy and Astrophysics* 26 (Aug. 1, 1973). ADS Bibcode: 1973A&A....26..483R, pp. 483–485. ISSN: 0004-6361. URL: <https://ui.adsabs.harvard.edu/abs/1973A&A....26..483R> (visited on 01/06/2025).
- [16] Paolo Salucci and Annamaria Borriello. “The Intriguing Distribution of Dark Matter in Galaxies”. In: *Particle Physics in the New Millennium*. Ed. by Josip Trampetić and Julius Wess. Red. by R. Beig et al. Vol. 616. Series Title: Lecture Notes in Physics. Berlin, Heidelberg: Springer Berlin Heidelberg, 2003, pp. 66–77. ISBN: 978-3-540-36539-6. DOI: [10.1007/3-540-36539-7\\_5](https://doi.org/10.1007/3-540-36539-7_5). URL: [http://link.springer.com/10.1007/3-540-36539-7\\_5](http://link.springer.com/10.1007/3-540-36539-7_5) (visited on 01/06/2025).
- [17] K. G. Begeman, A. H. Broeils, and R. H. Sanders. “Extended rotation curves of spiral galaxies: dark haloes and modified dynamics”. In: *Monthly Notices of the Royal Astronomical Society* 249.3 (Apr. 1, 1991), pp. 523–537. ISSN: 0035-8711, 1365-2966. DOI: [10.1093/mnras/249.3.523](https://doi.org/10.1093/mnras/249.3.523). URL: <https://academic.oup.com/mnras/article-lookup/doi/10.1093/mnras/249.3.523> (visited on 01/06/2025).
- [18] S. M. Faber and R. E. Jackson. “Velocity dispersions and mass-to-light ratios for elliptical galaxies”. In: *The Astrophysical Journal* 204 (Mar. 1976), p. 668. ISSN: 0004-637X, 1538-4357. DOI: [10.1086/154215](https://doi.org/10.1086/154215). URL: <http://adsabs.harvard.edu/doi/10.1086/154215> (visited on 01/06/2025).
- [19] G. Illingworth. “The masses of globular clusters. II - Velocity dispersions and mass-to-light ratios”. In: *The Astrophysical Journal* 204 (Feb. 1976), p. 73. ISSN: 0004-637X, 1538-4357. DOI: [10.1086/154152](https://doi.org/10.1086/154152). URL: <http://adsabs.harvard.edu/doi/10.1086/154152> (visited on 01/06/2025).
- [20] F. Zwicky. “Die Rotverschiebung von extragalaktischen Nebeln”. In: *Helvetica Physica Acta* 6 (Jan. 1933), pp. 110–127. URL: <https://ui.adsabs.harvard.edu/abs/1933AcHPh...6..110Z>.

- [21] Edwin Hubble. “A relation between distance and radial velocity among extra-galactic nebulae”. In: *Proceedings of the National Academy of Sciences* 15.3 (Mar. 15, 1929), pp. 168–173. ISSN: 0027-8424, 1091-6490. DOI: [10.1073/pnas.15.3.168](https://doi.org/10.1073/pnas.15.3.168). URL: <https://pnas.org/doi/full/10.1073/pnas.15.3.168> (visited on 02/18/2025).
- [22] G. Lemaître. “Un Univers homogène de masse constante et de rayon croissant rendant compte de la vitesse radiale des nébuleuses extra-galactiques”. In: *Annales de la Société Scientifique de Bruxelles* 47 (Jan. 1, 1927). ADS Bibcode: 1927ASSB...47...49L, pp. 49–59. URL: <https://ui.adsabs.harvard.edu/abs/1927ASSB...47...49L> (visited on 02/18/2025).
- [23] A. Einstein. “Zur Elektrodynamik bewegter Körper”. In: *Annalen der Physik* 322.10 (Jan. 1905), pp. 891–921. ISSN: 0003-3804, 1521-3889. DOI: [10.1002/andp.19053221004](https://doi.org/10.1002/andp.19053221004). URL: <https://onlinelibrary.wiley.com/doi/10.1002/andp.19053221004> (visited on 01/02/2025).
- [24] R. Clausius. “Ueber einen auf die Wärme anwendbaren mechanischen Satz”. In: *Annalen der Physik* 217.9 (Jan. 1870), pp. 124–130. ISSN: 0003-3804, 1521-3889. DOI: [10.1002/andp.18702170911](https://doi.org/10.1002/andp.18702170911). URL: <https://gallica.bnf.fr/ark:/12148/bpt6k152258/f138.item> (visited on 12/27/2024).
- [25] F. Zwicky. “On the Masses of Nebulae and of Clusters of Nebulae”. In: *The Astrophysical Journal* 86 (Oct. 1937), p. 217. ISSN: 0004-637X, 1538-4357. DOI: [10.1086/143864](https://doi.org/10.1086/143864). URL: <http://adsabs.harvard.edu/doi/10.1086/143864> (visited on 12/30/2024).
- [26] Adam G. Riess et al. “A 2.4% DETERMINATION OF THE LOCAL VALUE OF THE HUBBLE CONSTANT\*”. In: *The Astrophysical Journal* 826.1 (July 20, 2016), p. 56. ISSN: 0004-637X, 1538-4357. DOI: [10.3847/0004-637X/826/1/56](https://doi.org/10.3847/0004-637X/826/1/56). URL: <https://iopscience.iop.org/article/10.3847/0004-637X/826/1/56> (visited on 12/30/2024).
- [27] Planck Collaboration et al. “Planck 2018 results: VI. Cosmological parameters”. In: *Astronomy & Astrophysics* 641 (Sept. 2020), A6. ISSN: 0004-6361, 1432-0746. DOI: [10.1051/0004-6361/201833910](https://doi.org/10.1051/0004-6361/201833910). URL: <https://www.aanda.org/10.1051/0004-6361/201833910> (visited on 01/26/2025).
- [28] Ewa L. Łokas and Gary A. Mamon. “Dark matter distribution in the Coma cluster from galaxy kinematics: breaking the mass–anisotropy degeneracy”. In: *Monthly Notices of the Royal Astronomical Society* 343.2 (Aug. 2003), pp. 401–412. ISSN: 0035-8711, 1365-2966. DOI: [10.1046/j.1365-8711.2003.06684.x](https://doi.org/10.1046/j.1365-8711.2003.06684.x). URL: <https://academic.oup.com/mnras/article/343/2/401/1038976> (visited on 12/30/2024).
- [29] Sinclair Smith. “The Mass of the Virgo Cluster”. In: *The Astrophysical Journal* 83 (Jan. 1936), p. 23. ISSN: 0004-637X, 1538-4357. DOI: [10.1086/143697](https://doi.org/10.1086/143697). URL: <http://adsabs.harvard.edu/doi/10.1086/143697> (visited on 12/31/2024).
- [30] Marisa Girardi et al. “Optical Mass Estimates of Galaxy Clusters”. In: *The Astrophysical Journal* 505.1 (Sept. 20, 1998), pp. 74–95. ISSN: 0004-637X, 1538-4357. DOI: [10.1086/306157](https://doi.org/10.1086/306157). URL: <https://iopscience.iop.org/article/10.1086/306157> (visited on 12/31/2024).

- [31] C. L. Sarazin. “The Intracluster Medium”. In: *Clusters and Superclusters of Galaxies*. Ed. by A. C. Fabian. Dordrecht: Springer Netherlands, 1992, pp. 131–150. ISBN: 978-94-010-5095-1. DOI: [10.1007/978-94-011-2482-9\\_9](https://doi.org/10.1007/978-94-011-2482-9_9). URL: [http://link.springer.com/10.1007/978-94-011-2482-9\\_9](http://link.springer.com/10.1007/978-94-011-2482-9_9) (visited on 02/01/2025).
- [32] O. Kotov and A. Vikhlinin. “Chandra Sample of Galaxy Clusters at  $z = 0.4$ – $0.55$ : Evolution in the Mass-Temperature Relation”. In: *The Astrophysical Journal* 641.2 (Apr. 20, 2006), pp. 752–755. ISSN: 0004-637X, 1538-4357. DOI: [10.1086/500553](https://doi.org/10.1086/500553). URL: <https://iopscience.iop.org/article/10.1086/500553> (visited on 02/01/2025).
- [33] A. Einstein. “Die Grundlage der allgemeinen Relativitätstheorie”. In: *Annalen der Physik* 354.7 (Jan. 1916), pp. 769–822. ISSN: 0003-3804, 1521-3889. DOI: [10.1002/andp.19163540702](https://doi.org/10.1002/andp.19163540702). URL: <https://onlinelibrary.wiley.com/doi/10.1002/andp.19163540702> (visited on 01/07/2025).
- [34] H. A. Lorentz, A. Einstein, and H. Minkowski. *Das Relativitätsprinzip: Eine Sammlung von Abhandlungen*. 4th ed. 1922. Fortschritte der mathematischen Wissenschaften in Monographien. Wiesbaden: Vieweg+Teubner Verlag, 1922. 121-123. ISBN: 978-3-663-16170-7. DOI: [10.1007/978-3-663-16170-7](https://doi.org/10.1007/978-3-663-16170-7).
- [35] Albert Einstein, Alfred Engel, and Engelbert Schucking. *The collected papers of Albert Einstein: writings, 1914-1917*. English translation of selected texts. Princeton: Princeton university press, 1997. ISBN: 978-0-691-01734-1. URL: <https://einsteinpapers.press.princeton.edu/vol6-trans/> (visited on 01/07/2025).
- [36] Massimo Meneghetti. *Introduction to Gravitational Lensing: With Python Examples*. Vol. 956. Lecture Notes in Physics. Cham: Springer International Publishing, 2021. ISBN: 978-3-030-73581-4. DOI: [10.1007/978-3-030-73582-1](https://doi.org/10.1007/978-3-030-73582-1). URL: <https://link.springer.com/10.1007/978-3-030-73582-1> (visited on 02/18/2025).
- [37] Richard Massey, Thomas Kitching, and Johan Richard. “The dark matter of gravitational lensing”. In: *Reports on Progress in Physics* 73.8 (Aug. 1, 2010), p. 086901. ISSN: 0034-4885, 1361-6633. DOI: [10.1088/0034-4885/73/8/086901](https://doi.org/10.1088/0034-4885/73/8/086901). URL: <https://iopscience.iop.org/article/10.1088/0034-4885/73/8/086901> (visited on 01/08/2025).
- [38] NASA. *1E 0657-56: NASA Finds Direct Proof of Dark Matter*. Aug. 21, 2006. URL: <https://chandra.harvard.edu/photo/2006/1e0657/index.html> (visited on 10/01/2025).
- [39] NASA. *MACS J0025.4-1222: A Clash of Clusters Provides Another Clue to Dark Matter*. Aug. 27, 2008. URL: <https://chandra.harvard.edu/photo/2008/macs/> (visited on 01/13/2025).
- [40] Douglas Clowe et al. “A Direct Empirical Proof of the Existence of Dark Matter”. In: *The Astrophysical Journal* 648.2 (Sept. 10, 2006), pp. L109–L113. ISSN: 0004-637X, 1538-4357. DOI: [10.1086/508162](https://doi.org/10.1086/508162). URL: <https://iopscience.iop.org/article/10.1086/508162> (visited on 01/10/2025).
- [41] M. J. Jee et al. “Hubble Space Telescope Advanced Camera for Surveys Weak-Lensing and Chandra X-Ray Studies of the High-Redshift Cluster MS 1054–0321”. In: *The Astrophysical Journal* 634.2 (Dec. 2005), pp. 813–832. ISSN: 0004-637X, 1538-4357. DOI: [10.1086/497001](https://doi.org/10.1086/497001). URL: <https://iopscience.iop.org/article/10.1086/497001> (visited on 01/10/2025).

- [42] Maruša Bradač et al. “Revealing the Properties of Dark Matter in the Merging Cluster MACS J0025.4–1222”. In: *The Astrophysical Journal* 687.2 (Nov. 10, 2008), pp. 959–967. ISSN: 0004-637X, 1538-4357. DOI: [10.1086/591246](https://doi.org/10.1086/591246). URL: <https://iopscience.iop.org/article/10.1086/591246> (visited on 01/10/2025).
- [43] Andisheh Mahdavi et al. “A Dark Core in Abell 520”. In: *The Astrophysical Journal* 668.2 (Oct. 20, 2007), pp. 806–814. ISSN: 0004-637X, 1538-4357. DOI: [10.1086/521383](https://doi.org/10.1086/521383). URL: <https://iopscience.iop.org/article/10.1086/521383> (visited on 01/10/2025).
- [44] G. Hinshaw et al. “FIVE-YEAR WILKINSON MICROWAVE ANISOTROPY PROBE OBSERVATIONS: DATA PROCESSING, SKY MAPS, AND BASIC RESULTS”. In: *The Astrophysical Journal Supplement Series* 180.2 (Feb. 1, 2009), pp. 225–245. ISSN: 0067-0049, 1538-4365. DOI: [10.1088/0067-0049/180/2/225](https://doi.org/10.1088/0067-0049/180/2/225). URL: <https://iopscience.iop.org/article/10.1088/0067-0049/180/2/225> (visited on 01/27/2025).
- [45] D. J. Fixsen. “THE TEMPERATURE OF THE COSMIC MICROWAVE BACKGROUND”. In: *The Astrophysical Journal* 707.2 (Dec. 20, 2009), pp. 916–920. ISSN: 0004-637X, 1538-4357. DOI: [10.1088/0004-637X/707/2/916](https://doi.org/10.1088/0004-637X/707/2/916). URL: <https://iopscience.iop.org/article/10.1088/0004-637X/707/2/916> (visited on 01/26/2025).
- [46] A. A. Penzias and R. W. Wilson. “A Measurement of Excess Antenna Temperature at 4080 Mc/s.” In: *The Astrophysical Journal* 142 (July 1965), p. 419. ISSN: 0004-637X, 1538-4357. DOI: [10.1086/148307](https://doi.org/10.1086/148307). URL: <http://adsabs.harvard.edu/doi/10.1086/148307> (visited on 01/26/2025).
- [47] R. H. Dicke et al. “Cosmic Black-Body Radiation.” In: *The Astrophysical Journal* 142 (July 1, 1965). Publisher: IOP ADS Bibcode: 1965ApJ...142..414D, pp. 414–419. ISSN: 0004-637X. DOI: [10.1086/148306](https://doi.org/10.1086/148306). URL: <https://ui.adsabs.harvard.edu/abs/1965ApJ...142..414D> (visited on 01/26/2025).
- [48] Shaul Hanany, Michael D. Niemack, and Lyman Page. “CMB Telescopes and Optical Systems”. In: *Planets, Stars and Stellar Systems*. Ed. by Terry D. Oswalt and Ian S. McLean. Dordrecht: Springer Netherlands, 2013, pp. 431–480. ISBN: 978-94-007-5620-5. DOI: [10.1007/978-94-007-5621-2\\_10](https://doi.org/10.1007/978-94-007-5621-2_10). URL: [http://link.springer.com/10.1007/978-94-007-5621-2\\_10](http://link.springer.com/10.1007/978-94-007-5621-2_10) (visited on 01/26/2025).
- [49] Planck Collaboration et al. “Planck 2018 results: IV. Diffuse component separation”. In: *Astronomy & Astrophysics* 641 (Sept. 2020), A4. ISSN: 0004-6361, 1432-0746. DOI: [10.1051/0004-6361/201833881](https://doi.org/10.1051/0004-6361/201833881). URL: <https://www.aanda.org/10.1051/0004-6361/201833881> (visited on 01/26/2025).
- [50] Planck Collaboration. *2018 CMB maps - Planck Legacy Archive Wiki*. URL: [https://wiki.cosmos.esa.int/planck-legacy-archive/index.php/CMB\\_maps](https://wiki.cosmos.esa.int/planck-legacy-archive/index.php/CMB_maps) (visited on 01/26/2025).
- [51] A. Del Popolo. “Dark matter, density perturbations, and structure formation”. In: *Astronomy Reports* 51.3 (Mar. 2007), pp. 169–196. ISSN: 1063-7729, 1562-6881. DOI: [10.1134/S1063772907030018](https://doi.org/10.1134/S1063772907030018). URL: <http://link.springer.com/10.1134/S1063772907030018> (visited on 02/01/2025).

- [52] Volker Springel et al. “Simulations of the formation, evolution and clustering of galaxies and quasars”. In: *Nature* 435.7042 (June 2005), pp. 629–636. ISSN: 0028-0836, 1476-4687. DOI: [10.1038/nature03597](https://doi.org/10.1038/nature03597). URL: <https://www.nature.com/articles/nature03597> (visited on 02/01/2025).
- [53] M. Milgrom. “A modification of the Newtonian dynamics as a possible alternative to the hidden mass hypothesis”. In: *The Astrophysical Journal* 270 (July 1983), p. 365. ISSN: 0004-637X, 1538-4357. DOI: [10.1086/161130](https://doi.org/10.1086/161130). URL: <http://adsabs.harvard.edu/doi/10.1086/161130> (visited on 01/14/2025).
- [54] Jacob D. Bekenstein. “Relativistic gravitation theory for the modified Newtonian dynamics paradigm”. In: *Physical Review D* 70.8 (Oct. 13, 2004), p. 083509. ISSN: 1550-7998, 1550-2368. DOI: [10.1103/PhysRevD.70.083509](https://doi.org/10.1103/PhysRevD.70.083509). URL: <https://link.aps.org/doi/10.1103/PhysRevD.70.083509> (visited on 01/14/2025).
- [55] Theodorus Maria Nieuwenhuizen. “How Zwicky already ruled out modified gravity theories without dark matter”. In: *Fortschritte der Physik* 65.6 (June 2017), p. 1600050. ISSN: 0015-8208, 1521-3978. DOI: [10.1002/prop.201600050](https://doi.org/10.1002/prop.201600050). URL: <https://onlinelibrary.wiley.com/doi/10.1002/prop.201600050> (visited on 02/01/2025).
- [56] G. W. Angus, B. Famaey, and D. A. Buote. “X-ray group and cluster mass profiles in MOND: unexplained mass on the group scale”. In: *Monthly Notices of the Royal Astronomical Society* 387.4 (July 11, 2008), pp. 1470–1480. ISSN: 00358711, 13652966. DOI: [10.1111/j.1365-2966.2008.13353.x](https://doi.org/10.1111/j.1365-2966.2008.13353.x). URL: <https://academic.oup.com/mnras/article-lookup/doi/10.1111/j.1365-2966.2008.13353.x> (visited on 02/01/2025).
- [57] Judith A. Irwin, Lawrence M. Widrow, and Jayanne English. “An Observational Test of Dark Matter as Cold Fractal Clouds”. In: *The Astrophysical Journal* 529.1 (Jan. 20, 2000), pp. 77–87. ISSN: 0004-637X, 1538-4357. DOI: [10.1086/308267](https://doi.org/10.1086/308267). URL: <https://iopscience.iop.org/article/10.1086/308267> (visited on 02/01/2025).
- [58] P. Tisserand et al. “Limits on the Macho content of the Galactic Halo from the EROS-2 Survey of the Magellanic Clouds”. In: *Astronomy & Astrophysics* 469.2 (July 2007), pp. 387–404. ISSN: 0004-6361, 1432-0746. DOI: [10.1051/0004-6361:20066017](https://doi.org/10.1051/0004-6361:20066017). URL: <http://www.aanda.org/10.1051/0004-6361:20066017> (visited on 02/01/2025).
- [59] C. Alcock et al. “The MACHO Project: Microlensing Results from 5.7 Years of Large Magellanic Cloud Observations”. In: *The Astrophysical Journal* 542.1 (Oct. 10, 2000), pp. 281–307. ISSN: 0004-637X, 1538-4357. DOI: [10.1086/309512](https://doi.org/10.1086/309512). URL: <https://iopscience.iop.org/article/10.1086/309512> (visited on 02/01/2025).
- [60] Brian D. Fields and Keith A. Olive. “Big bang nucleosynthesis”. In: *Nuclear Physics A* 777 (Oct. 2006), pp. 208–225. ISSN: 03759474. DOI: [10.1016/j.nuclphysa.2004.10.033](https://doi.org/10.1016/j.nuclphysa.2004.10.033). URL: <https://linkinghub.elsevier.com/retrieve/pii/S0375947404011479> (visited on 02/01/2025).
- [61] Karsten Jedamzik and Maxim Pospelov. “Big Bang nucleosynthesis and particle dark matter”. In: *New Journal of Physics* 11.10 (Oct. 16, 2009), p. 105028. ISSN: 1367-2630. DOI: [10.1088/1367-2630/11/10/105028](https://doi.org/10.1088/1367-2630/11/10/105028). URL: <https://iopscience.iop.org/article/10.1088/1367-2630/11/10/105028> (visited on 02/01/2025).

- [62] L. Bergström. “Non-baryonic dark matter”. In: *Nuclear Physics B - Proceedings Supplements* 70.1 (Jan. 1999), pp. 31–42. ISSN: 09205632. DOI: [10.1016/S0920-5632\(98\)00385-5](https://doi.org/10.1016/S0920-5632(98)00385-5). URL: <https://linkinghub.elsevier.com/retrieve/pii/S0920563298003855> (visited on 02/01/2025).
- [63] S. Navas et al. “Review of Particle Physics”. In: *Physical Review D* 110.3 (Aug. 1, 2024), p. 030001. ISSN: 2470-0010, 2470-0029. DOI: [10.1103/PhysRevD.110.030001](https://doi.org/10.1103/PhysRevD.110.030001). URL: <https://link.aps.org/doi/10.1103/PhysRevD.110.030001> (visited on 02/02/2025).
- [64] Scott Tremaine and James E. Gunn. “Dynamical Role of Light Neutral Leptons in Cosmology”. In: *Physical Review Letters* 42.6 (Feb. 5, 1979), pp. 407–410. ISSN: 0031-9007. DOI: [10.1103/PhysRevLett.42.407](https://doi.org/10.1103/PhysRevLett.42.407). URL: <https://link.aps.org/doi/10.1103/PhysRevLett.42.407> (visited on 02/02/2025).
- [65] Joel R. Primack and Michael A. K. Gross. “Hot Dark Matter in Cosmology”. In: *Current Aspects of Neutrino Physics*. Ed. by David O. Caldwell. Berlin, Heidelberg: Springer Berlin Heidelberg, 2001, pp. 287–308. ISBN: 978-3-642-07424-0. DOI: [10.1007/978-3-662-04597-8\\_12](https://doi.org/10.1007/978-3-662-04597-8_12). URL: [https://link.springer.com/10.1007/978-3-662-04597-8\\_12](https://link.springer.com/10.1007/978-3-662-04597-8_12) (visited on 02/02/2025).
- [66] T. Yanagida. “Horizontal Symmetry and Masses of Neutrinos”. In: *Progress of Theoretical Physics* 64.3 (Sept. 1, 1980), pp. 1103–1105. ISSN: 0033-068X, 1347-4081. DOI: [10.1143/PTP.64.1103](https://doi.org/10.1143/PTP.64.1103). URL: <https://academic.oup.com/ptp/article-lookup/doi/10.1143/PTP.64.1103> (visited on 02/18/2025).
- [67] A. Boyarsky et al. “Sterile neutrino Dark Matter”. In: *Progress in Particle and Nuclear Physics* 104 (Jan. 2019), pp. 1–45. ISSN: 01466410. DOI: [10.1016/j.ppnp.2018.07.004](https://doi.org/10.1016/j.ppnp.2018.07.004). URL: <https://linkinghub.elsevier.com/retrieve/pii/S0146641018300711> (visited on 02/02/2025).
- [68] Leszek Roszkowski, Enrico Maria Sessolo, and Sebastian Trojanowski. “WIMP dark matter candidates and searches—current status and future prospects”. In: *Reports on Progress in Physics* 81.6 (June 1, 2018), p. 066201. ISSN: 0034-4885, 1361-6633. DOI: [10.1088/1361-6633/aab913](https://doi.org/10.1088/1361-6633/aab913). URL: <https://iopscience.iop.org/article/10.1088/1361-6633/aab913> (visited on 02/10/2025).
- [69] Gerard Jungman, Marc Kamionkowski, and Kim Griest. “Supersymmetric dark matter”. In: *Physics Reports* 267.5 (Mar. 1996), pp. 195–373. ISSN: 03701573. DOI: [10.1016/0370-1573\(95\)00058-5](https://doi.org/10.1016/0370-1573(95)00058-5). URL: <https://linkinghub.elsevier.com/retrieve/pii/0370157395000585> (visited on 02/10/2025).
- [70] Dan Hooper and Stefano Profumo. “Dark matter and collider phenomenology of universal extra dimensions”. In: *Physics Reports* 453.2 (Dec. 2007), pp. 29–115. ISSN: 03701573. DOI: [10.1016/j.physrep.2007.09.003](https://doi.org/10.1016/j.physrep.2007.09.003). URL: <https://linkinghub.elsevier.com/retrieve/pii/S0370157307003493> (visited on 02/10/2025).
- [71] Hsin-Chia Cheng and Ian Low. “Little Hierarchy, Little Higgses, and a Little Symmetry”. In: *Journal of High Energy Physics* 2004.8 (Sept. 1, 2004), pp. 061–061. ISSN: 1029-8479. DOI: [10.1088/1126-6708/2004/08/061](https://doi.org/10.1088/1126-6708/2004/08/061). URL: <http://stacks.iop.org/1126-6708/2004/i=08/a=061?key=crossref.03790284936a6407ba700efb1fb3e083> (visited on 02/09/2025).

- [72] V. Fanti et al. “A new measurement of direct CP violation in two pion decays of the neutral kaon”. In: *Physics Letters B* 465.1 (Oct. 1999), pp. 335–348. ISSN: 03702693. DOI: [10.1016/S0370-2693\(99\)01030-8](https://doi.org/10.1016/S0370-2693(99)01030-8). URL: <https://linkinghub.elsevier.com/retrieve/pii/S0370269399010308> (visited on 02/02/2025).
- [73] K. Abe et al. “Observation of Large CP Violation in the Neutral B Meson System”. In: *Physical Review Letters* 87.9 (Aug. 14, 2001), p. 091802. ISSN: 0031-9007, 1079-7114. DOI: [10.1103/PhysRevLett.87.091802](https://doi.org/10.1103/PhysRevLett.87.091802). URL: <https://link.aps.org/doi/10.1103/PhysRevLett.87.091802> (visited on 02/02/2025).
- [74] C. Abel et al. “Measurement of the Permanent Electric Dipole Moment of the Neutron”. In: *Physical Review Letters* 124.8 (Feb. 28, 2020), p. 081803. ISSN: 0031-9007, 1079-7114. DOI: [10.1103/PhysRevLett.124.081803](https://doi.org/10.1103/PhysRevLett.124.081803). URL: <https://link.aps.org/doi/10.1103/PhysRevLett.124.081803> (visited on 02/02/2025).
- [75] R. D. Peccei and Helen R. Quinn. “CP Conservation in the Presence of Pseudoparticles”. In: *Physical Review Letters* 38.25 (June 20, 1977), pp. 1440–1443. ISSN: 0031-9007. DOI: [10.1103/PhysRevLett.38.1440](https://doi.org/10.1103/PhysRevLett.38.1440). URL: <https://link.aps.org/doi/10.1103/PhysRevLett.38.1440> (visited on 02/02/2025).
- [76] F. Wilczek. “Problem of Strong P and T Invariance in the Presence of Instantons”. In: *Physical Review Letters* 40.5 (Jan. 30, 1978), pp. 279–282. ISSN: 0031-9007. DOI: [10.1103/PhysRevLett.40.279](https://doi.org/10.1103/PhysRevLett.40.279). URL: <https://link.aps.org/doi/10.1103/PhysRevLett.40.279> (visited on 02/02/2025).
- [77] Steven Weinberg. “A New Light Boson?” In: *Physical Review Letters* 40.4 (Jan. 23, 1978), pp. 223–226. ISSN: 0031-9007. DOI: [10.1103/PhysRevLett.40.223](https://doi.org/10.1103/PhysRevLett.40.223). URL: <https://link.aps.org/doi/10.1103/PhysRevLett.40.223> (visited on 02/02/2025).
- [78] David J.E. Marsh. “Axion cosmology”. In: *Physics Reports* 643 (July 2016), pp. 1–79. ISSN: 03701573. DOI: [10.1016/j.physrep.2016.06.005](https://doi.org/10.1016/j.physrep.2016.06.005). URL: <https://linkinghub.elsevier.com/retrieve/pii/S0370157316301557> (visited on 02/02/2025).
- [79] Andriy Kurylov and Marc Kamionkowski. “Generalized analysis of the direct weakly interacting massive particle searches”. In: *Physical Review D* 69.6 (Mar. 10, 2004), p. 063503. ISSN: 1550-7998, 1550-2368. DOI: [10.1103/PhysRevD.69.063503](https://doi.org/10.1103/PhysRevD.69.063503). URL: <https://link.aps.org/doi/10.1103/PhysRevD.69.063503> (visited on 02/09/2025).
- [80] V. A. Bednyakov. “Aspects of spin-dependent dark matter search”. In: *Physics of Atomic Nuclei* 67.11 (Nov. 2004), pp. 1931–1941. ISSN: 1063-7788, 1562-692X. DOI: [10.1134/1.1825508](https://doi.org/10.1134/1.1825508). URL: <http://link.springer.com/10.1134/1.1825508> (visited on 02/18/2025).
- [81] D Carney et al. “Mechanical quantum sensing in the search for dark matter”. In: *Quantum Science and Technology* 6.2 (Apr. 1, 2021), p. 024002. ISSN: 2058-9565. DOI: [10.1088/2058-9565/abcfd](https://doi.org/10.1088/2058-9565/abcfd). URL: <https://iopscience.iop.org/article/10.1088/2058-9565/abcfd> (visited on 02/03/2025).

- [82] M.G. Aartsen et al. “The IceCube Neutrino Observatory: instrumentation and online systems”. In: *Journal of Instrumentation* 12.3 (Mar. 14, 2017), P03012–P03012. ISSN: 1748-0221. DOI: [10.1088/1748-0221/12/03/P03012](https://doi.org/10.1088/1748-0221/12/03/P03012). URL: <https://iopscience.iop.org/article/10.1088/1748-0221/12/03/P03012> (visited on 02/18/2025).
- [83] Tomio Kobayashi. “Experimental verification of the standard model of particle physics”. In: *Proceedings of the Japan Academy, Series B* 97.5 (May 11, 2021), pp. 211–235. ISSN: 0386-2208, 1349-2896. DOI: [10.2183/pjab.97.013](https://doi.org/10.2183/pjab.97.013). URL: [https://www.jstage.jst.go.jp/article/pjab/97/5/97\\_PJA9705B-01/\\_article](https://www.jstage.jst.go.jp/article/pjab/97/5/97_PJA9705B-01/_article) (visited on 02/18/2025).
- [84] R. Bernabei et al. “Annual modulation results from DAMA/LIBRA”. In: *International Journal of Modern Physics: Conference Series* 51 (Jan. 2023), p. 2361008. ISSN: 2010-1945. DOI: [10.1142/S2010194523610086](https://doi.org/10.1142/S2010194523610086). URL: <https://www.worldscientific.com/doi/10.1142/S2010194523610086> (visited on 02/18/2025).
- [85] G. Angloher et al. “Deep-underground dark matter search with a COSINUS detector prototype”. In: *Physical Review D* 110.4 (Aug. 5, 2024), p. 043010. ISSN: 2470-0010, 2470-0029. DOI: [10.1103/PhysRevD.110.043010](https://doi.org/10.1103/PhysRevD.110.043010). URL: <https://link.aps.org/doi/10.1103/PhysRevD.110.043010> (visited on 02/18/2025).
- [86] M. Kaznacheeva and K. Schäffner. “Scintillating low-temperature calorimeters for direct dark matter search”. In: *Journal of Advanced Instrumentation in Science* 2024.1 (2024). DOI: [10.31526/jais.2024.514](https://doi.org/10.31526/jais.2024.514). URL: <https://jais.andromedapublisher.org/index.php/JAIS/article/download/514/252> (visited on 02/09/2025).
- [87] Lino Miramonti. “European underground laboratories: An overview”. In: *AIP Conference Proceedings*. TOPICAL WORKSHOP ON LOW RADIOACTIVITY TECHNIQUES: LRT 2004. Vol. 785. ISSN: 0094243X. Sudbury, Ontario (Canada): AIP, 2005, pp. 3–11. DOI: [10.1063/1.2060447](https://doi.org/10.1063/1.2060447). URL: <https://pubs.aip.org/aip/acp/article/785/1/3-11/947115> (visited on 01/30/2025).
- [88] Klemens Rottler. “Muons in the CRESST Dark Matter Experiment”. PhD thesis. U. Tübingen, 2014. URL: <http://hdl.handle.net/10900/53055>.
- [89] CRESST experiment. *The CRESST Facility | CRESST*. URL: <https://cresst-experiment.org/the-cresst-experiment/the-cresst-facility> (visited on 02/02/2025).
- [90] Marco Selvi. “Analysis of the seasonal modulation of the cosmic muon flux in the LVD detector during 2001-2008.” In: *Proceedings of the 31st International Cosmic Ray Conference*. Vol. 2. Lodz, Poland, 2009, pp. 1043–1047. URL: <https://galprop.stanford.edu/elibrary/icrc/2009/preliminary/pdf/icrc0766.pdf>.
- [91] Francesca Pucci. “Optimisation of Transition Edge Sensors and Development of Novel Detector Designs to Enhance CRESST Dark Matter Sensitivity”. PhD thesis. Technische Universität München, 2024. 178 pp. URL: <https://mediatum.ub.tum.de/1747757>.
- [92] S. Di Lorenzo. “Multiple detector analysis in the CRESST dark matter experiment.” PhD thesis. GSSI, L’Aquila, Italy, 2020. URL: <https://iris.gssi.it/handle/20.500.12571/15361> (visited on 02/12/2025).

- [93] G. Angloher et al. “Commissioning run of the CRESST-II dark matter search”. In: *Astroparticle Physics* 31.4 (May 2009), pp. 270–276. ISSN: 09276505. DOI: [10.1016/j.astropartphys.2009.02.007](https://doi.org/10.1016/j.astropartphys.2009.02.007). URL: <https://linkinghub.elsevier.com/retrieve/pii/S0927650509000358> (visited on 02/10/2025).
- [94] S Henry et al. “The 66-channel SQUID readout for CRESST II”. In: *Journal of Instrumentation* 2.11 (Nov. 12, 2007), P11003–P11003. ISSN: 1748-0221. DOI: [10.1088/1748-0221/2/11/P11003](https://doi.org/10.1088/1748-0221/2/11/P11003). URL: <https://iopscience.iop.org/article/10.1088/1748-0221/2/11/P11003> (visited on 02/10/2025).
- [95] M Sisti et al. “The CRESST dark matter experiment: status and perspectives”. In: *Nuclear Instruments and Methods in Physics Research Section A: Accelerators, Spectrometers, Detectors and Associated Equipment* 444.1 (Apr. 2000), pp. 312–314. ISSN: 01689002. DOI: [10.1016/S0168-9002\(99\)01405-9](https://doi.org/10.1016/S0168-9002(99)01405-9). URL: <https://linkinghub.elsevier.com/retrieve/pii/S0168900299014059> (visited on 02/10/2025).
- [96] F Petricca et al. “First results on low-mass dark matter from the CRESST-III experiment”. In: *Journal of Physics: Conference Series* 1342.1 (Jan. 1, 2020), p. 012076. ISSN: 1742-6588, 1742-6596. DOI: [10.1088/1742-6596/1342/1/012076](https://doi.org/10.1088/1742-6596/1342/1/012076). URL: <https://iopscience.iop.org/article/10.1088/1742-6596/1342/1/012076> (visited on 02/10/2025).
- [97] R. Strauss et al. “A prototype detector for the CRESST-III low-mass dark matter search”. In: *Nuclear Instruments and Methods in Physics Research Section A: Accelerators, Spectrometers, Detectors and Associated Equipment* 845 (Feb. 2017), pp. 414–417. ISSN: 01689002. DOI: [10.1016/j.nima.2016.06.060](https://doi.org/10.1016/j.nima.2016.06.060). URL: <https://linkinghub.elsevier.com/retrieve/pii/S0168900216306039> (visited on 02/11/2025).
- [98] A. H. Abdelhameed et al. “First results from the CRESST-III low-mass dark matter program”. In: *Physical Review D* 100.10 (Nov. 25, 2019), p. 102002. ISSN: 2470-0010, 2470-0029. DOI: [10.1103/PhysRevD.100.102002](https://doi.org/10.1103/PhysRevD.100.102002). URL: <https://link.aps.org/doi/10.1103/PhysRevD.100.102002> (visited on 02/11/2025).
- [99] Angelina Carina Kinast. “Enhancing the Dark Matter Sensitivity of CRESST: Purification, Stress Reduction and <sup>17</sup>O Enrichment of CaWO<sub>4</sub> Target Crystals”. PhD thesis. Technische Universität München, 2023. 254 pp. URL: <https://mediatum.ub.tum.de/1726057>.
- [100] P. Debye. “Zur Theorie der spezifischen Wärmen”. In: *Annalen der Physik* 344.14 (Jan. 1912), pp. 789–839. ISSN: 0003-3804, 1521-3889. DOI: [10.1002/andp.19123441404](https://doi.org/10.1002/andp.19123441404). URL: <https://onlinelibrary.wiley.com/doi/10.1002/andp.19123441404> (visited on 02/23/2025).
- [101] J. Bardeen, L. N. Cooper, and J. R. Schrieffer. “Theory of Superconductivity”. In: *Physical Review* 108.5 (Dec. 1, 1957), pp. 1175–1204. ISSN: 0031-899X. DOI: [10.1103/PhysRev.108.1175](https://doi.org/10.1103/PhysRev.108.1175). URL: <https://link.aps.org/doi/10.1103/PhysRev.108.1175> (visited on 02/13/2025).
- [102] Alexander Klaus Herbert Langenkämper. “Characterisation of the Muon-Induced Neutron Background with a LiF Cryogenic Detector”. PhD thesis. Technische Universität München, 2023. 178 pp. URL: <https://mediatum.ub.tum.de/1709909>.

- [103] W. Meissner and R. Ochsenfeld. “Ein neuer Effekt bei Eintritt der Supraleitfähigkeit”. In: *Die Naturwissenschaften* 21.44 (Nov. 1933), pp. 787–788. ISSN: 0028-1042, 1432-1904. DOI: [10.1007/BF01504252](https://doi.org/10.1007/BF01504252). URL: <http://link.springer.com/10.1007/BF01504252> (visited on 02/23/2025).
- [104] E. M. Lifshitz et al. *Statistical physics*. 2nd ed. rev. and enl. Course of theoretical physics 9. Oxford: Pergamon press, 1980. ISBN: 978-0-08-023073-3.
- [105] Waldemar Nawrocki. “SQUID Detectors of Magnetic Flux”. In: *Introduction to Quantum Metrology*. Cham: Springer International Publishing, 2019, pp. 119–162. ISBN: 978-3-030-19676-9. DOI: [10.1007/978-3-030-19677-6\\_5](https://doi.org/10.1007/978-3-030-19677-6_5). URL: [http://link.springer.com/10.1007/978-3-030-19677-6\\_5](http://link.springer.com/10.1007/978-3-030-19677-6_5) (visited on 02/14/2025).
- [106] John Clarke and Alex I. Braginski, eds. *The SQUID Handbook: Fundamentals and Technology of SQUIDs and SQUID Systems*. 1st ed. Wiley, May 26, 2004. ISBN: 978-3-527-40229-8. DOI: [10.1002/3527603646](https://doi.org/10.1002/3527603646). URL: <https://onlinelibrary.wiley.com/doi/book/10.1002/3527603646> (visited on 02/14/2025).
- [107] Samuel Austin Henry. “The 66-channel readout for the CRESST dark matter search”. PhD thesis. University of Oxford, 2003. URL: [https://twiki.cern.ch/twiki/pub/CRESST/PhDTheses/Oxford\\_2003\\_S.\\_Henry\\_-\\_The\\_66-channel\\_readout\\_for\\_the\\_CRESST\\_dark\\_matter\\_search.pdf](https://twiki.cern.ch/twiki/pub/CRESST/PhDTheses/Oxford_2003_S._Henry_-_The_66-channel_readout_for_the_CRESST_dark_matter_search.pdf).
- [108] Nahuel Ferreiro Iachellini. “Increasing the sensitivity to low mass dark matter in CRESST-III with a new DAQ and signal processing”. Medium: application/pdf. PhD thesis. Ludwig-Maximilians-Universität München, 2019. DOI: [10.5282/EDOC.23762](https://doi.org/10.5282/EDOC.23762). URL: <https://edoc.ub.uni-muenchen.de/id/eprint/23762> (visited on 02/19/2025).
- [109] Michael F. L’Annunziata. *Handbook of Radioactivity Analysis*. 4th ed. Vol. 1. Elsevier, 2020. ISBN: 978-0-12-814397-1. DOI: [10.1016/C2016-0-04811-8](https://doi.org/10.1016/C2016-0-04811-8). URL: <https://linkinghub.elsevier.com/retrieve/pii/C20160048118> (visited on 02/24/2025).
- [110] G. Angloher et al. “Secular equilibrium assessment in a CaWO<sub>4</sub> target crystal from the dark matter experiment CRESST using Bayesian likelihood normalisation”. In: *Applied Radiation and Isotopes* 194 (Apr. 2023), p. 110670. ISSN: 09698043. DOI: [10.1016/j.apradiso.2023.110670](https://doi.org/10.1016/j.apradiso.2023.110670). URL: <https://linkinghub.elsevier.com/retrieve/pii/S0969804323000234> (visited on 02/23/2025).
- [111] M Bühler et al. “Status and low background considerations for the CRESST dark matter search”. In: *Nuclear Instruments and Methods in Physics Research Section A: Accelerators, Spectrometers, Detectors and Associated Equipment* 370.1 (Feb. 1996), pp. 237–240. ISSN: 01689002. DOI: [10.1016/0168-9002\(95\)01095-5](https://doi.org/10.1016/0168-9002(95)01095-5). URL: <https://linkinghub.elsevier.com/retrieve/pii/0168900295010955> (visited on 02/21/2025).
- [112] A. Fuss and et al et. “EXCESS workshop: Descriptions of rising low-energy spectra”. In: Fermi National Accelerator Lab. (FNAL), Batavia, IL (United States); SLAC National Accelerator Lab., Menlo Park, CA (United States); Pacific Northwest National Lab. (PNNL), Richland, WA (United States), Feb. 2022. URL: <https://www.osti.gov/biblio/1862233>.

- [113] G. Angloher et al. “Detector Development for the CRESST Experiment”. In: *Journal of Low Temperature Physics* 216.1 (July 2024), pp. 393–401. ISSN: 0022-2291, 1573-7357. DOI: [10.1007/s10909-024-03154-6](https://doi.org/10.1007/s10909-024-03154-6). URL: <https://link.springer.com/10.1007/s10909-024-03154-6> (visited on 02/21/2025).
- [114] A. H. Abdelhameed et al. “Geant4-based electromagnetic background model for the CRESST dark matter experiment”. In: *The European Physical Journal C* 79.10 (Oct. 2019), p. 881. ISSN: 1434-6044, 1434-6052. DOI: [10.1140/epjc/s10052-019-7385-0](https://doi.org/10.1140/epjc/s10052-019-7385-0). URL: <http://link.springer.com/10.1140/epjc/s10052-019-7385-0> (visited on 02/22/2025).
- [115] Jens Burkhart. “Enhancing the Electromagnetic Background Model of CRESST-II”. In: (2022). In collab. with Jochen Schieck and Florian Reindl. Artwork Size: 101 pages Medium: application/pdf Publisher: TU Wien, 101 pages. DOI: [10.34726/HSS.2022.104928](https://doi.org/10.34726/HSS.2022.104928). URL: <https://repositum.tuwien.at/handle/20.500.12708/81297> (visited on 02/21/2025).
- [116] G. Angloher et al. “High-dimensional Bayesian likelihood normalisation for CRESST’s background model”. In: *Journal of Instrumentation* 19.11 (Nov. 1, 2024), P11013. ISSN: 1748-0221. DOI: [10.1088/1748-0221/19/11/P11013](https://doi.org/10.1088/1748-0221/19/11/P11013). URL: <https://iopscience.iop.org/article/10.1088/1748-0221/19/11/P11013> (visited on 02/22/2025).
- [117] Philipp Martin Michael Bauer. “Data Analysis for the CRESST Experiment: New Methods, improved Alpha Analysis, and Results on Light Dark Matter and Backgrounds”. PhD thesis. Munich, Tech. U., 2020. URL: <https://publications.mppmu.mpg.de/?action=search&language=en&mpi=MPP-2020-270>.
- [118] E. Gatti and P. F. Manfredi. “Processing the signals from solid-state detectors in elementary-particle physics”. In: *La Rivista del Nuovo Cimento* 9.1 (Jan. 1986), pp. 1–146. ISSN: 1826-9850. DOI: [10.1007/BF02822156](https://doi.org/10.1007/BF02822156). URL: <http://link.springer.com/10.1007/BF02822156> (visited on 03/03/2025).
- [119] M. Mancuso et al. “A method to define the energy threshold depending on noise level for rare event searches”. In: *Nuclear Instruments and Methods in Physics Research Section A: Accelerators, Spectrometers, Detectors and Associated Equipment* 940 (Oct. 2019), pp. 492–496. ISSN: 01689002. DOI: [10.1016/j.nima.2019.06.030](https://doi.org/10.1016/j.nima.2019.06.030). URL: <https://linkinghub.elsevier.com/retrieve/pii/S0168900219308708> (visited on 03/04/2025).
- [120] Felix Wagner. “Towards next-generation cryogenic dark matter searches with superconducting thermometers”. Artwork Size: 238 pages Medium: application/pdf Pages: 238 pages. PhD thesis. TU Wien, 2023. DOI: [10.34726/HSS.2023.106550](https://doi.org/10.34726/HSS.2023.106550). URL: <https://repositum.tuwien.at/handle/20.500.12708/190804> (visited on 03/05/2025).
- [121] F. Pröbst et al. “Model for cryogenic particle detectors with superconducting phase transition thermometers”. In: *Journal of Low Temperature Physics* 100.1 (July 1995), pp. 69–104. ISSN: 0022-2291, 1573-7357. DOI: [10.1007/BF00753837](https://doi.org/10.1007/BF00753837). URL: <http://link.springer.com/10.1007/BF00753837> (visited on 03/07/2025).
- [122] *Cait (Cryogenic Artificial Intelligence Tools)*. <https://cait.readthedocs.io>. URL: <https://github.com/fewagner/cait>.

- [123] R. Strauss et al. “Beta/gamma and alpha backgrounds in CRESST-II Phase 2”. In: *Journal of Cosmology and Astroparticle Physics* 2015.6 (June 16, 2015), pp. 030–030. ISSN: 1475-7516. DOI: [10.1088/1475-7516/2015/06/030](https://doi.org/10.1088/1475-7516/2015/06/030). URL: <https://iopscience.iop.org/article/10.1088/1475-7516/2015/06/030> (visited on 03/27/2025).
- [124] National Nuclear Data Center. *NuDat database*. URL: <https://www.nndc.bnl.gov/nudat/>.
- [125] C. Cozzini et al. “Detection of the Natural Alpha Decay of Tungsten”. In: *Physical Review C* 70.6 (Dec. 13, 2004), p. 064606. ISSN: 0556-2813, 1089-490X. DOI: [10.1103/PhysRevC.70.064606](https://doi.org/10.1103/PhysRevC.70.064606). URL: <https://link.aps.org/doi/10.1103/PhysRevC.70.064606> (visited on 03/27/2025).